DISSERTATION

INVESTIGATING MOLECULAR INTERACTIONS CONTRIBUTING TO SELF-ASSEMBLY ON ULTRAFAST TIME SCALES WITH TWO-DIMENSIONAL INFRARED SPECTROSCOPY

Submitted by

Christopher Thomas Kuhs

Department of Chemistry

In partial fulfillment of the requirements

For the Degree of Doctor of Philosophy

Colorado State University

Fort Collins, Colorado

Fall 2019

Doctoral Committee:

Advisor: Amber T. Krummel

Martin McCullagh
Justin Sambur
Kathryn Ross

ABSTRACT

INVESTIGATING MOLECULAR INTERACTIONS CONTRIBUTING TO SELF-ASSEMBLY ON ULTRAFAST TIME SCALES WITH TWO-DIMENSIONAL INFRARED SPECTROSCOPY

Many chemical systems rely on π-π interactions to drive self-assembly. These systems range from peptides and proteins to polyaromatic hydrocarbons (PAH). There are a wide variety of chemical environments where π-π interactions are critically important. In such environments, factors such as sterics or the solvent surrounding these aromatic systems will affect the final aggregate. To elucidate the chemical structures and system dynamics that exist in these π stacking molecular structures, many researchers are turning their attention to examining molecular vibrations. Chemical vibrations are affected by molecular coupling, solvent environments, and aggregated state. By using infrared spectroscopy to monitor these vibrations, we can develop a molecular picture of these aggregated systems. Two-dimensional infrared (2D IR) spectroscopy provides additional information on the structure and dynamics of aggregated systems that cannot be gained from traditional linear infrared techniques. This thesis focuses on using 2D IR to study two aggregate systems. First, this thesis focuses on the self-assembly of phenylalanine based dipeptides. One of the primary goals of this work was to understand how the solvent interacts with the dipeptides, a factor critical for self-assembly. Using 2D IR and molecular dynamics simulations this work investigated how the primary structure of an aromatic dipeptide system, Val-Phe versus Phe-Val, affects the solvation dynamics around the dipeptide. It also explores the primary sequence influences hydrogen-bond dynamics. The second part of this work examines how the polarity of a solvent influences π-π stacking of PAH. Using 2D IR it was found that these solvent dependent structures have different degrees of vibrational energy delocalization. This suggests that the choice in solvent will influence the flow of energy though aggregated systems.

ACKNOWLEDGEMENTS

In many regards, completing my Ph.D. is not only a personal accomplishment but also the accomplishment of my friends, mentors, colleagues, and loved ones. Through this process I have depended on these people for advice, guidance, and support. I truly believe that without them none of this would be possible.

First, I would like to thank my amazing PhD advisor Professor Amber Krummel. She has had faith in me through this process even when I didn't have faith in myself. Dr. Krummel is always wanting to help and will go the extra mile for her students to make sure they have what they need for successes. Furthermore, I need to thank Dr. Brad Luther. Dr. Luther had taught me so much about ultrafast laser systems. Without his guidance I would not have technique skills that I needed to complete this endeavor. Through his teaching I was able to complete this project, and will be qualified to work on a variety of ultrafast research projects.

I am also indebted to the love and support I revived from my colleagues past and present. There intellectual and moral support helped me get through many long days.

I need to thank my family for belief and support of me though these processes. My mother and father have provided unending support thought my entire academic carrier, so thank you.

Finally, I would not be here without my beautiful wife. Thank you, Erika.

TABLE OF CONTENTS

LIST OF FIGURES

Chapter 1

Introduction

The first section of this chapter focuses on the importance of understanding molecular self-assembly. It will examine some of the other techniques for understanding self-assemble processes and the benefit that 2D IR provides. It will then focus on the chemical systems that are the subject of this thesis.

The second part of this chapter is from a publication from 2018 from the journal Institute of Electrical and Electronics Engineers (IEEE) Journal of Selective Topics in Quantum Electronics. I wrote this review article as an invited paper to discuss the advancements of 2D IR spectroscopy and how the technique is applied to the study of molecular systems[1].

1.1 Introduction to Molecular Self-Assembly

Molecular self-assembly is an appealing synthetic approach for the development of novel materials due to the relative ease of synthesis and the diversity of material properties that can be achieved. As such, self-assembled materials have been utilized in applications such as tissue engineering, charge separation for photovoltaics and drug delivery vehicles. In order to make to fast strides in these disciplines, chemists would need a data bank of molecular building blocks such that they would know exactly how to create an aggregated material for any application. Because of the large variety of self-assembled compounds, currently there is no such data bank, but advancements have been made.

Synthetic chemists have been working diligently at trying combinations of environmental conditions and chemical properties to see what types of structures form. They have found that aggregate properties can be changed by solvent, or through functionalizing a particular base building block with chemical functional groups to drive aggregation towards a final assembled structure. For example, using

atomic force microscopy, it has been found the dipeptide diphenylalanine will form different structured nanotubes in ethanol verses toluene[2]. There are many parameters that can be used to tune to a particular self-assembled structure. As such the "phase" space to explore for self-assembly is vast and it is not feasible to do it for the endless possibilities of combinations. Therefor it is necessary to develop design principles based on physico-chemical properties that link monomeric structures, solvation dynamics, and final self-assembled structures of aggregates.

The synthetic approach discussed above considers looking at self-assembly through an iterative technique to determine the best combination of molecular composition and solvent conditions to generate a desired aggregate. Alternatively, if the scientific community had a better understanding of the fundamental physical properties that drive aggregation then researchers would be able to form more informed decisions in their synthetic endeavors. Broadly speaking there are two approaches at getting at these physical properties, computational methodology and experiments. Computational techniques such quantum mechanical calculations and molecular dynamics simulations provide valuable information on aggregation events. For instance, molecular dynamics will inform how the environmental conditions surrounding solute molecules will force them together and predict how the solvent will drive dimer configurations. Computational techniques have been applied to many scientific problems which has resulted in useful information. However, one of the greatest achievements in physical chemistry is when these computational results can be correlated with experimental observables.

The modern experimentalist has many tools at their disposal to examine molecular aggregation. For example, UV-Vis spectroscopy is a common technique used to look at polyaromatic hydrocarbons. The UV-Vis spectrum of these chemical systems will shift in intensity and position depending on the aggregate formed. Typical experiments would look at how changing the concentration changed the spectrum, and thus report on the aggregate structures. However, obtaining more specific information can be challenging. To state the exact nature of the aggregate requires assumptions that are sometimes not easy to substantiate. Therefore, these experiments can be coupled with other techniques such as linear infrared spectroscopy. Infrared spectroscopy reports on molecular vibrations of a system. Therefore, if changes in the aggregate

occurs, it will manifest itself in changes in the vibrations modes that are probed with linear IR spectroscopy. Problems occur when the system becomes incredibly complex; for example, in polyaromatic hydrocarbons, the vibrational modes intrinsic to the PAH can be used to report on structure, but are likely to be spectrally overlapped. Thus, spectral information can be convoluted on top of each other, resulting in spectra that are difficult to interpret. It would therefore be advantageous to use a technique that provided additional information on the structural motif of these systems.

Two-dimensional NMR has become a workhorse technique producing high resolution structural information of many compounds[3,4]. However, NMR experiments require high concentration samples and several milliliter volumes. Furthermore, NMR does not have particularly high time resolution[5]. For example, dynamics associated with hydrogen bond making and breaking cannot be accessed by NMR, because these events are too fast[4,5]. It is possible that initial steps in self-assembly are driven by events that occur on sub-nanosecond time scales. Elucidating dynamic behaviors on ultrafast time scales may give scientists an additional parameter to consider when comparing molecular building blocks involved in self-assembly. 2D NMR falls short in this front as well, only providing information on the microsecond time scale.

Two-dimensional infrared (2D IR) spectroscopy has proven to be a powerful technique to investigate solvent dynamics[8], structural dynamics in biological systems[9,10], and energy transport in materials[11,12]. The power of 2D IR is due to the structural resolution gained from observing molecular vibrations and the time resolution inherent to 2D IR due the ultrafast pulses used to perform the experiments. 2D IR spectroscopy is an ultrafast optical technique that utilizes three ultrafast pulses to interact with the sample. The resulting spectrum contains two frequency axes, referred to as the pump axis and the probe axis. In the simplest case of a single vibrational oscillator, the resulting spectrum is a peak pair, equal in amplitude and with opposite sign of intensity. This peak pair is the result of optically pumping the chemical system into the first and second vibrational levels[13].

When molecular systems become more complex, like in a self-assembled chemical system, the molecular vibrations of a molecule will influence one another[14]. Because 2D IR has two frequency axis, the plethora of information is spread out, making data interpretation easier than its linear counterpart[15]. Depending on the aggregate and the local solvent environment around it a 2D IR spectrum will show changes in cross peaks[16] and peak shapes[17]. Furthermore, because 2D IR uses femtosecond pulses to interrogate the chemical system, femtosecond chemical dynamic information can be obtained[18,19].

The aim of the work presented in this thesis was to design 2D IR experiments to probe two systems: 1. The dipeptide building blocks valine-phenylalanine/phenylalanine-valine (VF/FV) and 2. Aggregate structures formed by violanthrone-79. These two sets of experiments are used to explore two different extremes with regards to self-assembly. The work with VF/FV is focused on understanding how slight changes in the monomer structure influenced how the solvent behaved and interacted with the molecular building blocks. This was accomplished by examining the isomers of valine bonded with phenylalanine. These experiments revealed drastic changes in the solvent interaction surrounding the dipeptide building blocks. In future work, it will be important to determine if the solvation surrounding the dipeptides plays a role in restricting the possible conformations that can be accessed by the dipeptides as they assemble into different structures. At the opposite end of the self-assembly spectrum, aggregates of violanthrone-79 are investigated. More specifically, this work considered how solvent influences the overall aggregate structure and how the vibrational energy distribution changed depending on the resulting aggregate structure. In both cases, the experimental results were married with computational efforts to generate a more complete view of these two extremes in self-assembly.

1.2 Introduction for Institute of Electrical and Electronics Engineers Review Article

The advent of ultrafast laser sources allowed spectroscopists to bring nonlinear optical spectroscopy techniques with high time resolution and sensitivity to molecular structure to fruition.

Many years prior to the first transient absorption and pump-probe experiments, theorists revealed to the community the wealth of information to be gleaned from coherent multidimensional spectroscopy experiments[20,21]. In the decades since, coherent multidimensional spectroscopy techniques including 2D Electronic Spectroscopy (2D ES)[22], 2D Infrared (2D IR)[23] spectroscopy, and more recently mixed frequency 2D spectroscopy techniques including 2D Vibrational Electronic (2D VE)[24], 2D Electronic Vibrational (2D EV)[25], and 2D Sum Frequency Generation (2D SFG)[26,27] spectroscopy have been developed. Each of these spectroscopic techniques have proven to be powerful experimental tools to study aggregate structure[14], exciton dynamics, chemical dynamics[28], and ultrafast chemical reactions[29] across broad fields of science. These range from biology[30] to materials engineering to geochemistry [31] to catalysis[32]. The expanse of these investigations has been possible due to the techno-logical breakthroughs made in ultrafast science along the way. This brief review will focus on 2D IR spectroscopy, the basic principles that govern 2D IR, recent technological advances expected to impact 2D IR experiments, and new 2D vibrational spectroscopy tools. In each section concrete examples of 2D IR experiments performed will be used to illustrate the points. However, this review will not be able to cover all of the important results that have come out of 2D IR spectroscopy experiments to date. It is also important to note that the field of multidimensional spectroscopy in general has greatly benefited from crucial advances made in theoretical frameworks with which these spectroscopy experiments are interpreted. However, the brevity of this review will not allow these advanced to be discussed.

1.3 Basic Principles of 2D IR Spectroscopy

This section provides a backdrop to discuss the principles of vibrational modes, macroscopic polarizability, excitation path-ways, observables in 2D IR spectroscopy, and approaches to extract the information available from 2D IR experiments.

1.3.1 Vibrational Modes

Molecular vibrations are powerful reporters of chemical structure and dynamics. Vibrational modes localized to a specific bond can be used to determine molecular structure with angstrom level resolution[33,34]. 2D IR spectroscopy can be used to directly measure the curvature of the vibrational potential energy surface and as such can directly report vibrational coupling constants required to make structural determinations of molecular systems ranging from small molecules to macromolecular systems. These have included the study of hydrogen bond making and breaking[18], contact ion pairs[35], and the vibrational characteristics of different isomers[15]. In addition, 2D IR spectroscopy has been used to determine the structure of amyloid fibrils[36,37], the pH dependence on Influenza A's proton channels[38], and the structure of potassium ion channels[30].

Vibrational modes are also sensitive to the local environment in which they reside. Interactions of solvent molecules with a vibrational mode can alter the force constant, reduced mass, or anharmonicity of the vibrational mode. Thus, molecular vibrations are sensitive to fluctuations in the local environment sur-rounding the mode. In linear IR spectroscopy this information is embedded in the line shape of the observed IR spectrum[39]. However, quantitative information regarding chemical dynamics that is available from the linear IR spectrum is limited. 2DIR provides access to investigating vibrational dynamics quantitatively and across timescales ranging from femtoseconds[6,40] to picoseconds[15,41] and even into longer nanosecond time scales[42]. The femtosecond time resolution is achieved using ultrashort mid-infrared pulses and access to vibrational dynamics on the nanosecond timescale depends on the vibrational lifetime of the oscillator. In addition, 2D IR experiment scan be set up to discern the homogeneous contributions from the inhomogeneous contributions to the observed linewidths in the spectra. Taken together the vibrational dynamics probed during a 2D IR spectroscopy experiment will provide quantitative

details of chemical dynamics in condensed phase systems. For example, advances have been made in understanding the role of hydrogen bonding in proton transfer events[43], the dynamics involved with crossing over from liquid to glassy regimes in molecular glasses[42], or the role of multipole interactions in ionic liquids, to name a few[44]. The ability to better understand the dynamics of chemical systems is a key strength of 2D IR spectroscopy.

1.3.2 Pathways

Spectral congestion is a difficult challenge to overcome in linear IR spectroscopy. Observed peaks in linear IR spectra carry information related to chemical structure and dynamics. Thus, the linear response observed in linear IR spectra is a convolution over the contributions from chemical structures and chemical dynamics. Investigators can use a variety of tools to deconvolute the structural responses from the dynamical responses observed in linear IR spectroscopy, but this often relies on using external vibrational labels or isotope labeling of a particular vibrational mode. 2D IR spectroscopy techniques offer the ability to spread information across two dimensions and probe the structural response independently from the dynamical responses. However, to accomplish this task, one must consider the energetic pathways available in 2D IR spectroscopy and consider how pathways can be isolated from one another. Here, we briefly develop the concept of pathways available via light-matter interactions, relate the pathways to the macroscopic polarization of a sample, and then describe experimental approaches to isolate the pathways of interest. For a more detailed description, the readers are referred to references 34 and 35. 2D IR spectroscopy requires three light-matter interactions. In practice there are a few ways of producing these light-matter interactions, a topic that is discussed in the optical geometry section, however the underlying principles are the same no matter which optical geometry is used. When a sample

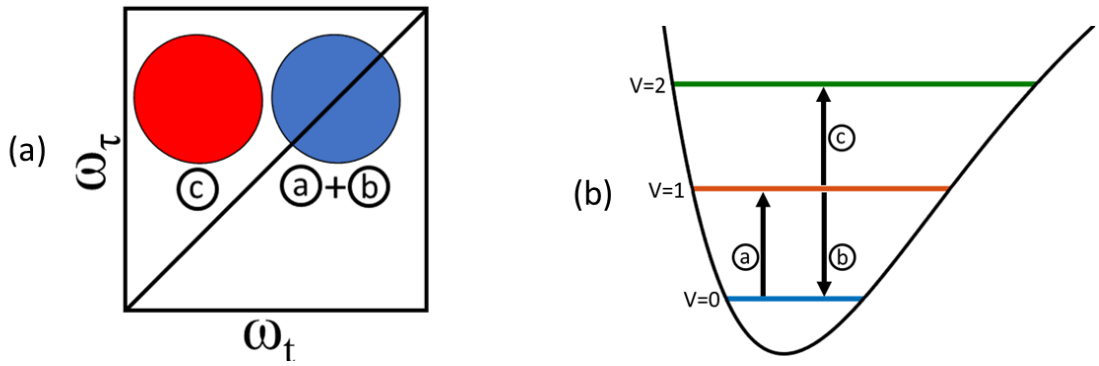

Figure 1.1 Cartoon representations of a 2D IR spectrum, and (b) the corresponding energy level diagram, (b). The blue peak in (a) is the addition of the bleach and excited state emission. These are labeled as transitions (A) and (B)in the Fig. 1b, respectively. The red peak in (a) corresponds the excited state absorption, the transition represented by (C) in Fig. 1.1.b.

under goes excitation from multiple light-matter interactions, the system goes through different Liouville pathways, a concept covered in greater depth in reference[46]. Here we will take a more general view of the processes necessary to generate a 2D IR signal. To illustrate what is happening, a simple two-level vibrational system can be used. The molecules start out in the ground vibrational state. The first pulse will excite the sample and will generate a coherence between the ground state and first excited state. The second pulse will excite the sample and can create populations in the first excited state or drive the system back down to the ground state. In addition, it is possible to create another coherence between the first and second vibrational excited states. The third pulse excites the sample forming coherences between either the ground and the first excited state or between the first excited state and the second excited state. After the three pulses interact with the sample, a signal field is emitted from the sample and is encoded with the molecular response of the system. The responses can be observed as peak pairs in the 2D IR spectrum, where one is positive going and the other is negative going. Each peak represents different processes or pathways the vibrational system can undergo in a given excitation and detection scheme. A diagram showing the energy levels of these processes and a diagram of the corresponding 2D

spectrum can be seen in Fig. 1. Multiple path-ways can contribute to particular sets of peaks. For example, the negative going peak contains the bleach and the stimulated emission, labeled A and B in in Fig. 1 respectively. The positive going peak contains the excited state absorption labeled as transition C. The above example is for a single vibrational mode and the simplest of experimental geometries. However, if multiple vibrational modes lie within the bandwidth of the excitation pulses, then two or more diagonal features appear in the spectrum. When multiple excitations exist in the bandwidth of the pulse then cross peaks can also be observed. Showing up in the upper left hand and lower right hand corners of the spectrum, cross peaks are the result of vibrational coupling[13,14] chemical exchange[28], population transfer or coherence transfer[47]. A more detailed look at coupling is discussed below.

1.3.3 Macroscopic Polarizability

Nonlinear spectroscopy relies on a chemical system emitting a macroscopic polarization in response to an external electric field. 2D IR is a third order spectroscopic technique and as such, the macroscopic response is the function of three input pulses. In a 2D IR pulse sequence each pulse interacts with the sample at time intervals t1, t2, and t3. Therefore, an expression for the macroscopic polarizability can be written as

$$P^{(3)} \propto \int_0^\infty dt_3 \int_0^\infty dt_2 \int_0^\infty dt_1 \, E_3(t-t_3)E_2(t-t_3-t_2)\cdot E_1(t-t_3-t_2-t_1)\cdot R^{(3)}(t_3,t_2,) \; (1.1)$$

where En are the three different electric fields and $R^{(3)}$is the third order response function of the chemical system. The R(3)contains all of the possible excitation pathways that can occur. After applying the second-order cumulant expansion approximation, the Condon approximation, the short time approximation, and assuming that only beams satisfying the phase matching conditions

of the experiment contribute to the signal field, there are 8 response functions for a single vibrational mode in a chemical system four rephasing and four nonrephasing responses[13]. However, if there are multiple vibrational modes within the bandwidth of the excitation pulses, then each one will have their own eight responses.

1.3.4 Dynamics

The absorption peaks in linear IR spectroscopy experience two sources of peak broadening, homogeneous and inhomogeneous broadening. Homogenous broadening comes from very fast fluctuations between the molecule and the bath modes of the solvent. Inhomogeneous broadening instead comes from the same molecules being in different local environments, and therefore having a distribution of different frequencies[48,49]. A depiction of this can be seen at the top of Fig. 2(a). where underneath the broad gaussian line shape there are several narrower gaussian line shapes representing multiple vibrational modes making up the total shape of the absorption feature. These different broadening processes also manifest themselves in 2DIR spectra. If a chemical system experiences inhomogeneous broadening, the peak in the 2D IR spectrum will be elongated along the diagonal of the spectrum[13], as seen in the cartoon2D IR spectrum in Fig. 2(a). The fast and slow chemical dynamics in a system can be measured in 2D IR experiments, because of the femtosecond time resolution inherent to 2D IR experiments that utilize femtosecond light sources. Characterizing the inhomogeneity of a chemical system is achieved by monitoring the shape of peaks in 2D IR spectra collected as a function of delay time between the second and third pulses, denoted Tw. As Tw becomes larger, the molecules in the sample have more time to

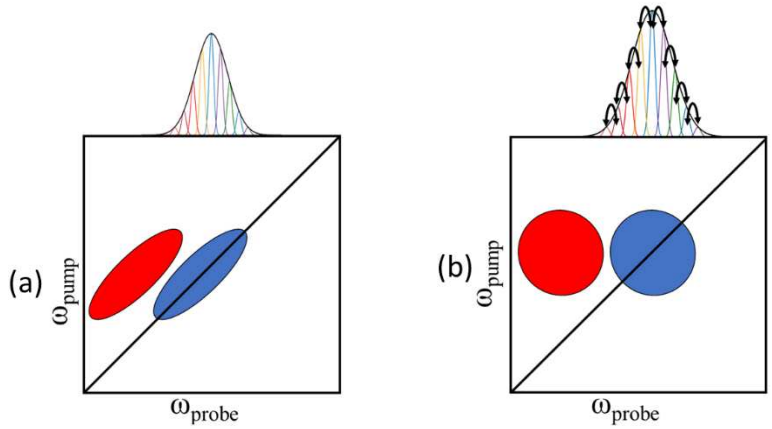

Figure 1.2 Depiction of an in homogeneously broadened spectral feature. (a) Linear IR and 2D IR spectrum at early times. The vibrational mode exists in many solvation environments resulting in many different vibrational frequencies under the peak in the linear IR spectrum and resulting in an elliptical feature in the2D IR spectrum. (b) After a delay T_w a vibrational mode has time to sample all of the solvent environments, shown by the black arrows, and resulting in round shape of the peak pair in the 2D spectrum.

experience the different solvation environments. This is denoted in Fig. 2(b) by the arrows showing that the different vibrational modes that make up the broad peak sample all the different solvent environments. The peaks in the resulting2D IR spectra progress from being elongated to being round as shown in Fig. 2(b). The evolution of the spectra is referred to as spectral diffusion. Spectral diffusion is manifest from a variety of dynamic properties of the molecule[50,51]. Changes in line shape can be related to important physical properties, including the nature of the solvent-solute interactions in a system. Several techniques have been developed to quantify2D IR peak shapes, including monitoring the ellipticity of peak shapes, nodal line slopes (NLS) between the peak pairs, and monitoring the center line slope (CLS) of a particular peak in a2D IR spectrum[52]. The readers are referred to references 39 and 40 for a comprehensive discussion of these techniques[17,53]. Regardless of the method used to quantify the change in peak shape, the underlying goal is to experimentally determine the frequency frequency correlation function (FFCF)[54].The FFCF is an expression that describes the fluctuations of the frequencies of a molecule, which are directly related to the fluctuations of the local environment around the oscillator .Experimentally

this oscillator can either be the solvent system, the solute itself, or a probe molecule containing a isolated vibrational mode that is added for reporting on the dynamics of interest[55–57]. The FFCF can be expressed as C(t) as seen in (1.2). Where δω(t) is the difference between the measured frequency at time t and the average frequency over the course of the experiment, $\delta\omega(t)=\omega(t)-\langle\omega\rangle$

$$C(t) = \langle \delta\omega(t)\delta\omega(0)\rangle \qquad (1.2)$$

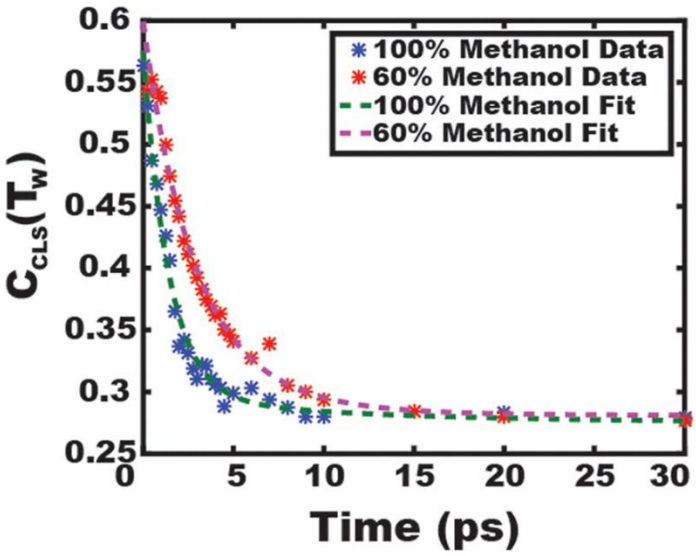

Figure 1.3 LS fits for KOCN in a methanol solution and a mixed methanol-DMF solvent environment. These results show there are differences in the spectral diffusion times for these two solvent environments[58]. Figure reproduced from Ref. 46.

Experimentally, 2D IR spectra are collected at a series of waiting times, T_W. Then peak shape is quantified for each spectrum using one of the methods mentioned above. An example of this can be seen in Fig. 3 where CLS of each spectrum in a T-waiting experiment is plotted as a function of time. In this example 2D IR spectra were collected within a microfluidic device to demonstrate how binary solvent mixtures have unique solvation environments. In this case, as it is with most FFCF analyses, the data is fit to a biexponential, like the one shown in (3). In (3) there are the time constants, τ_1 and τ_2, which are the fast and slow time components to the dynamics, respectively.

$$C(t) = Ae^{\frac{-\tau}{T_1}} + Be^{\frac{-\tau}{T_2}} \quad (1.3)$$

assuming Bloch dynamics in which there are two different, separable time scales for solvent rearrangement. The Bloch dynamics picture holds for many types of condensed phase systems. An important question is where do dynamics experiments to generate FFCFs find their utility? Researchers have had a growing interest in ionic liquids. Current synthetic chemical processes primarily use volatile organic compounds, VOCs, as their primary solvent. Unfortunately, VOCs are a major source of pollution, and as a result there has been a push for greener solvents[59]. One such solvent system are room temperature ionic liquids or RTILs. RTILs are organic salts that are liquid below 100°C. Their low melting point comes from RTILs having very low vapor pressures. The low vapor pressure is also one of the properties that lessens them as a pollutant, allows for ease of recycling, and purification[60]. Another compelling reason to use RTILs is the ability to tailor them to a particular need. Changing properties such as the different ion pairs or carbon chain lengths on the ions can alter the properties of the solvent[61] . Some consider RTILs as the next big advancement in synthetic chemistry, but many of its solvent properties are not well understood. 2D IR has become an emerging tool to study the chemical dynamics of this important chemical system. Examples of the utility of 2D IR for investigating the dynamic properties of ionic liquids is currently being investigated by several groups around the world[32,58,61]. For example, Garret-Roe investigated azides interacting with different ionic liquid solvent environments[44]. Azides are important in SN2 reactions in biochemistry. Moreover, the polarity of the solvent can drastically affect the rates of these reactions[62]. However, it was unclear how a solvent like an ionic liquid would affect the solvation and subsequently the reactions. In addition, questions regarding how different azide species behave in ionic liquids were largely unexplored. Dutta et. al. examined dynamical parameters of azides in solvents, including heavy water(D2O), tetrahydrofuran (THF),

and the ionic liquid 1-butyl-3-methylimidazolium tetrafluoroborate ([BMIM][BF4]) with both organic and inorganic azides[44]. The CLS analysis of the 2D IR spectra yielded information regarding the solvation of organic and inorganic azide compounds in the solvents noted above, asshowninFig.4. In D_2O all the azides studied experienced spectral diffusion within ~2 ps, as seen in Fig. 4(a). In THF they found the spectral diffusion of the inorganic azide to be 9.2 ps, roughly 2 times slower the its organic counterpart 4.8 ps, shown in Fig. 4(b). The authors attribute this difference to the first solvation shell each solvent formed around the azide. In ionic liquids the spectral diffusion exhibited by organic and inorganic azides have dramatically different time scales. Dutta et. al. show that organic azides experience spectral diffusion within sub 5 ps, but the inorganic azides with diffusion times greater than 20 ps, presented in Fig. 4(c). The authors relate these results to the viscosity of the solvent system. More generally, this work also demonstrates the sensitivity of azides as vibrational probes of local molecular environment.

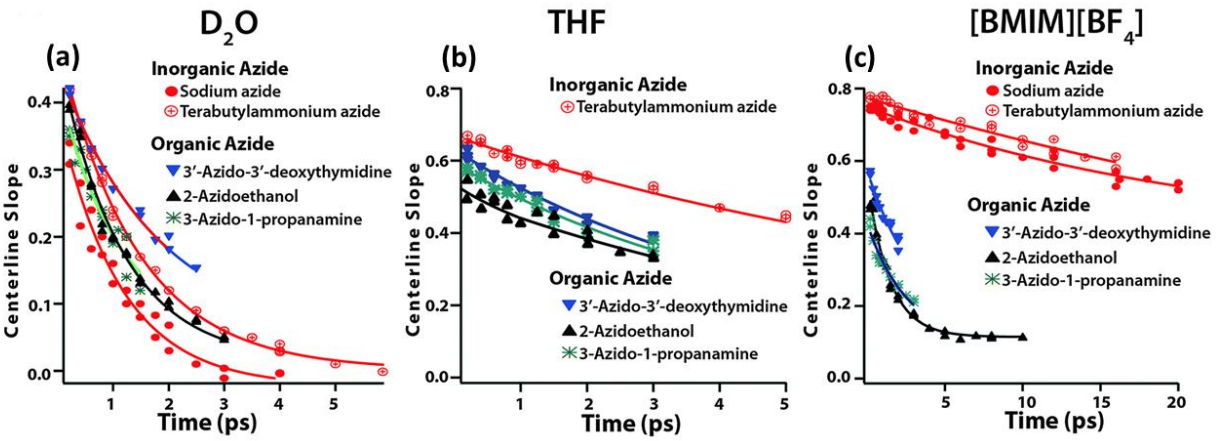

Figure 1.4 CLS data for organic and inorganic azide compounds in different solvents. (a) In THF both species of azides have similar solvent interactions.(b) The CLS decays are similar for the azides in heavy water. (c) CLS data for the azides in ionic liquid[BMIM][BF4]. From the data presented in (c) a clear difference in the solvent-solute interaction can be seen[44]. Reproduced from Ref. 33.

1.3.5 Structure

Molecular structure can be determined so long as the curvature of the potential energy surface can be probed. This curvature can be measured using 2D IR spectroscopy by monitoring the off-diagonal anharmonicity of vibrational modes[23]. If a vibrational mode is localized to a chemical bond, it is possible to build a local mode picture of the vibrations and the coupling between the localized vibrational modes. The framework of coupled, localized vibrational modes have afforded the impact of 2D IR spectroscopy for structure determination to be broad. Vibrational coupling models have been built to describe peptides[63], proteins[64], nucleic acids[10], and aggregates of organic dyes[14] to name a few. The structures of these systems were related to the linear IR and 2D IR spectra by determining the nature of the vibrational coupling between localized vibrational modes in the molecules. Cross peaks that exist at Tw=0 in a 2D IR spectrum provide a window into understanding the nature of the vibrational coupling between vibrational modes. To understand the appearance of cross peaks, consider two vibrational modes A and B with frequencies ω_1 and ω_2 where $\omega_2>\omega_1$ and the two modes are coupled. An energy level diagram and example spectrum can be seen in Fig. 5. The energy level diagram in Fig. 5 depicts the different vibrational excitations that can occur within a 2D IR experiment of coupled vibrational modes. The red arrows denote the pump pulses establishing populations in ω_1 and ω_2, and the blue arrows denote the coherences that occur with probe pulse. As discussed above, the peaks that lie on the diagonal comes from the bleach and stimulated emission, blue peak, and the excited state absorption, red peak.

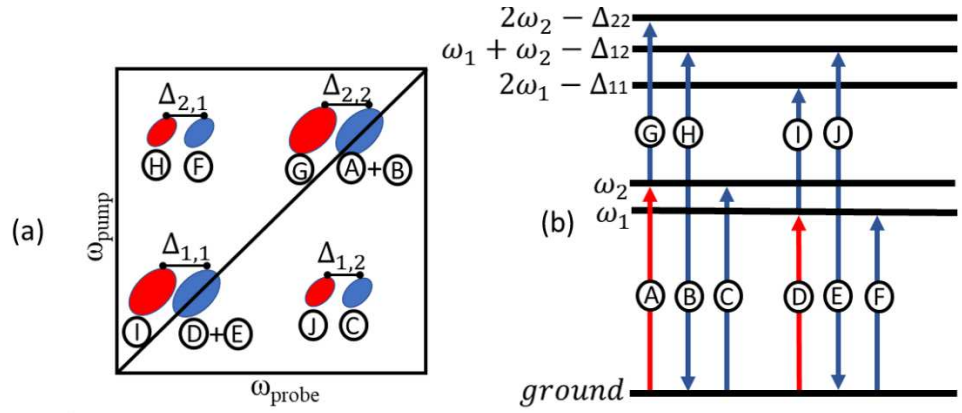

Figure 1.5 Energy level 2D IR for a system with coupled oscillators, and(b) the corresponding energy level diagram, where the oscillators I and j are equal to 1 and 2, respectively.

Here, there are two sets of peak pairs on the diagonal, one for each vibrational mode. Because vibrational modes A and B are coupled the spectrum also contains pairs of cross peaks. Like the diagonal peaks, the cross peaks show upas a peak pair, one negative going and the other positive. The off-diagonal anharmonicity, Δij, can be used to determine the vibrational coupling constant [30]. Perturbation theory provides an analytic solution to relate the off-diagonal anharmonicity to the vibrational coupling constant, βij. The last term in the Taylor series expansion of potential energy with respect to vibrational modes, Q, as seen in (4), is the bilinear vibrational coupling term. This term is set equal to the bilinear vibrational coupling constant, βij, seen in (5). Therefore, vibrational coupling is directly related to the curvature of the potential energy surface. Using (6),βij

$$V(Q_i, Q_j) = \frac{1}{2}\left(\frac{\delta^2 V}{\delta Q_i^2}\right) Q_i^2 + \frac{1}{2}\left(\frac{\delta^2 V}{\delta Q_j^2}\right) Q_j^2 + \frac{1}{2}\left(\frac{\delta^2 V}{\delta Q_i \delta Q_j}\right) Q_i Q_j \qquad (1.4)$$

$$\beta_{i,j} \propto \left(\frac{\delta^2 V}{\delta Q_i \delta Q_j}\right) Q_i Q_j \qquad (1.5)$$

$$\Delta_{i,j} = -4\Delta \frac{\beta_{i,j}}{\left(h\omega_j - h\omega_i\right)^2} \qquad (1.6)$$

can be determined based on the off-diagonal anharmonicity Δ_{ij}, the diagonal anharmonicity Δ, and the frequency of the transitions, ω_i and ω_j; it is assumed that Δ_{ii} and Δ_{ij} are approximately the same. However, in order to relate the linear IR spectrum or the 2D IR spectrum to molecular structure, the nature of the coupling between the vibrational modes must be determined. In general, vibrational coupling can be classified as mechanical coupling, electrostatic coupling, or a mixture of these two extremes. Interactions between vibrational modes in a molecule can be mechanical in nature, electrostatic in nature, and sometimes a combination of mechanical and electrostatic interactions. The community has utilized quantum electronic structure and frequency calculations to estimate the extent to which the vibrational coupling within a molecule is dominated by mechanical coupling or electrostatic coupling. For example, finite difference methods (FDM) have been used to calculate the bilinear vibrational coupling constant directly as the curvature of the potential produced from electronic structure and frequency calculations[10,65,66]. If the vibrational coupling is dominated by mechanical interactions, then the system needs to be investigated in a time-dependent manner and is very useful to determine vibrational energy flow pathways through a molecular system. Work exemplary of this scenario is recent work by Rubstov and co-workers[67], as well as Bredenbeck and co-workers[68]. Two-color 2D IR spectroscopy experiments or ultrabroad-band 2D IR spectroscopy experiments can be used to monitor oscillators with large differences in energy can be performed as a function of time in order to monitor vibrational energy flow directly. In contrast to mechanical coupling of vibrational modes, electrostatically coupled oscillators affords the utility of modelling to relate the magnitudes and sign of the vibrational coupling constants to molecular structure. The existing models used to describe vibrational coupling in an electrostatic picture range from a simple transition dipole coupling model to more sophisticated models that take into account electrostatic interactions within the transition dipole

volume, for example the Transition Dipole Density Distribution model, or higher order multipole interactions. The simplest model is the Transition Dipole Coupling (TDC) model, pioneered by Krimm et al. to examine secondary structure in proteins[69].

TDC has been parametrized for many other types of molecules including nucleic acids, as well as molecular aggregates of organic dye molecules like violanthrone-79. The vibrational coupling constant, βij, depends on the strength of the coupled oscillators, the position of the dipoles relative to each other, and the relative angles between them, in accord with (7). TDC is a powerful model although it does have its limitations. For example, when two oscillators are too close to each

$$\beta_{ij} = \frac{1}{4\pi\epsilon_0}\left[\frac{\vec{\mu}_i \cdot \vec{\mu}_j}{r_{ij}^3} - 3\frac{(\vec{r}_{ij} \cdot \vec{\mu}_i)(\vec{r}_{ij} \cdot \vec{\mu}_j)}{r_{ij}^5}\right] \quad (1.7)$$

other, TDC overestimates the magnitude of the vibrational coupling[70]. However, the TDC is useful for considering one of several reasons why polarization dependent 2D IR spectroscopy measurements are useful. Experiments have been developed to exploit cross peaks to determine the relative angle between two vibrational modes in a molecule[71]. These experiments require

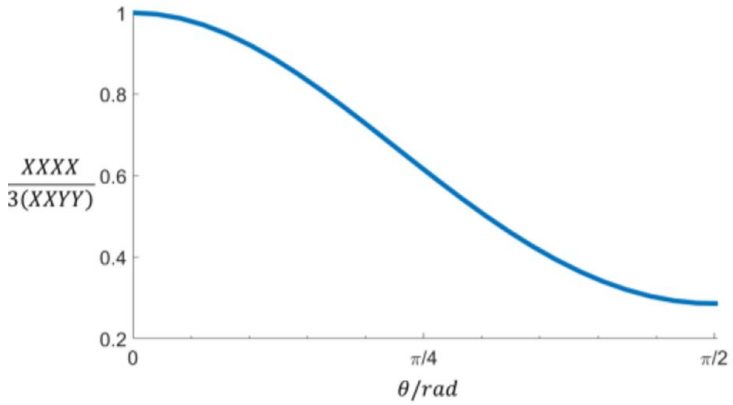

Figure 1.6 lot of (8) that related the intensity ratio of cross peaks taken a two different polarization conditions and the relative angle between the transition diploe moments.

collecting data under different polarization conditions and taking the ratio of intensities of the cross peaks. The intensity ratios are then compared to the plot shown in Fig. 6 to determine the relative angle between the two transition dipole moments. Fig. 6 is a plot of (1.8), where P2 is

$$\frac{XXXX}{3(XXYY)} = \frac{4P_2 + 5}{10 - P_2} \tag{1.8}$$

$$P_2 = \frac{1}{2}(3\,cos^2\,\theta - 1) \tag{1.9}$$

equal to (1.9). The formalism noted above is appropriate for purely absorptive spectra collected in a pump probe geometry. If a BOX-CAR beam geometry is used in which the wave vector direction and polarization of each pulse is manipulated independently, then the ratio between cross peaks in the XXXX and XYYX polarization conditions should equate to (1.10).

$$\frac{XXXX}{3(XYYX)} = \frac{4P_2 + 5}{9P_2} \tag{1.10}$$

The angles between the vibrational transition dipoles measured under the conditions noted above can be directly input into the electrostatic coupling models, like TDC, in order to connect the measured 2D IR spectrum to molecular structure. However, polarization control can also be used to remove diagonal peaks while retaining the cross peaks[72]. One such example can be found in work by Krummel and Zanni in which model DNA oligomers of guanine and cytosine base pairs were studied to get a better understanding of vibrational coupling in DNA[10]. Their results, shown in Fig. 7, were produced with polarization-dependent 2D IR measurements to reveal both

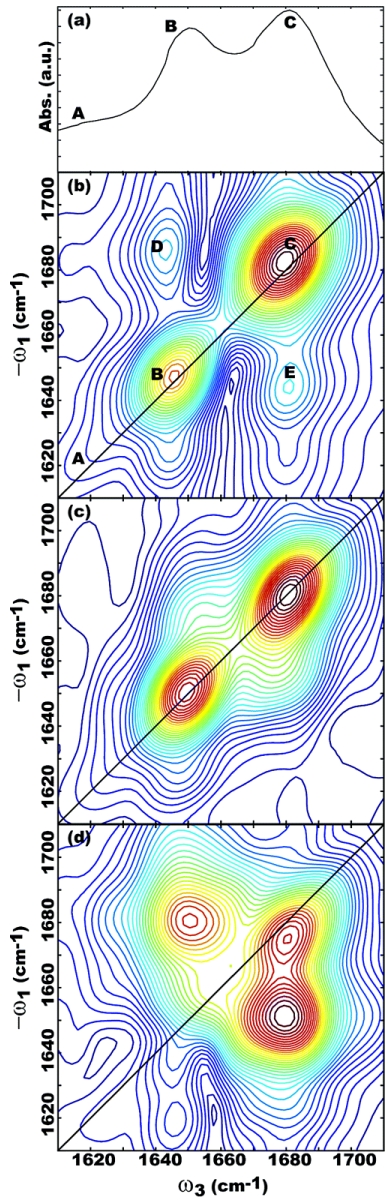

Figure 1.7 linear and 2D IR spectra of poly(dG)∗poly(dC) oligomers. (a) The linear IR spectrum of the sample with the peaks of interest labeled A though D.(b) A 2D IR spectrum collected with XXXX polarization. (c) 2D IR collected with XYYX polarization. (d) 2D IR spectrum collected with (X+Y), (X-Y), Y,X[10]. Figure reproduced from reference 53.

the relative angles between the vibrational modes in the molecule and to remove diagonal peaks to better observe cross peaks. Fig. 1.7(a) is the linear IR spectrum of the poly(dG)∗poly(dC) oligomers with the peaks of interest labeled A though D. The corresponding absolute value 2D IR spectrum in Fig. 1.7(b) shows all four features having diagonal features as well as cross peaks;

cross peaks F and G arise from vibrational coupling between modes D and C, while cross peaks E and H arise from vibrational coupling between peaks D and B. Fig. 1.7(c) is of the same chemical system but with XYYX polarization. Under this polarization condition the cross peaks gain intensity suggesting the coupled vibrational modes are nearly 90°from one another. Fig. 1.7(d) utilizes a fully orthogonal polarization condition (X+Y), (X−Y), Y, X. These spectra were collected in a BOXCAR beam geometry hence the ability to control the polarization of each electric field in the experiment. Under these conditions the diagonal features are removed from the spectra and only the cross peaks remain. The authors suggest that strong feature located close to the diagonal peak D comes from a cross peak between two modes hidden under peak D, an observable that would be unavailable without polarization control.

1.4 Experimental Systems

In Section II above, the basic principles of 2D IR were discussed in the context of experimental observables. In this section, we focus on new developments in light sources and experimental systems that have taken place in the last decade. These technological developments are enabling 2D IR spectroscopy experiments to be more broadly applied to heterogeneous chemical systems and open the doors to new measurements.

1.4.1 Source and Repetition Rate

Ti:Sapphire lasers have become a ubiquitous table top source for 2D IR spectroscopy measurements. In the 1990's, it was first demonstrated that Ti:Sapphire lasers could be used to pump an optical parametric amplifier (OPA)—a key breakthrough for IR light generation. Today, OPAs have become more compact, produce pulses higher in energy, and are more stable.

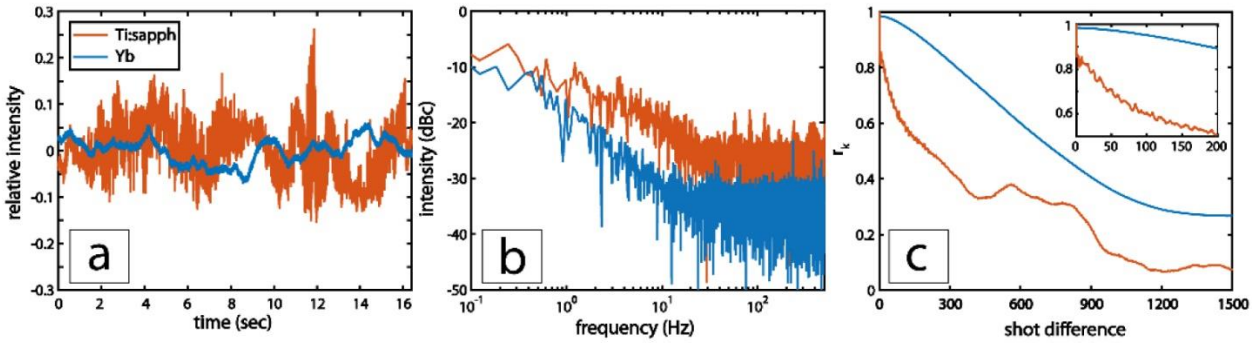

Figure 1.8 comparison of a 1 kHz Ti:Sapphire and a 100 kHz ytterbium source. (a) Relative intensity for 2^{14}pulses. (b) Fourier transform of 16,384 pulses plotted on a log scale. (c) Autocorrelations for 2^{14}pulses[73]. Reproduced form Ref. 62.

Recently efforts have been made to generate pulse trains at much higher repetition rates to allow for faster acquisition times. Starting off with 100 kHz pump-probe experiments in the visible region of the light spectrum[74], high repetition rate sources found their way into nonlinear optical spectroscopy experiments. Improvements in ytterbium-based oscillators along with advancements in nonlinear crystals have allowed for mid-IR light generation at 100 kHz. The ability for mid-IR light generation soon led to 2D IR at 100 kHz[75,76]. Stable 100 kHzmid-IR sources paved the way to dramatically reduce the acquisition time of 2D IR spectra. This technological development is opening the possibility for more time intensive experiments such as 2D IR microscopy[77]. The experimental efforts to demonstrate the utility of high repetition rate laser sources in nonlinear optical spectroscopy revealed that data produced from ytterbium based laser systems had far better signal-to-noise ratios than the signal-to-noise ratios achieved with Ti:Sapphire laser sources. Work by Zanni and co-workers has shown that ytterbium-based systems have a greater shot-to-shot stability than Ti:Sapphire systems[73]. The plots in Fig. 8 of the two laser sources as a function of time with data from a 1 kHz Ti:Sapphire lasers system shown in red and data from a 100 kHz ytterbium-based laser system in blue. Fig. 8(a) shows the relative intensity of each laser pulse for 214 pulses. Fig. 8(b), the Fourier transform of 16,384 pulses and the amplitude of the frequency

fluctuation in those pulses plotted on a log scale. The autocorrelation of the 214 shots from each system are shown in Fig. 1.8(c). These results demonstrate the improvement in shot-to-shot stability achieved in ytterbium-based sources over the Ti:Sapphire laser sources. It has been suggested that this is due to the difference in the fluorescence lifetime between the two sources.[73] The impact of the improved acquisition time and signal-to-noise ratios gained using a ytterbium-based laser system can be demonstrated by inspecting 2D IR spectra collected under different averaging conditions. Fig. 9 presents three 2D IR spectra of potassium cyanate (KOCN) in

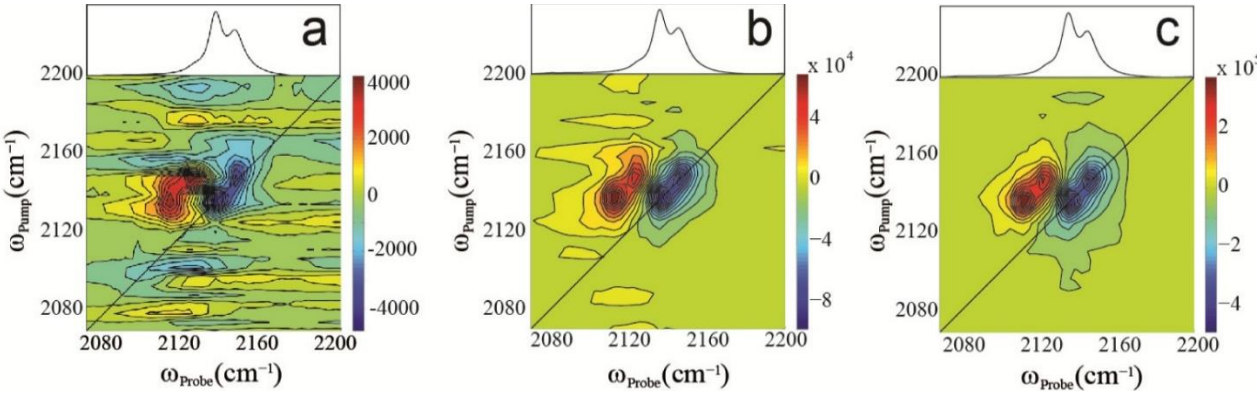

Figure 1.9 2D IR spectra of KOCN in DMF with different number of averages.(a) One spectrum, no averaging, (b) 20 spectra, (c) 100 spectra[75]. Figure reproduced from Ref. 64.

dimethylformamide (DMF) acquired with different numbers of averages. Fig. 1.9(a) is a single 2D IR spectrum with no averaging, Fig. 1.9(b) is the average of 20 spectra, and Fig. 1.9(c) is the average of 100 spectra. As Fig. 1.9 demonstrates the signal-to-noise ratio for the ytterbium system is so good that only a single spectrum is needed to resolve the spectral features.

Of course, the quality of the data is increased with averaging, but with 100 spectra averaged the peak pair is cleanly resolved. It should be noted that the spectrum in Fig. 1.9(c) only required 716 ms to acquire[75]. Donaldson and coworkers have also shown that one can take advantage of the improved sensitivity in the high-repetition rate ytterbium-based laser systems in order to investigate biomolecules at much lower concentrations, approximately 300 nM[76], much lower than

those required in previous investigations, such as 886μM[64]. There are clear advantages of moving to high repetition rate laser systems. However, in moving to high repetition rates, investigators have had to address concerns regarding the heating of molecular samples and the impact of heating on the results acquired using high repetition rate 2D IR spectrometers.

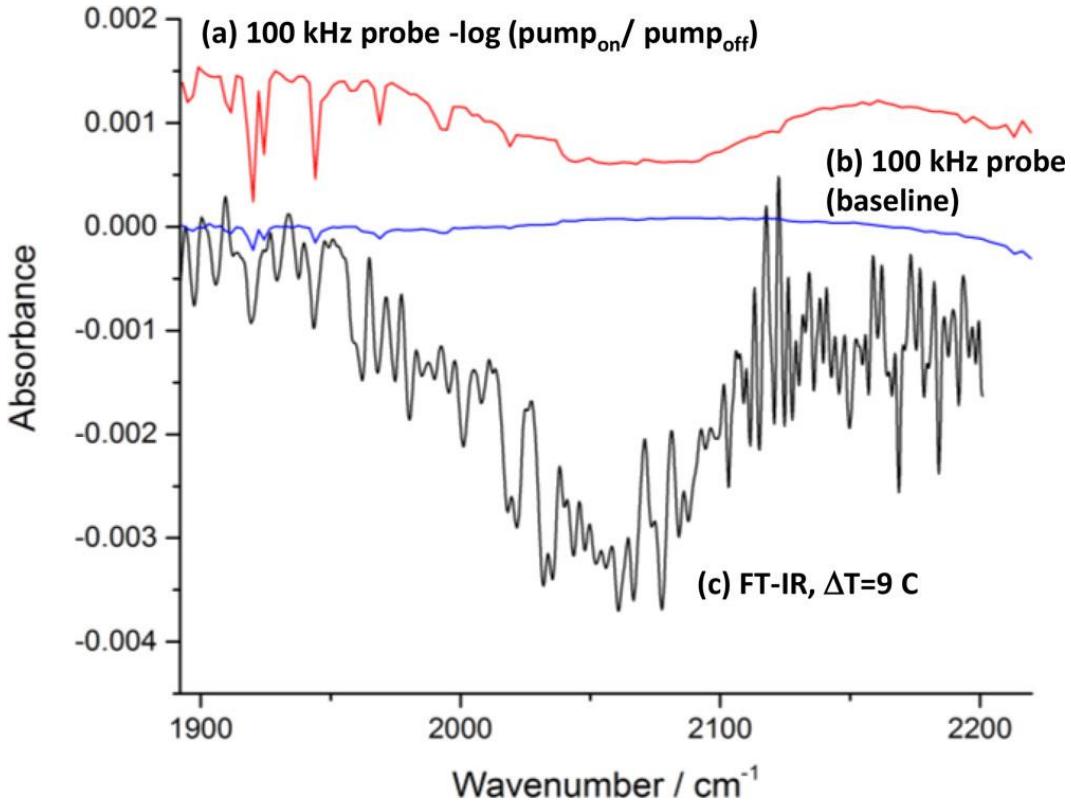

Figure 1.10 Comparing the effects of temperature on the IR spectra of NaSCN. (a) 100 kHz pump and probe pulses on the chemical system.(b) Just the 100 kHz probe pulse. (c) A FTIR spectrum of the chemical sample with the temperature raised 9°C. The baseline differences between (a) and(b) are believed to be due to laser fluctuations not a heating processes[76]. Figure reproduced from Ref. 65.

Heating in samples is a function of how strongly the sample absorbs at the frequencies it is being driven with, as well as the heat capacity of the solvent. Sample heating has been explored by investigating sodium thiocyanate (NaSCN) in a variety of sol-vents including ionic liquids, water, and organic solvents[76]. The ionic liquid data is shown in Fig. 1.10. In Fig. 1.10 plot (a)shows the response from the system when it is pumped, (b) is the spectrum of the system with only the probe

present, and (c) is of the sample in a temperature-controlled cell collected in an FTIR heated 9°C above room temperature. These data show that for samples that are pumped, there is an increase in the bleach at~2050 cm^{-1}. These results suggest that the pump is thermally exciting vibrational modes from the ground state to the first excited state. However, this heating is likely only a few degrees, because when the spectrum is compared to the one collected from the sample heated in the temperature-controlled cell in the FTIR spectrometer, they are very different. These experimental efforts also realized approaches to avoid heating in samples. It was noted that NaSCN in water experienced some thermal effects, but a more extreme result was the observation that the pump pulse boiled the organic solvent. Rastering the sample provided a solution to this problem. Therefore, although high average powers generated by operating at 100 kHz can affect the data collected, it will depend on the sample and can be avoided by rastering the sample as needed.

1.4.2 Optical

2D IR reports on the correlation between the state prepared by two pump pulses and a probe pulse. In practice, 2D IR can be performed in the frequency domain[78], time domain[79],or in mixed frequency domain-time domain experiments[80]. In this review, the authors will focus on advancements made in time domain experiments. The general pulse sequence that is used is shown in Fig. 1.11. As shown in Fig. 1.11, each pulse has a corresponding wave vector denoted as k1, k2 and k3whichdescribes the direction of the pulse; there are also three time intervals denoted. First

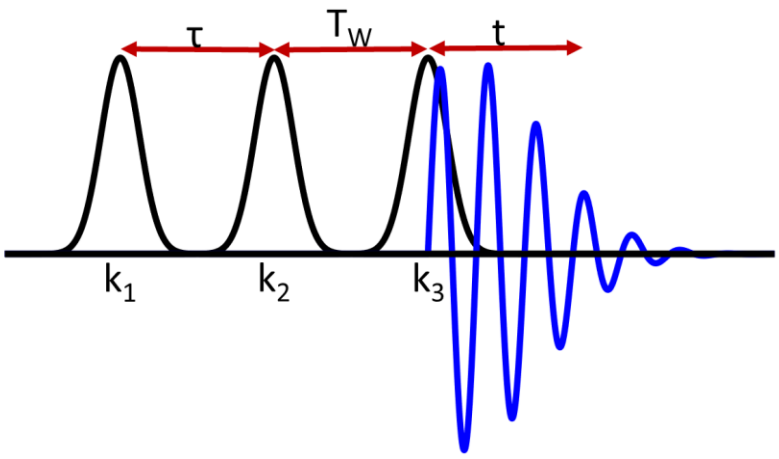

Figure 1.11 Pulse sequence used in a 2D IR experiment. Pulses with k vectors 1 and 2 are the pump pulses separated by time τ. Pulse with k vector 3 is the probe pulse and is separated from the last pump pulse by time TW. The blue decay represents the emitted signal field that occurs at time t after the probe pulse.

is the time interval between the first wo pump pulses, the correlation time labeled as τ. Next is the time interval between the last pump pulse and the probe pulse, referred to as the population time and denoted as Tw. The last time interval is between the probe pulse and the emitted signal field, referred to as the detection time, t. The two pump pulses are scanned from τ equal to zero and out to τ equal to several picoseconds; the time steps, Δτ, typically range from a few to tens of femtoseconds. At each value of τ the probe pulse interacts with the molecular sample, thus probing the state that the two pulses generated. Thus, a free induction decay of all the frequencies present within the bandwidth of the pulses is traced out in this process. In practice, these experiments are realized with two different optical geometries—the BOXCAR and pump probe geometries. The BOXCAR geometry involves having each pulse in the pulse sequence on its own input line, and therefore each have a unique wave vector direction. The emitted signal will then be emitted with a new, unique wave vector, k4, that is picked off and sent to the detector. The BOXCAR geometry provides the benefit of having control over the polarization of each pulse in the experiment; having this level of control allows for a wider variety of experiments that explore the polarization

dependent excitation pathways in a chemical system[71]. Another benefit of the BOXCAR geometry is that it is a background free experiment. The background free nature of this beam geometry comes from the emitted signal having a different wave vector than the three input pulses. Often a fourth pulse is employed to act as a local oscillator in the BOXCAR geometry to heterodyne the signal; the heterodyned detection allows phase information to be retained in the experiment and the local oscillator also amplifies the signal, thus aiding in signal detection. 2D IR spectra produced with a pump-probe geometry can use two different means of generating the pump pulses, interferometry or pulse shaping. In this review we will focus on the pulse shaping technique due to the direct impact pulse shaping has had on improving 2D IR acquisition rates. Pulse shaping involves modulating the amplitude and phase of individual frequencies to produce the pulse pair required for 2D IR spectroscopy. Un-like the previously discussed BOXCAR beam geometry, both pump pulses come in on the same input line, and therefore have the same wave vector direction. This allows for ease in alignment but limits the polarization dependent studies that can be

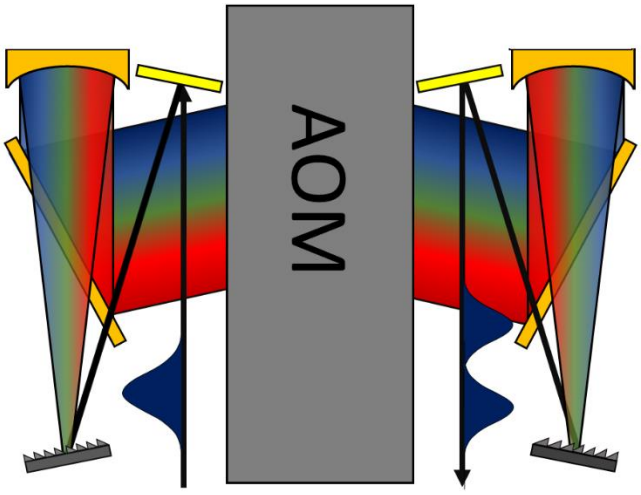

Figure 1.12 Example of an optical layout used for a pulse shaper. A pulse shaper takes the input pulse (left side) to be phase and amplitude modulated such that the output of the shaper is two pulses.

performed. Shaping in the mid IR requires frequency resolving the optical pulse and manipulating the phase and amplitude of the pulse's constituent wavelengths. This can be done using an acoustic optical modulator (AOM). A typical optical geometry for a mid-IR pulse shaper is drawn in Fig. 1.12. In Fig. 1.12 the input optical pulse is frequency dispersed using a grating. This light is then collimated using a cylindrical mirror and reflected down onto a flat mirror directing the light onto the AOM. Within the AOM the optical wavelengths interact with an acoustic wave, called a mask, that is propagating though a crystal. The acoustic mask modulates the amplitude and phase of the individual wavelengths. The optical output of the AOM is then directed up to a second cylindrical mirror, by way of a flat mirror, and onto a second grating, resulting in the output being a recollimated beam with the pulses in the time domain. A key advantage to pulse shaping is the ability to control the phase of each pump pulse. The phase and amplitude control over the pump pulses is achieved because the phase and amplitude of frequencies that make up the longitudinal wave are written onto the optical frequencies. An equation for the longitudinal wave, or mask is shown in (1.11). In (1.11) M(ω)is a mask written as a function of the center frequency of the optical

$$M(\omega) = \frac{1}{2}\left(e^{i\omega\tau}e^{i\phi_1} + e^{i\phi_2}\right) \qquad (1.11)$$

pulse, ω, the time between the two pump pulses, τ, and the phases, φ_i, for pulses 1 and 2. The detected 2D IR signal is a function of the relative phase of the pump pulses[13,81], specifically φ1–φ2 which can be written as $\Delta\varphi_{12}$.Therefore, changing φ_1 and φ_2 in (1.11) will change the phase of the detected signal. This is an important property that allows for improved data collection[82]. The ability to change$\Delta\varphi_{12}$ allows for phase cycling, a technique that drastically improves the signal to noise ratio in a dataset and removes unwanted nonlinear artifacts in the data[82,83]. Phase cycling can provide these benefits because the detected signal from the sample is a function of the relative

phase of the two pump pulses, while other nonlinear signals such as a transient absorption are not affected by the relative phase of the pump pulses. The relative phase will typically be either 0 or π. In a practice, implementing phase cycling involves collecting one data set for all values of τ with $\Delta\varphi_{12}$ equal to 0, and then another data set for all values of τ with $\Delta\varphi_{12}$

Table 1.1. Relative Phases for Each Pulse in Each Frame

Frame Number	ϕ of pump pulse 1	ϕ of pump pulse 2
Frame 1	0	0
Frame 2	0	π
Frame 3	π	π
Frame 4	π	0

equal to π. Then the two data sets are subtracted from one another. This is referred to as two frame phase cycling, because there are two different values of $\Delta\varphi_{12}$ used. The subtraction will remove any transient absorption signal that is present, while at the same time doubling the intensity of the 2D IR signal. To further sup-press the noise a four-frame phase cycling scheme can be used. Table I lists out the different values of $\Delta\varphi_{12}$ and (1.12) provides the phase math used to isolate the signal.

$$DataOutput = (Frame\ 1 - Frame\ 2) + (Frame\ 3 - Frame\ 4) \qquad (1.12)$$

Depending on the beam geometry and the sample of interest, simple four-frame phase cycling may not be enough to remove unwanted features from a data set. For example, scatter from a sample can produce a spectral feature that appears along the di-agonal of the data. This feature is due to interactions between the two pump pulses. Furthermore, signals from each pump pulse individually interacting with the probe pulse can also appear in the spectra[81]. Investigators can turn to eight-frame phase cycling to remove these unwanted features. In these schemes, two consecutive

four frame phase cycling schemes are performed back to back for each value of τ and the probe beam line is chopped. Finally, the chopped and unchopped signals are subtracted to isolate the signal. It should be noted that phase cycling schemes have also been developed for higher order spectroscopies and can be adapted to suit the needs of the experiment[84]. Faster acquisition times are achieved by removing the need for mechanical stages and implementing the use of a rotating frame. When collecting a 2D IR spectrum Δτ needs to be small enough to satisfy the Nyquist frequency of the highest frequency vibrational mode that is being probed. For example, Δτ needs to be 10 fs or less to probe vibrational modes at 1666 cm^{-1}. Therefore, many timesteps of τ are required, and consequently the acquisition time in the experiment is increased to have satisfactory resolution in a 2D IR spectrum. By implementing rotating frame, under sampling of the free induction decay can be achieved, while still preserving the third order signal[85,86]. Though there are many benefits to using pulse shaping, issues do arise especially with broad bandwidth pulses. The next section will look at these issues and approaches to correct them. To shape in the mid-IR the typical AOM is made with a 10 mm by 55 mm germanium crystal that the mask travels down. As the mask propagates though the crystal it creates different regions of density in the germanium crystal making what is in effect a transmission grating. Since the AOM acts as a transmission grating the input beam coming from the flat mirror is rotated ∼2°to allow for the first order signal to be reflected to the second flat mirror. The ∼2°angle comes from the Bragg equation, as shown in (13). In (13) θ is the transmission angle, λ is the center wavelength of the

$$sin(\theta) = \frac{\lambda \upsilon_{RF}}{2U_{ac}} \tag{1.13}$$

optical pulse, ν_{RF} is frequency of the mask, and U_{ac} is the speed of sound in the material. From this equation an important issue can be seen for broad band-width pulses the further the wavelengths

are from the center frequency the greater the difference of the transmission angles become. This results in angular dispersion of the light, because all wavelengths do not exit the AOM in the same direction. To get around this issue ν_{RF} can be changed from being a constant frequency to one that is varied across the germanium crystal. This results in θ being constant for all wavelengths[79,87]. The germanium crystal will also chirp the beam, a problem that is especially true for broadband pulses. Germanium willput~698 fs2/mm of group velocity dispersion (GVD) on a 6000 nm pulse[88]. This amount of GVD will put enough chirp on the pulse to turn a femtosecond pulse into a picosecond pulse. Two approaches can be taken to correct for this problem. First, germanium puts positive GVD on the pulse, therefore, placing a material window with negative GVD, such as calcium fluoride (CaF_2)[89], in the beam path will help to compensate for this material dispersion. Secondly, just like with correcting for the different Bragg angles discussed above, using a chirped mask will cause individual wavelengths to be reflected at slightly different angles. This results in each wavelength taking slightly different beam paths thought the shaper and thus, reversing the chirp that the germanium put on the pulse. Continuing to develop a deeper understanding of pulse shaping across the entire wavelength spectrum from the deep UV to the far IR will lead to the ability to implement pulse shaping in many emerging spectroscopy techniques outside of the visible and mid-IR wavelength regions.

1.5 New Opportunities in the Field

A long-standing advantage of 2D IR spectroscopy has been the fact that samples of interest can be in their natural environment; one of the few molecular environments 2D IR spectroscopy has yet to be applied to is the gas phase environment. Therefore, 2DIR spectroscopy is a potentially powerful tool to investigate heterogeneous systems. However, dynamics in biological systems and materials science applications can span decades in time. For example, in RTILs chemical dynamics

that govern local ionic conductivity occur on femtosecond to 10 s of picosecond timescales, while dynamics that govern diffusion and transport of an ion pair occur at much longer times in the nanosecond to microsecond timescales and longer. Emerging techniques to extend the utility of 2D IR spectroscopy to examine time dynamics beyond picosecond and into the nanosecond time regime are crucial to continue to exploit 2D IR spectroscopy to study heterogeneous systems. One approach has been to exploit the long vibrational lifetimes of pseudohalides, including SCN and SeCN among others, to utilize 2D IR spectroscopy to monitor dynamics from femtosecond to nanosecond timescales. For ex-ample, recent work utilizing selenocyanate based probes have provided a quantitative picture of dynamics in RTILs and fragile glasses well into the nanosecond timescales[42,90]. A second approach is to extend vibrational lifetimes of oscillators native to system by employing different pulse sequences to perform 2DIR spectroscopy. VIPER Spectroscopy is an emerging technique that is a promising approach to extending the time window of dynamics that can be monitored, as well as provide new information related to energy flow within a molecular system.

1.5.1 VIPER Spectroscopy

Exploring the dynamics of certain chemical systems can be a challenge due to their short vibrational lifetimes. 2D IR spectroscopy can only probe chemical dynamics that occur within the vibrational lifetime of the oscillator employed during an experiment. Thus, investigators have explored the use of oscillators that have very long vibrational lifetimes as probes[91]. Alternatively, new spectroscopic approaches can be developed to extend the dynamical timescales accessible by coherent multidimensional spectroscopy techniques. One such spectroscopic approach is vibrationally promoted electronic resonance spectroscopy (VIPERS)[92]. VIPERS utilizes a UV/Vis

pulse to excite molecules into the first electronic excited state which allows access to longer lifetimes. VIPERS experiments begin with an IR pulse to selectively excite certain

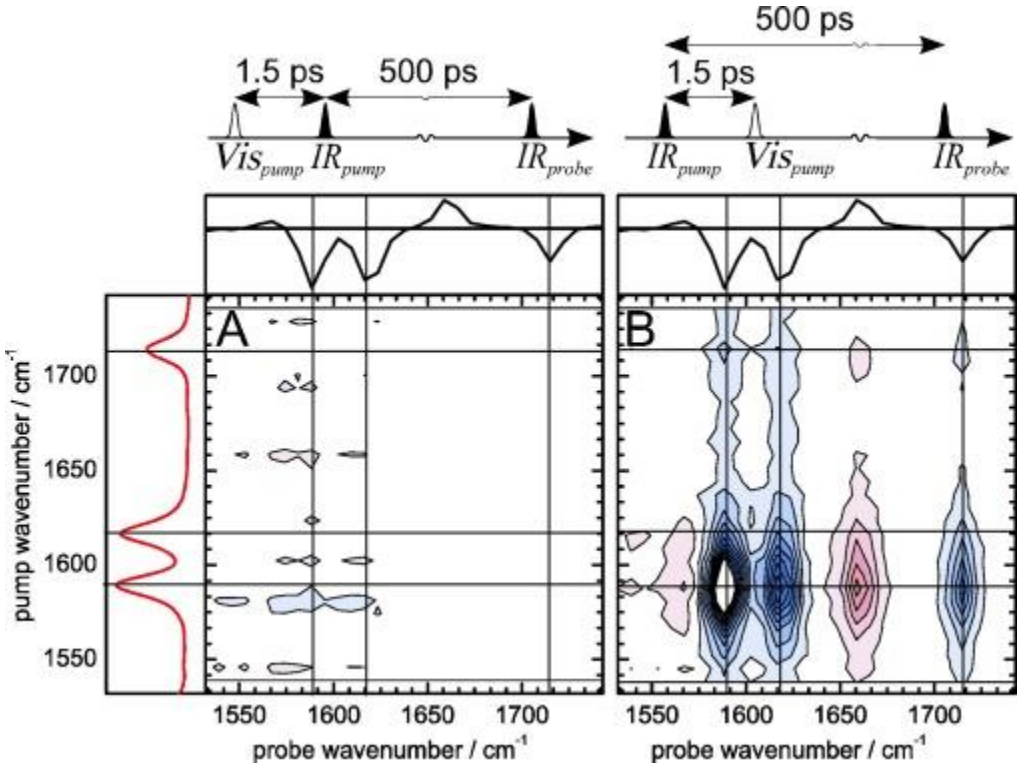

Figure 1.13 Comparing the pulse ordering that is used in VIPERS experiments by reversing the order of the pump pulses. (A) the first pump pulse is a UV/Vis pulse and (C) the first pump pulse is an IR pulse. After a delay of 500 ps between each IR pulse, it can be seen the VIPERS pulse sequence, (B), provides the longer observed signal[93]. Figure reproduced from Ref. 82.

vibrational modes to the first excited state. The population that is in the first ex-cited state is then excited with a UV/Vis pulse. It is important to note that this pulse is only resonant with the first vibrational excited state and the first excited state, meaning the molecules left in the ground state will not be promoted to the first electronic excited state. This in effect writes the information carried in the vibration onto the much longer lifetime of the electronic state. Therefore, much longer waiting times can be used in experiments. VIPERS is particularly useful to monitor chemical exchange processes across femtosecond to nanosecond times and potentially longer. The utility of a VIPERS experiment is demonstrated with an investigation of coumarin 6, (C6). The

goal of the work was to see if the extended vibrational life time offered by VIPERS could provide more information on the chemical exchange processes between a hydrogen bonded carbonyl and a non-hydrogen bonded, or free, carbonyl[93]. Testing the pulse sequence is necessary to determine if the increased detection time comes only from the addition of a UV/Vis pulse or if it is due to the timing of the UV/Vis excitation at the sample relative to the IR pulses. A VIPERS pulse sequence, Fig. 1.13(B), was compared to a pulse sequence where the first excitation was the UV/Vis pulse, Fig. 1.13(A). This data clearly shows the larger signal strength in the VIPERS pulse sequence after 500 ps. Therefore, the pulse sequence used does influence the resulting data. It was crucial to determine whether the vibrational properties of C6 were perturbed in VIPERS experiments. Thus, experiments were conducted to compare the results for vibrational lifetimes of the ring modes of C6 with traditional 2D IR spectroscopy techniques. Vibrational lifetimes were found to be 2 ps and 9 ps; these results were comparable to the lifetimes observed with 2D IR. After confirming the results of VIPERS, the chemical exchange dynamics could be studied. Moreover, analysis of the cross peaks between the free and hydrogen bonded carbonyl modes revealed that the chemical exchange processes extended for at least 77 ps. Processes occurring on long time scales like these would not be possible to observe on the coumarin directly with traditional 2D IR spectroscopy techniques. VIPERS is a promising technique to dramatically expand the timescales of dynamics that can be observed. As the time window for observed dynamics is expanded, the spectrometers employed will need to have high signal-to-noise ratios and rapid acquisition rates in order to apply VIPERS to heterogeneous condensed phase systems. Thus, it is expected that the efforts in further developing pulse-shaping and the recent move towards high repetition rate laser sources will crucial technological advancements for 2D IR spectroscopy.

1.6 Closing Remarks

In closing, efforts by investigators involved with technology development continue to impact 2D IR spectroscopy, as well as other types of coherent multidimensional spectroscopy techniques. Advances in pulse-shaping and mid-IR laser source technologies will continue to push 2D IR spectroscopy and 2DIR microspectroscopy to be applied to study heterogeneous systems in which chemical structure and dynamics will yield in-sights into function of the systems of interest. Advancements in detection systems will likely lead to another generation of innovation in the field of 2D IR spectroscopy.

References

(1) Kuhs, C.; Luther, B.; Krummel, A. Recent Advances in 2D IR Spectroscopy Driven by Advances in Ultrafast Technology. *IEEE Journal of Selected Topics in Quantum Electronics* **2019**, 1–1. https://doi.org/10.1109/JSTQE.2019.2900597.

(2) Zhu, P.; Yan, X.; Su, Y.; Yang, Y.; Li, J. Solvent-Induced Structural Transition of Self-Assembled Dipeptide: From Organogels to Microcrystals. *Chem. Eur. J.* **2010**, *16* (10), 3176–3183. https://doi.org/10.1002/chem.200902139.

(3) Bonmatin, J.-M.; Genest, M.; Labbé, H.; Ptak, M. Solution Three-Dimensional Structure of Surfactin: A Cyclic Lipopeptide Studied by 1H-Nmr, Distance Geometry, and Molecular Dynamics. *Biopolymers* **1994**, *34* (7), 975–986. https://doi.org/10.1002/bip.360340716.

(4) Losonczi, JuditA.; Prestegard, JamesH. Improved Dilute Bicelle Solutions for High-Resolution NMR of Biological Macromolecules. *J. Biomol. NMR* **1998**, *12* (3), 447–451. https://doi.org/10.1023/A:1008302110884.

(5) MacKenzie, K. J. D.; Smith, M. E. *Multinuclear Solid-State NMR of Inorganic Materials*, 1st ed.; Pergamon materials series; Pergamon: Oxford ; New York, 2002.

(6) Fayer, M. D.; Moilanen, D. E.; Wong, D.; Rosenfeld, D. E.; Fenn, E. E.; Park, S. Water Dynamics in Salt Solutions Studied with Ultrafast Two-Dimensional Infrared (2D IR) Vibrational Echo Spectroscopy. *Acc. Chem. Res.* **2009**, *42* (9), 1210–1219. https://doi.org/10.1021/ar900043h.

(7) Feng, C.-J.; Tokmakoff, A. The Dynamics of Peptide-Water Interactions in Dialanine: An Ultrafast Amide I 2D IR and Computational Spectroscopy Study. *The Journal of Chemical Physics* **2017**, *147* (8), 085101. https://doi.org/10.1063/1.4991871.

(8) Kwak, K.; Park, S.; Finkelstein, I. J.; Fayer, M. D. Frequency-Frequency Correlation Functions and Apodization in Two-Dimensional Infrared Vibrational Echo Spectroscopy: A New Approach. *The Journal of Chemical Physics* **2007**, *127* (12), 124503. https://doi.org/10.1063/1.2772269.

(9) Ghosh, A.; Ostrander, J. S.; Zanni, M. T. Watching Proteins Wiggle: Mapping Structures with Two-Dimensional Infrared Spectroscopy. *Chemical Reviews* **2017**, *117* (16), 10726–10759. https://doi.org/10.1021/acs.chemrev.6b00582.

(10) Krummel, A. T.; Zanni, M. T. DNA Vibrational Coupling Revealed with Two-Dimensional Infrared Spectroscopy: Insight into Why Vibrational Spectroscopy Is Sensitive to DNA Structure. *J. Phys. Chem. B* **2006**, *110* (28), 13991–14000. https://doi.org/10.1021/jp062597w.

(11) Khalil, M.; Demirdöven, N.; Tokmakoff, A. Vibrational Coherence Transfer Characterized with Fourier-Transform 2D IR Spectroscopy. *The Journal of Chemical Physics* **2004**, *121* (1), 362. https://doi.org/10.1063/1.1756870.

(12) Gaynor, J. D.; Khalil, M. Signatures of Vibronic Coupling in Two-Dimensional Electronic-Vibrational and Vibrational-Electronic Spectroscopies. *The Journal of Chemical Physics* **2017**, *147* (9), 094202. https://doi.org/10.1063/1.4991745.

(13) Hamm, P.; Zanni, M. T. *Concepts and Methods of 2D Infrared Spectrscopy*, First.; Cambridge Univesrity Press: Cambridge, New York, 2011.

(14) Cyran, J. D.; Krummel, A. T. Probing Structural Features of Self-Assembled Violanthrone-79 Using Two Dimensional Infrared Spectroscopy. *The Journal of Chemical Physics* **2015**, *142* (21), 212435. https://doi.org/10.1063/1.4919637.

(15) Finkelstein, I. J.; Zheng, J.; Ishikawa, H.; Kim, S.; Kwak, K.; Fayer, M. D. Probing Dynamics of Complex Molecular Systems with Ultrafast 2D IR Vibrational Echo Spectroscopy. *Phys. Chem. Chem. Phys.* **2007**, *9* (13), 1533–1549. https://doi.org/10.1039/B618158A.

(16) Mattson, M. A.; Green, T. D.; Lake, P. T.; McCullagh, M.; Krummel, A. T. Elucidating Structural Evolution of Perylene Diimide Aggregates Using Vibrational Spectroscopy and Molecular Dynamics Simulations. *The Journal of Physical Chemistry B* **2018**, *122* (18), 4891–4900. https://doi.org/10.1021/acs.jpcb.8b02355.

(17) Guo, Q.; Pagano, P.; Li, Y.-L.; Kohen, A.; Cheatum, C. M. Line Shape Analysis of Two-Dimensional Infrared Spectra. *The Journal of Chemical Physics* **2015**, *142* (21), 212427. https://doi.org/10.1063/1.4918350.

(18) Kim, Y. S.; Hochstrasser, R. M. Chemical Exchange 2D IR of Hydrogen-Bond Making and Breaking. *PNAS* **2005**, *102* (32), 11185–11190. https://doi.org/10.1073/pnas.0504865102.

(19) Moilanen, D. E.; Wong, D.; Rosenfeld, D. E.; Fenn, E. E.; Fayer, M. D. Ion–Water Hydrogen-Bond Switching Observed with 2D IR Vibrational Echo Chemical Exchange Spectroscopy. *PNAS* **2009**, *106* (2), 375–380. https://doi.org/10.1073/pnas.0811489106.

(20) Oudar, J.-L.; Shen, Y. R. Nonlinear Spectroscopy by Multiresonant Four-Wave Mixing. *Physical Review A* **1980**, *22* (3), 1141–1158. https://doi.org/10.1103/PhysRevA.22.1141.

(21) Yan, Y. J.; Fried, L. E.; Mukamel, S. Ultrafast Pump-Probe Spectroscopy: Femtosecond Dynamics in Liouville Space. *The Journal of Physical Chemistry* **1989**, *93* (25), 8149–8162. https://doi.org/10.1021/j100362a006.

(22) Hybl, J. D.; Albrecht, A. W.; Faeder, S. M. G.; Jonas, D. M. Two-Dimensional Electronic Spectroscopy. **1998**, 7.

(23) Hamm, P.; Lim, M.; Hochstrasser, R. M. Structure of the Amide I Band of Peptides Measured by Femtosecond Nonlinear-Infrared Spectroscopy. *The Journal of Physical Chemistry B* **1998**, *102* (31), 6123–6138. https://doi.org/10.1021/jp9813286.

(24) Courtney, T. L.; Fox, Z. W.; Estergreen, L.; Khalil, M. Measuring Coherently Coupled Intramolecular Vibrational and Charge-Transfer Dynamics with Two-Dimensional Vibrational–Electronic Spectroscopy. *The Journal of Physical Chemistry Letters* **2015**, *6* (7), 1286–1292. https://doi.org/10.1021/acs.jpclett.5b00356.

(25) Oliver, T. A. A.; Lewis, N. H. C.; Fleming, G. R. Correlating the Motion of Electrons and Nuclei with Two-Dimensional Electronic-Vibrational Spectroscopy. *Proceedings of the National Academy of Sciences* **2014**, *111* (28), 10061–10066. https://doi.org/10.1073/pnas.1409207111.

(26) Xiong, W.; Laaser, J. E.; Mehlenbacher, R. D.; Zanni, M. T. Adding a Dimension to the Infrared Spectra of Interfaces Using Heterodyne Detected 2D Sum-Frequency Generation (HD 2D SFG) Spectroscopy. *Proceedings of the National Academy of Sciences* **2011**, *108* (52), 20902–20907. https://doi.org/10.1073/pnas.1115055108.

(27) Singh, P. C. 2D Heterodyne-Detected Sum Frequency Generation Study on the Ultrafast Vibrational Dynamics of H_2O and HOD Water at Charged Interfaces. *The Journal of Chemical Physics* **2015**, *142* (21), 212431. https://doi.org/10.1063/1.4918644.

(28) Fayer, M. D. Dynamics of Liquids, Molecules, and Proteins Measured with Ultrafast 2D IR Vibrational Echo Chemical Exchange Spectroscopy. *Annual Review of Physical Chemistry* **2009**, *60* (1), 21–38. https://doi.org/10.1146/annurev-physchem-073108-112712.

(29) Donten, M. L.; Hamm, P. PH-Jump Induced α-Helix Folding of Poly-l-Glutamic Acid. *Chemical Physics* **2013**, *422*, 124–130. https://doi.org/10.1016/j.chemphys.2012.11.023.

(30) Kratochvil, H. T.; Carr, J. K.; Matulef, K.; Annen, A. W.; Li, H.; Maj, M.; Ostmeyer, J.; Serrano, A. L.; Raghuraman, H.; Moran, S. D.; et al. Instantaneous Ion Configurations in the K^+ Ion Channel Selectivity Filter Revealed by 2D IR Spectroscopy. *Science* **2016**, *353* (6303), 1040–1044. https://doi.org/10.1126/science.aag1447.

(31) Yan, C.; Nishida, J.; Yuan, R.; Fayer, M. D. Water of Hydration Dynamics in Minerals Gypsum and Bassanite: Ultrafast 2D IR Spectroscopy of Rocks. *Journal of the American Chemical Society* **2016**, *138* (30), 9694–9703. https://doi.org/10.1021/jacs.6b05589.

(32) Rosenfeld, D. E.; Gengeliczki, Z.; Smith, B. J.; Stack, T. D. P.; Fayer, M. D. Structural Dynamics of a Catalytic Monolayer Probed by Ultrafast 2D IR Vibrational Echoes. *Science* **2011**, *334* (6056), 634–639. https://doi.org/10.1126/science.1211350.

(33) Woutersen, S.; Hamm, P. Isotope-Edited Two-Dimensional Vibrational Spectroscopy of Trialanine in Aqueous Solution. *The Journal of Chemical Physics* **2001**, *114* (6), 2727–2737. https://doi.org/10.1063/1.1336807.

(34) Smith, A. W.; Lessing, J.; Ganim, Z.; Peng, C. S.; Tokmakoff, A.; Roy, S.; Jansen, T. L. C.; Knoester, J. Melting of a β-Hairpin Peptide Using Isotope-Edited 2D IR Spectroscopy and Simulations. *The Journal of Physical Chemistry B* **2010**, *114* (34), 10913–10924. https://doi.org/10.1021/jp104017h.

(35) Sun, Z.; Zhang, W.; Ji, M.; Hartsock, R.; Gaffney, K. J. Contact Ion Pair Formation between Hard Acids and Soft Bases in Aqueous Solutions Observed with 2DIR Spectroscopy. *The Journal of Physical Chemistry B* **2013**, *117* (49), 15306–15312. https://doi.org/10.1021/jp4033854.

(36) Moran, S. D.; Zanni, M. T. How to Get Insight into Amyloid Structure and Formation from Infrared Spectroscopy. *The Journal of Physical Chemistry Letters* **2014**, *5* (11), 1984–1993. https://doi.org/10.1021/jz500794d.

(37) Dunkelberger, E. B.; Grechko, M.; Zanni, M. T. Transition Dipoles from 1D and 2D Infrared Spectroscopy Help Reveal the Secondary Structures of Proteins: Application to Amyloids. *The Journal of Physical Chemistry B* **2015**, *119* (44), 14065–14075. https://doi.org/10.1021/acs.jpcb.5b07706.

(38) Ghosh, A.; Qiu, J.; DeGrado, W. F.; Hochstrasser, R. M. Tidal Surge in the M2 Proton Channel, Sensed by 2D IR Spectroscopy. *Proceedings of the National Academy of Sciences* **2011**, *108* (15), 6115–6120. https://doi.org/10.1073/pnas.1103027108.

(39) Tokmakoff, A.; Fayer, M. D. Homogeneous Vibrational Dynamics and Inhomogeneous Broadening in Glass-forming Liquids: Infrared Photon Echo Experiments from Room Temperature to 10 K. *The Journal of Chemical Physics* **1995**, *103* (8), 2810–2826. https://doi.org/10.1063/1.470517.

(40) Ramasesha, K.; Roberts, S. T.; Nicodemus, R. A.; Mandal, A.; Tokmakoff, A. Ultrafast 2D IR Anisotropy of Water Reveals Reorientation during Hydrogen-Bond Switching. *The Journal of Chemical Physics* **2011**, *135* (5), 054509. https://doi.org/10.1063/1.3623008.

(41) Ghosh, A.; Remorino, A.; Tucker, M. J.; Hochstrasser, R. M. 2D IR Photon Echo Spectroscopy Reveals Hydrogen Bond Dynamics of Aromatic Nitriles. *Chemical Physics Letters* **2009**, *469* (4–6), 325–330. https://doi.org/10.1016/j.cplett.2008.12.094.

(42) Hoffman, D. J.; Sokolowsky, K. P.; Fayer, M. D. Direct Observation of Dynamic Crossover in Fragile Molecular Glass Formers with 2D IR Vibrational Echo Spectroscopy. *The Journal of Chemical Physics* **2017**, *146* (12), 124505. https://doi.org/10.1063/1.4978852.

(43) Thamer, M.; De Marco, L.; Ramasesha, K.; Mandal, A.; Tokmakoff, A. Ultrafast 2D IR Spectroscopy of the Excess Proton in Liquid Water. *Science* **2015**, *350* (6256), 78–82. https://doi.org/10.1126/science.aab3908.

(44) Dutta, S.; Ren, Z.; Brinzer, T.; Garrett-Roe, S. Two-Dimensional Ultrafast Vibrational Spectroscopy of Azides in Ionic Liquids Reveals Solute-Specific Solvation. *Phys. Chem. Chem. Phys.* **2015**. https://doi.org/10.1039/C5CP02119G.

(45) *Ultrafast Infrared and Raman Spectrscopy*, 1st ed.; Michael Fayer, Ed.; Practical Spectrscopy Series; Marcel Dekker, Inc: New York, 2001; Vol. 26.

(46) Yan, Y. J.; Gillilan, R. E.; Whitnell, R. M.; Wilson, K. R.; Mukamel, S. Optical Control of Molecular Dynamics: Liouville-Space Theory. *The Journal of Physical Chemistry* **1993**, *97* (10), 2320–2333. https://doi.org/10.1021/j100112a038.

(47) Marroux, H. J. B.; Orr-Ewing, A. J. Distinguishing Population and Coherence Transfer Pathways in a Metal Dicarbonyl Complex Using Pulse-Shaped Two-Dimensional Infrared Spectroscopy. *J. Phys. Chem. B* **2016**, *120* (17), 4125–4130. https://doi.org/10.1021/acs.jpcb.6b02979.

(48) Loring, R. F.; Mukamel, S. Selectivity in Coherent Transient Raman Measurements of Vibrational Dephasing in Liquids. *The Journal of Chemical Physics* **1985**, *83* (5), 2116–2128. https://doi.org/10.1063/1.449302.

(49) Mukherjee, P.; Kass, I.; Arkin, I. T.; Zanni, M. T. Picosecond Dynamics of a Membrane Protein Revealed by 2D IR. *PNAS* **2006**, *103* (10), 3528–3533. https://doi.org/10.1073/pnas.0508833103.

(50) Demirdöven, N.; Khalil, M.; Tokmakoff, A. Correlated Vibrational Dynamics Revealed by Two-Dimensional Infrared Spectroscopy. *Physical Review Letters* **2002**, *89* (23). https://doi.org/10.1103/PhysRevLett.89.237401.

(51) Kramer, P. L.; Nishida, J.; Giammanco, C. H.; Tamimi, A.; Fayer, M. D. Observation and Theory of Reorientation-Induced Spectral Diffusion in Polarization-Selective 2D IR Spectroscopy. *The Journal of Chemical Physics* **2015**, *142* (18), 184505. https://doi.org/10.1063/1.4920949.

(52) Kwak, K.; Park, S.; Finkelstein, I. J.; Fayer, M. D. Frequency-Frequency Correlation Functions and Apodization in Two-Dimensional Infrared Vibrational Echo Spectroscopy: A New Approach. *The Journal of Chemical Physics* **2007**, *127* (12), 124503. https://doi.org/10.1063/1.2772269.

(53) Roberts, S. T.; Loparo, J. J.; Tokmakoff, A. Characterization of Spectral Diffusion from Two-Dimensional Line Shapes. *The Journal of Chemical Physics* **2006**, *125* (8), 084502. https://doi.org/10.1063/1.2232271.

(54) Fenn, E. E.; Fayer, M. D. Extracting 2D IR Frequency-Frequency Correlation Functions from Two Component Systems. *The Journal of Chemical Physics* **2011**, *135* (7), 074502. https://doi.org/10.1063/1.3625278.

(55) Park, S.; Kwak, K.; Fayer, M. D. Ultrafast 2D-IR Vibrational Echo Spectroscopy: A Probe of Molecular Dynamics. *Laser Phys. Lett.* **2007**, *4* (10), 704. https://doi.org/10.1002/lapl.200710046.

(56) King, J. T.; Kubarych, K. J. Site-Specific Coupling of Hydration Water and Protein Flexibility Studied in Solution with Ultrafast 2D-IR Spectroscopy. *Journal of the American Chemical Society* **2012**, *134* (45), 18705–18712. https://doi.org/10.1021/ja307401r.

(57) Hydrogen bond dynamics in aqueous NaBr solutions http://www.pnas.org/content/104/43/16731.full (accessed Jun 13, 2016).

(58) Tracy, K. M.; Barich, M. V.; Carver, C. L.; Luther, B. M.; Krummel, A. T. High-Throughput Two-Dimensional Infrared (2D IR) Spectroscopy Achieved by Interfacing Microfluidic Technology with a High Repetition Rate 2D IR Spectrometer. *The Journal of Physical Chemistry Letters* **2016**, *7* (23), 4865–4870. https://doi.org/10.1021/acs.jpclett.6b01941.

(59) Rogers, R. D.; Seddon, K. R. Ionic Liquids—Solvents of the Future? *Science* **2003**, *302* (5646), 792–793. https://doi.org/10.1126/science.1090313.

(60) Ghandi, K. A Review of Ionic Liquids, Their Limits and Applications. *Green and Sustainable Chemistry* **2014**, *04* (01), 44–53. https://doi.org/10.4236/gsc.2014.41008.

(61) Tamimi, A.; Bailey, H. E.; Fayer, M. D. Alkyl Chain Length Dependence of the Dynamics and Structure in the Ionic Regions of Room-Temperature Ionic Liquids. *The Journal of Physical Chemistry B* **2016**, *120* (30), 7488–7501. https://doi.org/10.1021/acs.jpcb.6b05397.

(62) Alexander, R.; Ko, E. C. F.; Parker, A. J.; Broxton, T. J. Solvation of Ions. XIV. Protic-Dipolar Aprotic Solvent Effects on Rates of Bimolecular Reactions. Solvent Activity Coefficients of Reactants and Transition States at 25°. *Journal of the American Chemical Society* **1968**, *90* (19), 5049–5069. https://doi.org/10.1021/ja01021a002.

(63) Hamm, P.; Woutersen, S. Coupling of the Amide I Modes of the Glycine Dipeptide. *Bulletin of the Chemical Society of Japan* **2002**, *75* (5), 985–988. https://doi.org/10.1246/bcsj.75.985.

(64) Demirdöven, N.; Cheatum, C. M.; Chung, H. S.; Khalil, M.; Knoester, J.; Tokmakoff, A. Two-Dimensional Infrared Spectroscopy of Antiparallel β-Sheet Secondary Structure. *J. Am. Chem. Soc.* **2004**, *126* (25), 7981–7990. https://doi.org/10.1021/ja049811j.

(65) Ham, S.; Cha, S.; Choi, J.-H.; Cho, M. Amide I Modes of Tripeptides: Hessian Matrix Reconstruction and Isotope Effects. *The Journal of Chemical Physics* **2003**, *119* (3), 1451–1461. https://doi.org/10.1063/1.1581855.

(66) Torii, H.; Tasumi, M. Ab Initio Molecular Orbital Study of the Amide I Vibrational Interactions between the Peptide Groups in Di- and Tripeptides and Considerations on the Conformation of the Extended Helix. *Journal of Raman Spectroscopy* **1998**, *29* (1), 81–86. https://doi.org/10.1002/(SICI)1097-4555(199801)29:1<81::AID-JRS214>3.0.CO;2-H.

(67) Rubtsov, I. V. Relaxation-Assisted Two-Dimensional Infrared (RA 2DIR) Method: Accessing Distances over 10 Å and Measuring Bond Connectivity Patterns. *Accounts of Chemical Research* **2009**, *42* (9), 1385–1394. https://doi.org/10.1021/ar900008p.

(68) Müller-Werkmeister, H. M.; Essig, M.; Durkin, P.; Budisa, N.; Bredenbeck, J. Towards Direct Measurement of Ultrafast Vibrational Energy Flow in Proteins. In *Ultrafast Phenomena XIX*; Yamanouchi, K., Cundiff, S., de Vivie-Riedle, R., Kuwata-Gonokami, M., DiMauro, L., Eds.; Springer International Publishing: Cham, 2015; Vol. 162, pp 535–538. https://doi.org/10.1007/978-3-319-13242-6_131.

(69) Moore, W. H.; Krimm, S. Transition Dipole Coupling in Amide I Modes of Bpolypeptides. *PNAS* **1975**, *72* (12), 4933–4935.

(70) Moran, A.; Mukamel, S. The Origin of Vibrational Mode Couplings in Various Secondary Structural Motifs of Polypeptides. *Proceedings of the National Academy of Sciences* **2004**, *101* (2), 506–510. https://doi.org/10.1073/pnas.2533089100.

(71) Hochstrasser, R. M. Two-Dimensional IR-Spectroscopy: Polarization Anisotropy E€ ects. *Chemical Physics* **2001**, 12.

(72) Zanni, M. T.; Ge, N.-H.; Kim, Y. S.; Hochstrasser, R. M. Two-Dimensional IR Spectroscopy Can Be Designed to Eliminate the Diagonal Peaks and Expose Only the Crosspeaks Needed for Structure Determination. *PNAS* **2001**, *98* (20), 11265–11270. https://doi.org/10.1073/pnas.201412998.

(73) Kearns, N. M.; Mehlenbacher, R. D.; Jones, A. C.; Zanni, M. T. Broadband 2D Electronic Spectrometer Using White Light and Pulse Shaping: Noise and Signal Evaluation at 1 and 100 KHz. *Optics Express* **2017**, *25* (7), 7869. https://doi.org/10.1364/OE.25.007869.

(74) Kanal, F.; Keiber, S.; Eck, R.; Brixner, T. 100-KHz Shot-to-Shot Broadband Data Acquisition for High-Repetition-Rate Pump–Probe Spectroscopy. *Optics Express* **2014**, *22* (14), 16965. https://doi.org/10.1364/OE.22.016965.

(75) Luther, B. M.; Tracy, K. M.; Gerrity, M.; Brown, S.; Krummel, A. T. 2D IR Spectroscopy at 100 KHz Utilizing a Mid-IR OPCPA Laser Source. *Optics Express* **2016**, *24* (4), 4117. https://doi.org/10.1364/OE.24.004117.

(76) Donaldson, P. M.; Greetham, G. M.; Shaw, D. J.; Parker, A. W.; Towrie, M. A 100 KHz Pulse Shaping 2D-IR Spectrometer Based on Dual Yb:KGW Amplifiers. *The Journal of Physical Chemistry A* **2018**, *122* (3), 780–787. https://doi.org/10.1021/acs.jpca.7b10259.

(77) Tracy, K. M.; Guchhait, B.; Tibbetts, C. A.; Luther, B. M.; Krummel, A. T. Visualizing Chemical Dynamics in an Ionic Liquid Microdroplet Using Ultrafast 2D IR Microscopy. *J.Phys.Chem.B* **2018**, *Submitted*.

(78) Pakoulev, A. V.; Rickard, M. A.; Mathew, N. A.; Kornau, K. M.; Wright, J. C. Frequency-Domain Time-Resolved Four Wave Mixing Spectroscopy of Vibrational Coherence

Transfer with Single-Color Excitation. *The Journal of Physical Chemistry A* **2008**, *112* (28), 6320–6329. https://doi.org/10.1021/jp711014h.

(79) Nite, J. M.; Cyran, J. D.; Krummel, A. T. Active Bragg Angle Compensation for Shaping Ultrafast Mid-Infrared Pulses. *Opt. Express, OE* **2012**, *20* (21), 23912–23920. https://doi.org/10.1364/OE.20.023912.

(80) Rickard, M. A.; Pakoulev, A. V.; Mathew, N. A.; Kornau, K. M.; Wright, J. C. Frequency- and Time-Resolved Coherence Transfer Spectroscopy. *The Journal of Physical Chemistry A* **2007**, *111* (7), 1163–1166. https://doi.org/10.1021/jp0677804.

(81) Baiz, C. R.; Schach, D.; Tokmakoff, A. Ultrafast 2D IR Microscopy. *Optics Express* **2014**, *22* (15), 18724. https://doi.org/10.1364/OE.22.018724.

(82) Shim, S.-H.; Zanni, M. T. How to Turn Your Pump–Probe Instrument into a Multidimensional Spectrometer: 2D IR and Vis Spectroscopies via Pulse Shaping. *Phys. Chem. Chem. Phys.* **2009**, *11* (5), 748–761. https://doi.org/10.1039/B813817F.

(83) Tan, H.-S.; Warren, W. S. Mid Infrared Pulse Shaping by Optical Parametric Amplification and Its Application to Optical Free Induction Decay Measurement. *Optics Express* **2003**, *11* (9), 1021. https://doi.org/10.1364/OE.11.001021.

(84) Tan, H.-S. Theory and Phase-Cycling Scheme Selection Principles of Collinear Phase Coherent Multi-Dimensional Optical Spectroscopy. *The Journal of Chemical Physics* **2008**, *129* (12), 124501. https://doi.org/10.1063/1.2978381.

(85) Xiong, W.; Zanni, M. T. Signal Enhancement and Background Cancellation in Collinear Two-Dimensional Spectroscopies. *Opt. Lett., OL* **2008**, *33* (12), 1371–1373. https://doi.org/10.1364/OL.33.001371.

(86) Strasfeld, D. B.; Ling, Y. L.; Gupta, R.; Raleigh, D. P.; Zanni, M. T. Strategies for Extracting Structural Information from 2D IR Spectroscopy of Amyloid: Application to Islet Amyloid Polypeptide. *The Journal of Physical Chemistry B* **2009**, *113* (47), 15679–15691. https://doi.org/10.1021/jp9072203.

(87) Wagner, W.; Li, C.; Semmlow, J.; Warren, W. S. Rapid Phase-Cycled Two-Dimensional Optical Spectroscopy in Fluorescence and Transmission Mode. *Optics Express* **2005**, *13* (10), 3697. https://doi.org/10.1364/OPEX.13.003697.

(88) Icenogle, H. W.; Platt, B. C.; Wolfe, W. L. Refractive Indexes and Temperature Coefficients of Germanium and Silicon. *Applied Optics* **1976**, *15* (10), 2348. https://doi.org/10.1364/AO.15.002348.

(89) Li, H. H. Refractive Index of Alkaline Earth Halides and Its Wavelength and Temperature Derivatives. *Journal of Physical and Chemical Reference Data* **1980**, *9* (1), 161–290. https://doi.org/10.1063/1.555616.

(90) King, J. T.; Ross, M. R.; Kubarych, K. J. Ultrafast α -Like Relaxation of a Fragile Glass-Forming Liquid Measured Using Two-Dimensional Infrared Spectroscopy. *Physical Review Letters* **2012**, *108* (15). https://doi.org/10.1103/PhysRevLett.108.157401.

(91) Mukherjee, P.; Krummel, A. T.; Fulmer, E. C.; Kass, I.; Arkin, I. T.; Zanni, M. T. Site-Specific Vibrational Dynamics of the CD3ζ Membrane Peptide Using Heterodyned Two-Dimensional Infrared Photon Echo Spectroscopy. *The Journal of Chemical Physics* **2004**, *120* (21), 10215–10224. https://doi.org/10.1063/1.1718332.

(92) von Cosel, J.; Cerezo, J.; Kern-Michler, D.; Neumann, C.; van Wilderen, L. J. G. W.; Bredenbeck, J.; Santoro, F.; Burghardt, I. Vibrationally Resolved Electronic Spectra

Including Vibrational Pre-Excitation: Theory and Application to VIPER Spectroscopy. *The Journal of Chemical Physics* **2017**, *147* (16), 164116. https://doi.org/10.1063/1.4999455.

(93) van Wilderen, L. J. G. W.; Messmer, A. T.; Bredenbeck, J. Mixed IR/Vis Two-Dimensional Spectroscopy: Chemical Exchange beyond the Vibrational Lifetime and Sub-Ensemble Selective Photochemistry. *Angewandte Chemie International Edition* **2014**, *53* (10), 2667–2672. https://doi.org/10.1002/anie.201305950.

Chapter 2

Materials and Methods

2.1 Introduction

The aim of this work was to use multidimensional spectroscopy to study the self-assembly processes of a variety of chemical systems. Two-dimensional IR spectroscopy requires three ultrafast pulses, two pumps and a probe pulse, to interact with the chemical sample at specific time intervals. To accomplish this, a time domain 2D IR spectrometer was built using a pulse shaper to generate the pump pulses. 2D IR experiments were then conducted that examined chemical exchange and population transfer of self-assembled systems.

This chapter details the various equipment, techniques, and sample preparation used in this thesis. First, this chapter presents a detailed look at the laser system, spectrometer, and pulse shaping techniques used to collect the necessary 2D spectra. This is followed by a discussion of 2D IR data analysis. Finally, an examination of linear spectroscopy techniques is discussed as well as a description of sample preparation.

2.2 Laser System

Generating the mid-IR light can be broken down into two parts: a Ti:Sapphire laser and an optical parametric amplifier (OPA). This section will detail both components explaining the different processes that are occurring in each step of the mid-IR light generation.

Ultrafast pulse generation starts with a KM-Wyvern 1000 Ti:Sapphire laser. This laser contains four parts: the oscillator, the stretcher, the amplifier, and the compressor as shown in Figure 2.1. The oscillator uses a Spectra Physics Millennium 532 nm continuous wave laser to

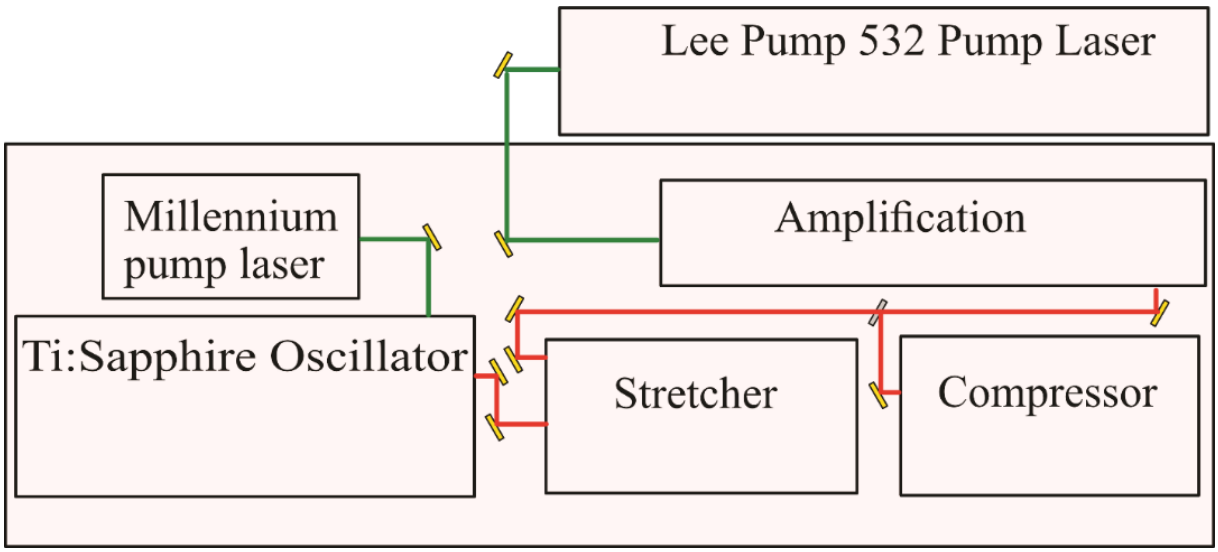

Figure 2.1 Optical layout for the Ti:Sapphire regenerative amplifier. This amplifier is used to generate the 790nm light that is used to pump the OPA.

pump a Ti:Sapphire crystal that generates a 75 MHz pulse train centered at 780 nm with 2 nJ of energy. The output of the oscillator, referred to as the seed beam, is then sent into a stretcher, which temporally chirps the beam. The pulse is stretched to prevent damaging optics, such as the gain medium, in the regenerative amplifier. After the seed is stretched, it is sent into the amplification stage. Here the seed is overlapped with Q-switched Lee pump laser operating at 1 kHz. The seed is trapped in the cavity approximately 19 ns before it is ejected from the cavity using a Pockel's cell. The amplified beam is then compressed and sent to pump the OPA. The final output of the Ti:Sapphire regenerative amplifier is a ~3 mJ 1 kHz beam centered at 790 nm.

Mid-IR light is generated using a Light Conversion TOPAS-C OPA. There are two sections in an OPA: first and second stage. Of the initial 3 mJ input beam from the Ti:Sapphire laser, 3% goes to the first stage, while the remining 97% is sent to the second amplification stage. In the first stage, the light is split again sending a portion for white light generation and a portion to pump the signal and idler beams generated in this step. Using a computer-controlled rotation stage, the signal and idler wavelengths are selected by rotating a beta barium borate (BBO) crystal. The signal and

idler are then amplified in the OPA's second stage by overlapping them with the remaining output from the Ti:Sapphire laser in a second BBO crystal. The amplified signal and idler are then sent to the difference frequency generation (DFG) crystal which can be angle-tuned to select the desired wavelength.

2.3 2D IR Spectrometer

The 2D IR spectrometer is configured in the pump probe geometry utilizing a pulse shaper to generate the pump pulses. A diagram of the spectrometer used can be seen in Figure 2.2. The output of the TOPAS-C is divided with a 90:10 zinc selenide wedge with 90% of the light going to the pulse shaper for the pump pulses and the other 10% of the mid-IR going into the probe pulse. In Figure 2.2 the probe beam path is traced out in a blue line and the pump beam path as a red line. The probe beam is on a delay line that utilizes a Newport XPS computer-controlled stage to adjust for temporal overlap and to conduct T-waiting experiments described below. Both pump and probe beams go through a 2x magnification telescope to allow for a tighter focus at the sample. The beams are focused onto the sample with a 4 inch off-axis parabolic mirror. The signal field generated at the sample follows the probe beam path and is frequency resolved on a 64-element mercury cadmium telluride (MCT) detector using a Horiba TRIAX 190 spectrometer. The voltage response from the MCT is sent to a Femtosecond Pulse Acquisition System (FPAS), where the analog signal is integrated and converted to a digital output.

The digital output is read out in a custom LabView program.

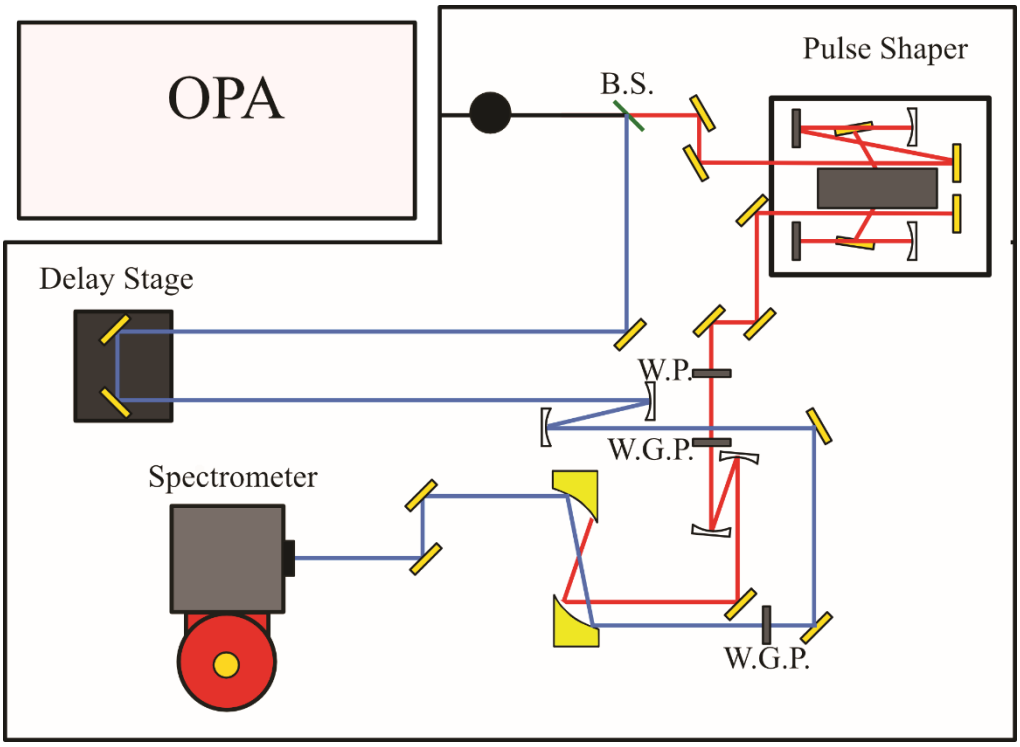

Figure 2.2 Optical layout of our home built 2D IR experiments. The spectrometer is in the pump probe optical configuration, employing a pulse shaper to generate the pump pulses. The blue line represents the probe beam geometry and the red line the pump pulses. In this figure, B.S. is the 90:10 beam splitter used to divided the OPA output into the pump and probe pulse line. W.P. is the half-waveplate used to rotate the polarization of the pump pulses for XXYY data collection. Two wire-grid polarizers, labeled W.G.P, used to clean up the polarization of both pump and probe pulse lines.

2.4 Pulse Shaping

2.4.1 Optical Geometry of a Pulse Shaper

Pulse shaping is an optical technique that allows for the manipulation of the phase and amplitude optical frequencies. In 2D IR, pulse shaping is used to generate pulse pairs in the time domain that pump a chemical sample. To generate the mid-IR pulse pair, a germanium-based pulse shaper is used to manipulate the amplitude and phase of the individual wavelengths that make up the input optical pulsed. This is accomplished by frequency resolving the pulse across an acoustic optical modulator (AOM). The optical geometry for this can be seen in Figure 2.3. In Figure 2.3 the pulse, in the time domain, is reflected off a grating, dispersing the frequencies contained in the

pulse onto a cylindrical mirror, which collimates the beam and reflects the wavelengths of light onto a flat mirror. The flat mirror reflects the wavelengths though the aperture of the AOM and through the germanium crystal. The beam is reflected out of the AOM and using a second flat mirror, directed to second cylindrical mirror. The second cylindrical mirror focusses the beam onto a second grating. The second grating Fourier transforms the wavelengths of light back into the time domain, generating the necessary pulse pair.

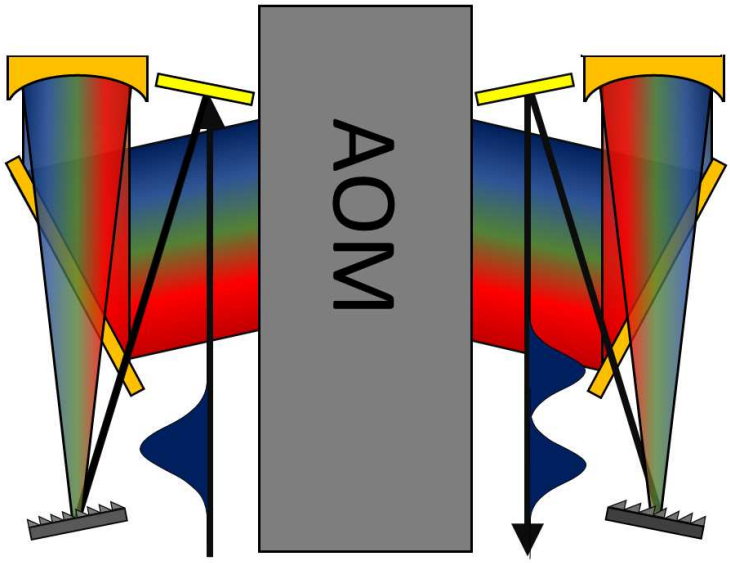

Figure 2.3 Beam geometry of the pulse shaper used to generate the pump pulses. The mid-IR pulse is frequency-resolved across a germanium crystal using a grating and a cylindrical mirror to collimate the beam. The output pulse pair is focused onto a second grating to Fourier transfer the pulses into the time domain.

2.4.2 Mask Generation

An acoustic wave is used as the mask that passes through the AOM. The mask acts as a transmission grating, refracting the different wavelengths of light. Depending on the properties of the mask, the amplitude and phase of the wavelengths in the ultrafast pulse can be modulated. In the following section the principles of mask generation, the characteristics of the mask that produce pulse pairs, manipulation of the pulse pairs, and important pitfalls of shaping will be discussed.

Because the mask acts as a transmission grating, the diffraction angle of the optical frequencies is expressed in Equation 2.1.

$$sin(\theta) = \frac{\lambda \nu_{RF}}{2\upsilon_{ac}} \tag{2.1}$$

where ν_{RF} is the frequency of the acoustic wave, υ_{ac} is the speed of sound though the germanium crystal, λ is the center frequency of the optical pulse, and θ is the angle of diffraction for the center frequency of the optical pulse. For our germanium-based pulse shapers, the center frequency of the acoustic wave is 75 MHz and the speed of sound in the germanium crystal is approximately 5,400 m/s.

Equation 2.1 shows that the different wavelengths are diffracted by the mask the angle will be different with each wavelength. With ultrafast pulses, the bandwidth can be significant, in some cases spanning a few thousand nanometers from base to base of the pulse. Consequently, the frequencies that make up the optical pulse will be diffracted at different angles causing a temporally chirped pulse.

Correcting this angular dispersion involves the use of a chirped mask through the AOM. The mask is chirped spatially through the germanium crystal. This results in the center wavelength of the optical pulse experiencing a mask at 75MHz, but shorter wavelengths will interact with a mask that has a frequency less than 75MHz, and longer wavelengths will interact will mask frequencies larger than 75MHz. In practice this is applied though group velocity dispersion (GVD) and third order dispersion (TOD) compensations.

Angular dispersion is not the only factor to generate pulse distortions in a pulse shaper. As the optical pulse passes through the germanium crystal in the AOM, it will pick up phase from the material. In an ultrafast pulse this will result in chromatic dispersion. Chromatic dispersion can be

expressed mathematically as the Taylor series expansion of the change in spectral phase per distance, *k* as shown in Equation 2.2.

$$k(\omega) = k_0 + \frac{\partial k}{\partial \omega}(\omega - \omega_0) + \frac{1}{2!}\frac{\partial^2 k}{\partial^2 \omega}(\omega - \omega_0)^2 + \frac{1}{3!}\frac{\partial^3 k}{\partial^3 \omega}(\omega - \omega_0)^3 \qquad (2.2)$$

where *k* is the change in spectral phase per unit of distance, ω is the angular frequency and ω_0 is the center frequency. The second order coefficient in this expression is GVD, with units of fs^2/mm, and the third order coefficient is the TOD, with units of fs^3/mm. $k(\omega)$ is then multiplied by the thickness of the material. The germanium crystal in the AOM is 10 mm thick. Therefore, the mid-IR light used in these 2D IR experiments is stretched from 110 fs to 8 ps. An 8ps pulse is too long for these experiments, therefore it is necessary to manipulate the acoustic mask to compress the pulse.

To apply the masks to the germanium crystal, an arbitrary waveform generator (AWG) will send the waveform to a radio frequency (RF) amplifier. The output of the RF amplifier drives a piezoelectric crystal inside of the AOM. The piezoelectric crystal sends a compression wave through the germanium crystal, generating the physical mask that interacts with the optical waves. The mask is made of discrete points referred to as samples. A Signatec PXDAC4800 arbitrary waveform generator (AWG) card is used to generate the mask. The Signatec PXDAC4800 has a 1200 GHz internal clock meaning that it can generate 1.2×10^9 samples per second. Masks can be made of different lengths of samples, where the more samples that are used, the longer the mask will be. Conventionally, the maximum number of samples is 12,000. If this sample number is used, then it would take 10 μs for the mask to clear the germanium crystal. Using this value and based on the speed of sound in germanium, 5400 m/s, the total length of the mask would be 54 mm long.

Overcoming the second order dispersion that is placed on the pulse can be done using material compensation. The germanium puts positive dispersion on the pulse, therefore, placing a

piece of material in the beam line with negative dispersion can act to cancel out the effects of the germanium. For example, calcium fluoride has approximately 1200 fs^2/mm of dispersion at 6 μm. Therefore, placing approximately half the material length that is in the germanium will correct for the material dispersion.

2.4.3 Rotating Frame and Phase Cycling

Pulse shaping allows for faster data collection and better signal-to-noise by using phase cycling and rotating frame. There are three phase cycling schemes commonly used in 2D-IR: two, four, and eight frame phase cycling. All of them rely on the fact that the emitted 2D-IR signal as a function of the phase of the pulse, but other signals such as noise or transient absorption are not. An example of four frame phase cycling is shown in Figures 2.4. Figure 2.4(a) through Figure 2.4(d) shows the free induction decay (FID) for each frame. In this case, there is a delta π phase shift in the signal between frame one and two, as well as a delta π phase shift between frame three and four. The next step in four frame phase cycling is to subtract frame one from frame two, subtract frame three from frame four, and finally add the results of the two subtractions together. This is shown in Figure 2.4e and f. The result is a signal field with drastically less noise and a higher signal intensity.

One of the other benefits of pulse shaping is using rotating frame to reduce acquisition time. Rotating frame does this by increasing the Nyquist frequency of the signal allowing for larger pump steps and therefore faster acquisition times.

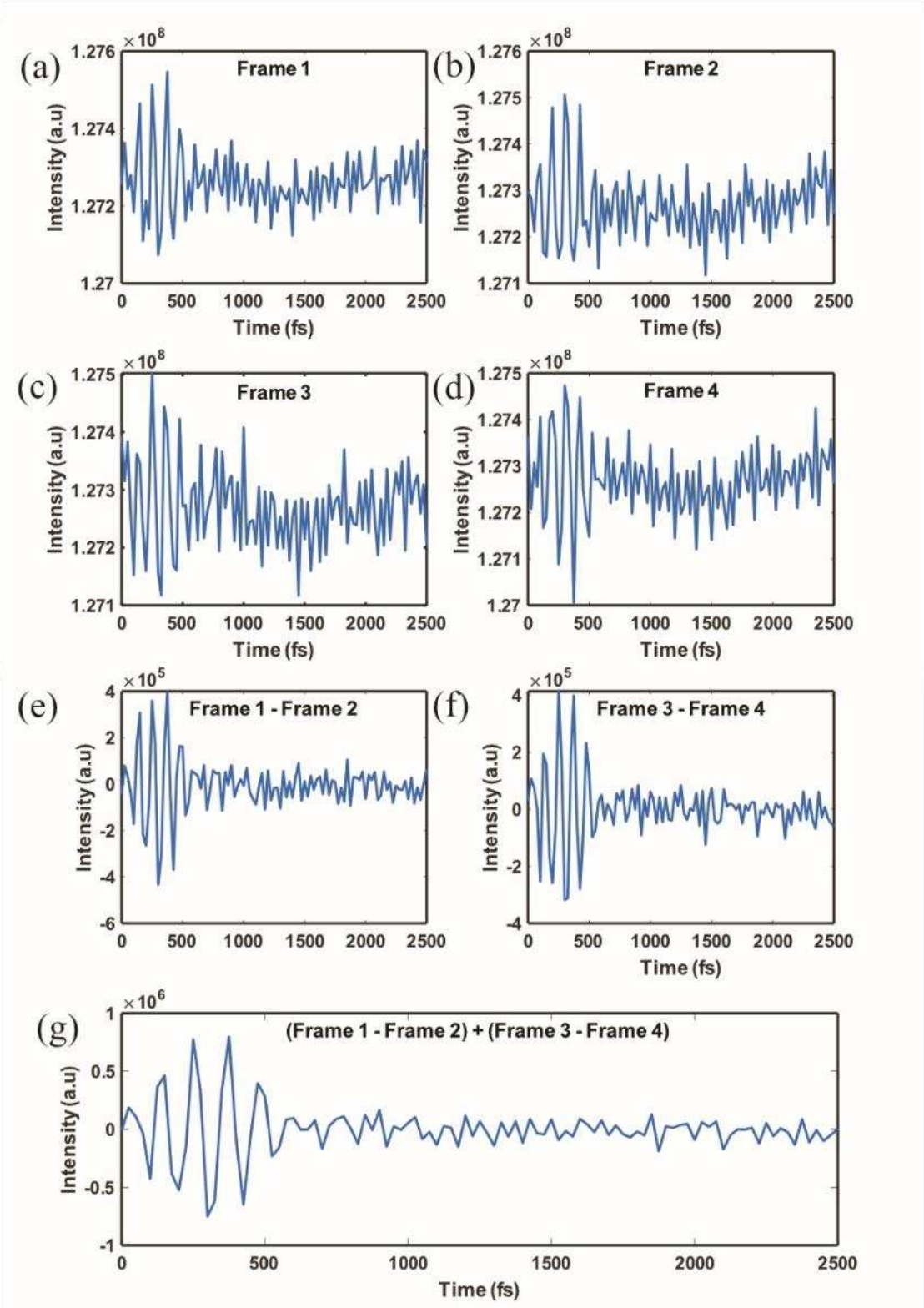

Figure 2.4. Plots (a) through (d) shows free induction decay of time traces of each frame for a given pixel of the dipeptide VF. Subtracting plot (a) from (b) generates plot (e) and subtracting plot (c) from (d) generates plot (f). The final signal that is generated is shown in (g). Plot (g) is the result of adding plot (e) and (f) together.

2.5 Understanding 2D IR Spectra

Multidimensional spectroscopy provides additional information on the structure and dynamics of chemical systems through the addition of frequency and temporal information. This is done by using multiple ultrafast mid-IR pulses to excite an ensemble average of a molecular sample into the first and second vibrational level. In addition, by controlling the time intervals between pump and probe pulses the dynamics of chemical systems can be studied. This section will look at the energy pathways the chemical system goes through as well as information that can be learned from 2D IR spectra.

2.5.1 Energy pathways in an optically pumped system

One of the key observables in a 2D IR spectra is a negative and positive going peak pair. This peak pair results from exiting an ensemble average of the molecules into both the first and second vibrational energy levels. Because these vibrations are anharmonic, the energy spacing between the ground state and the first excited state will be different from the energy spacing between the first excited state and the second. Conventionally, the 0 to 1 transitions are represented as negative going and the 2 to 1 transitions are shown as positive going. This anharmonicity causes the frequency shift between the positive and negative going features.

Double sided Feynman diagrams can be a useful way of representing energy level pathways in multidimensional experiments. Each row of the Feynman diagram corresponds to the density operator ρ where $\rho = \sum_{n,m} c_n c_m^* |n\rangle\langle m|$. The Feynman diagram therefore tracks how $|n\rangle\langle m|$ change with each light matter interaction. Each light matter interaction is represented as an arrow pointing to either the bra or the ket. When the arrow is pointing at the diagram the system is moving up in energy. When the arrow is pointing away the system is moving down in energy. The dashed arrow represents the emitted signal field. For more information in this, see references 1 through 4.

The Feynman diagrams for three of the fundamental energy pathways that are observed in 2D IR can be seen in Figure 2.6.

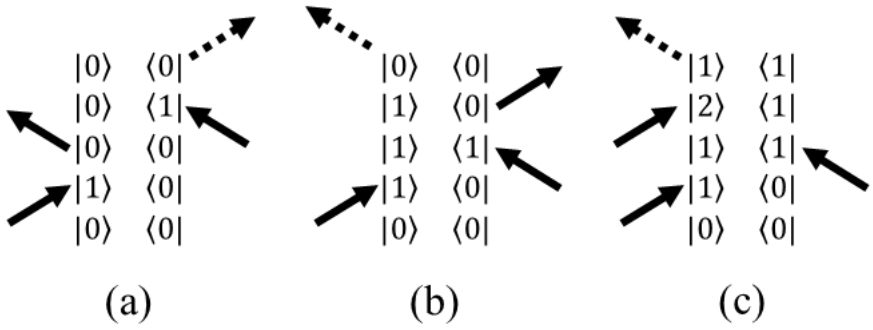

Figure 2.5 Feynman diagrams of bleach (a), stimulated emission (b), and excited state absorption (c).

In Figure 2.6a, the first pump pulse excites the sample creating a coherence between the ground and the first excited state; the system goes from a population, |0> <0|, to a coherence |1> <0|. Then the next pump pulse excites the sample and drives the coherence into the ground state, |1> <0| to |0> <0|. Finally, the probe pulse interacts with the sample generating the coherence between the ground and first excited state, |1> <0|. Finally, a signal field is emitted and the system returns to |0> <0|. Similar processes can be seen in Figure 2.6b and Figure 2.6c [1]. These processes can be related back to Figure 1.1 where Figure 2.5a and b contribute to the blue peak and Figure 2.5c produces the red peak.

When vibrational modes are coupled together, different energy transfer mechanisms can occur during a 2D IR experiment. These include quantum beating, coherence transfer, and population transfer. To understand when these different kinds of energy transfer processes occur the time intervals between the different pulses needs to be considered. The time between the two pump pulses, τ, can be referred to as the coherence time. It's during this time interval that the established coherence between the ground state and some excited state can be transferred due to some event in solution. The other time interval is T_w, referred to as the waiting time or the

population time. During this time interval, a population that was established by the two pump pulses can be transferred to a new population. Finally, quantum beating comes from when both modes are pumped, mode a with the first pump pulse and mode b with the second pump pulse. These modes will then beat on one another causing peak fluctuations and line shape deviations. Coherence transfer, population transfer, and quantum beating can be represented through Feynman diagrams as seen in Figure 2.7a, Figure 2.7b, and Figure 2.7c respectively. In Figure 2.7 the dashed line represents the event that occurs that forces the coherence transfer, population transfer, or quantum beating.

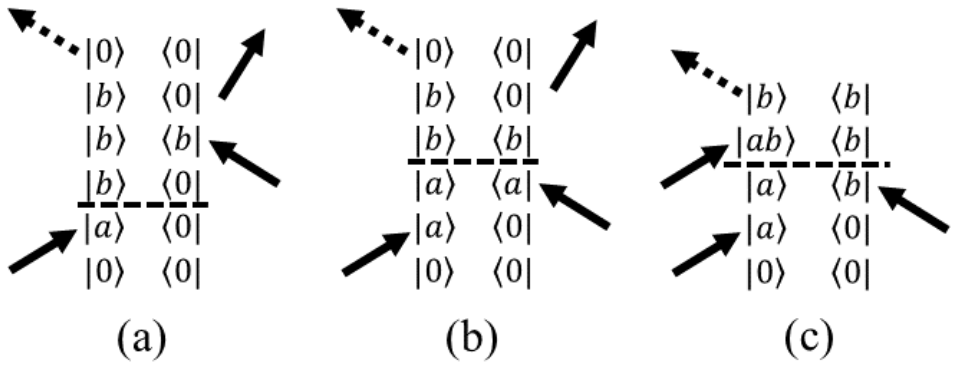

Figure 2.6 Feynman diagrams of coherence transfer (a), population transfer (b), and quantum beating (c).

2.5.2 Line Shape

The 2D IR line shape will report on the solvent environment the vibrational oscillators are in. The first step in understanding vibrational solvent environment is to introduce homogeneous and inhomogeneous frequency distributions. In an inhomogeneous solvent environment, the normal vibrational mode experiences many local environments, resulting in a distribution of vibrational frequencies. This is observed as one broad spectral feature that contains all the different vibrational modes. In contrast, a vibrational mode in a homogeneous solvent environment will

experience only one solvent environment ergo, one frequency. The spectral response will therefore be a narrow spectral feature

The homogeneous and inhomogeneous frequency distribution in a 2D IR spectrum manifests itself as the degree of ellipticity in the peak pair. An example of this can be seen in Figure 2.7. In Figure 2.7a, violanthrone-79 is in chloroform and in Figure 2.7b, violanthrone-79 is in tetrahydrofuran. The greater degree of ellipticity of violanthrone-79 in chloroform suggests that

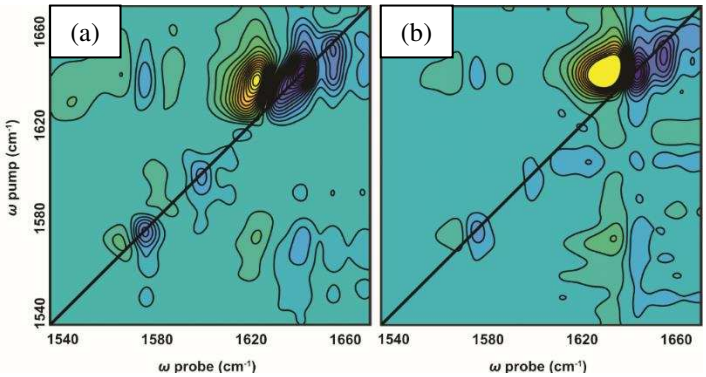

Figure 2.7 2D-IR spectra of violanthrone-79 in an inhomogeneous solvent environment (a) and a homogeneous one (b). The observed line shape of the 2D-IR spectral features are a function of solvent interaction.

the sample is more inhomogeneous, ergo there are more environments that the vibrational probed exists in. This is in contrast to violanthrone-79 in tetrahydrofuran, where the peak has little to no ellipticity. Round peaks suggest the violanthrone-79 aggregates in tetrahydrofuran is more homogeneous environment.

Conducting experiments that examine the rate of the peak transitioning from elliptical to round, characterizes the solvent movement in the sample, as well as how quickly the reporter molecule can sample the different configurations. These experiments can then be related back to the frequency-frequency correlation function (FFCF), a function that reports on the frequency memory of the system.

2.5.3 Chemical Exchange and Exchange Rate

Molecular systems can exist in equilibrium between different conformation states or hydrogen bonding environments. These different environments can shift the frequency of the vibrational normal mode, resulting in two observed peak pairs in the 2D IR spectrum. The resulting spectrum of this is shown in Figure 2.8a, where the two peaks are labeled α and β. Figure 2.8a is collected with a T_W time of 0 ps. As this waiting time is extended, the chemical environment can evolve. Consider the example of hydrogen bond making and breaking. A hydrogen bonded vibrational mode will have a lower frequency than a non-hydrogen bonded vibrational mode. Using Figure 2.8 as an example, this would imply the α peak is a hydrogen bonded environment and β is a non-hydrogen bonded environment. When the T_W time is increased, the vibrational mode may be pumped in a hydrogen bonded environment and probed in a non-hydrogen bonded environment. This would result in the growing in of a cross peak, Figure 2.8b. When this waiting time is extended even further, the intensity of cross peak will continue to increase, Figure 2.8c.

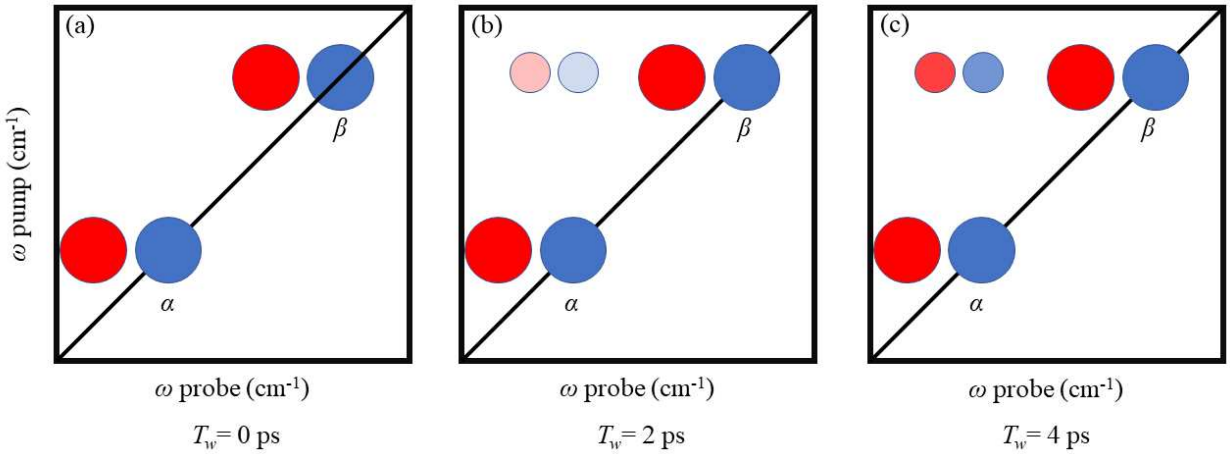

Figure 2.8 Cartoon example of a chemical exchange 2D IR experiment. In this example there are two vibrational modes, α and β, that are being probe. Figure 2.8a is at early time where no cross peak is observed between the two modes. However, as the T_w time is extended the intensity of the cross peak grows in. This is shown in Figures 2.8b and c where the cross peak becomes more intense with time.

A 2D IR chemical exchange experiment collects the necessary data to track and quantify this exchange in chemical environments. Tracking the change in the intensity of the cross peaks and the diagonal peaks results in an exponential decay or growth. By fitting this data to an exponential function and extracting the rate constants out, the exchange rate from one stat to the other can be determined. This is shown in equation 2.3 as $k_{\alpha\beta}$ and $k_{\beta\alpha}$. If we assume the rate from α to β is the same as β to α then we can express the exchange as $k_{\alpha\beta}^2$.

$$k_{CP} \cong \frac{k_{\propto} + k_{\beta}}{2} - \sqrt{\left(\frac{k_{\propto} - k_{\beta}}{2}\right)^2 + k_{\alpha\beta}\, k_{\beta\alpha}} \qquad (2.3)$$

2.6 Linear Infrared Absorption Spectroscopy and Microscopy

The linear spectra presented in this thesis were the result of averaging 64 spectra with 1 cm^{-1} resolution and collected on a Bruker Vertex 70 absorption spectrometer. The sample compartment was purged with dry air for 5 minutes before each measurement. Each data set had an atmospheric water spectrum subtracted from it using the OPUS software package. A Matlab script is then used to subtract a solvent background and fit spectral features to Gaussian or Lorentzian functions.

Second derivative spectra where generated using the OPUS software package. The OPUS software package uses a Savitzky-Golay filter to smooth the original data set. A second derivative spectrum shows the underlying features by exposing deviations in the FTIR spectrum. Therefore, every negative-going peak position corresponds with a vibrational mode.

The Hyperion 3000 is a focal plane array microscope (FPA) that allows for spatially resolved FTIR spectra across a chemical sample. This is particularly useful when examining the self-assembled structures of the different dipeptide molecules presented here. The Hyperion 3000 uses a 15x objective lens to image the sample onto a 64x64 element focal plane array, FPA. This

results in collecting an FTIR spectrum at each pixel of the FPA. A brightfield image was taken with every FTIR providing correlation with an FTIR with a location on the sample.

2.7 Sample Preparation

The work presented here examines a variety of different chemical systems. Therefore, several different procedures are required to prepare samples for spectroscopic investigation. The follow section describes the sample preparation for all of the experiments conducted in this thesis.

2.7.1 Violanthrone-79

Violanthrone-79 (V-79) was purchased from Ark Pharm without further purification. For 2D IR experiments 10 mM samples of V-79 were prepared in both $HCCl_3$ and THF. Each sample was sonicated for approximately 5 minutes or until the sample had fully dissolved.

2.7.2 Dipeptide Samples

Five different dipeptides where examined in this work; valine-phenylalanine, phenylalanine-valine, isoleucine-phenylalanine, phenylalanine-isoleucine, and phenylalanine-phenylalanine. Samples where purchased from Bachem without further purification. Each dipeptide had different sample handling procedures depending on the propensity for self-assembly.

Phenylalanine-phenylalanine (FF) nanotubes were synthesized dissolving FF into D_2O for a final concentration of 7.4 mM. Using a VWR mini block heater set to 100°C the FF sample is heated for approximately 10 minutes. Then the sample is sonicated for 5 minutes. This procedure is repeated until the sample is dissolved. As soon as the sample approaches room temperature nanotubes will start forming. Therefore, it is necessary to pipet the sample onto a CaF_2 plate while the sample was still in the heat block. CaF_2 plates with FF on them are placed in a petri dish and allow to set until the D_2O has evaporated off.

Both isoleucine-phenylalanine (IF) and phenylalanine-isoleucine (FI) form less ordered structures when compared to FF, and are therefore easier to get into solution. For these systems, a 10 mM solution is made by dissolving the powered dipeptide into D_2O or dimethyl sulfoxide (DMSO). A VWR mini heat block is also used to force the dipeptide into solution. For these samples the heat block only needs to be set to 80°C for approximately 10 minutes and then sonicated. This procedure is repeated until the dipeptide goes into solution. IF and FI samples also need to be deposited onto the CaF_2 while the sample is still warm. CaF_2 plates are placed in a petri dish and allowed to sit until the D_2O has fully evaporated.

Valine-phenylalanine and phenylalanine-valine where prepared in D_2O with a final concentration of 150 mM. Samples were prepared in snap-capped vials and heated in a mini-block heater set to 50°C for 3 to 5 minutes and then sonicated for another 10 minutes. The vials were then sealed with paraffin wax and placed in a -18°C freezer when not in use.

2.8 Introduction to Phenylalanine Self-Assembly

Many material scientists have turned their attention to self-assembled peptides to make novel materials for tissue engineering,[5,6] drug delivery,[7] antibacterial applications,[8] and nanofabrication.[9] Engineered proteins range in a variety of sizes from two amino acids to very long chains with a variety of amino acid combinations.[10] Functionalizing these peptides will produce changes in the self-assembled structure allowing for tailor-made aggregates for a variety of applications.[7] One of the most popular building blocks in peptide self-assembly is phenylalanine. Phenylalanine, shown in Figure 2.9, is only one of four essential amino acids with an aromatic

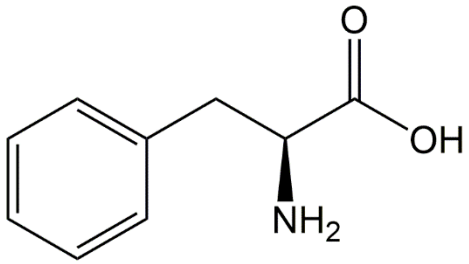

Figure 2.9 Chemical structure of the amino acid Phenylalanine. Phenylalanine is one of the building blocks in self-assembled structures.

side chain, and is in relatively low abundance in protein structures in the human body[11]. However, phenylalanine is responsible for the human body's generation of amyloid plaque, a structure that contributes to diseases such as Alzheimer's[8,12]. Material scientists have used nature's phenylalanine-based nanostructures as inspiration for their own work with great successes.[13] Even with all of phenylalanine's contributions to advancing materials chemistry, the underling physics that drive its self-assembly is unclear.[12] By gaining a deeper understanding of the physical driving forces of phenylalanine nanostructures, chemists can design better peptide-based building blocks in an ever demanding field of research.

2.8.1 Diphenylalanine Self-Assembly

Diphenylalanine, composed of two phenylalanine amino acids as shown in Figure 2.10, is instrumental in dipeptide self-assembly. Diphenylalanine quickly and easily forms highly ordered nanotubes in water. Because of its self-assemble properties, there is a large body of research focused on its application to any material science problem.

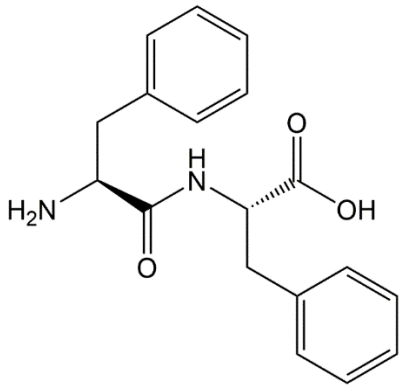

Figure 2.10 Chemical structure of the dipeptide diphenylalanine that forms nanotubes in water.

Interestingly, diphenylalanine's self-assembled network is disrupted by altering the solvent[14], the pH, or the salinity of the solution.[15] Therefore, if either the structure or chemical dynamics of diphenylalanine can be characterized in these various environmental conditions, a better model of the self-assembled system will be developed. Presented here are some of the first steps towards that endeavor. By examining the FTIR microscopy data of diphenylalanine nanotubes, a better understanding of the distribution of different structures is gained as well the role water plays in self-assembly.

2.8.2 Diphenylalanine Experimental Results

Figure 2.11 shows one of the diphenylalanine nanotubes that form in D_2O. A bright field image of the nanotube is shown in Figure 2.11(b), with an approximate width of 20 microns. In Figure 2.11b there are 3 circles indicating where FTIR spectra are being extracted from. These FTIR spectra are shown in Figure 2.11c. The region in blue is the amide I peak of the dipeptide. This peak is being integrated over and its concentration corresponds to the heat map Figure 2.11a.

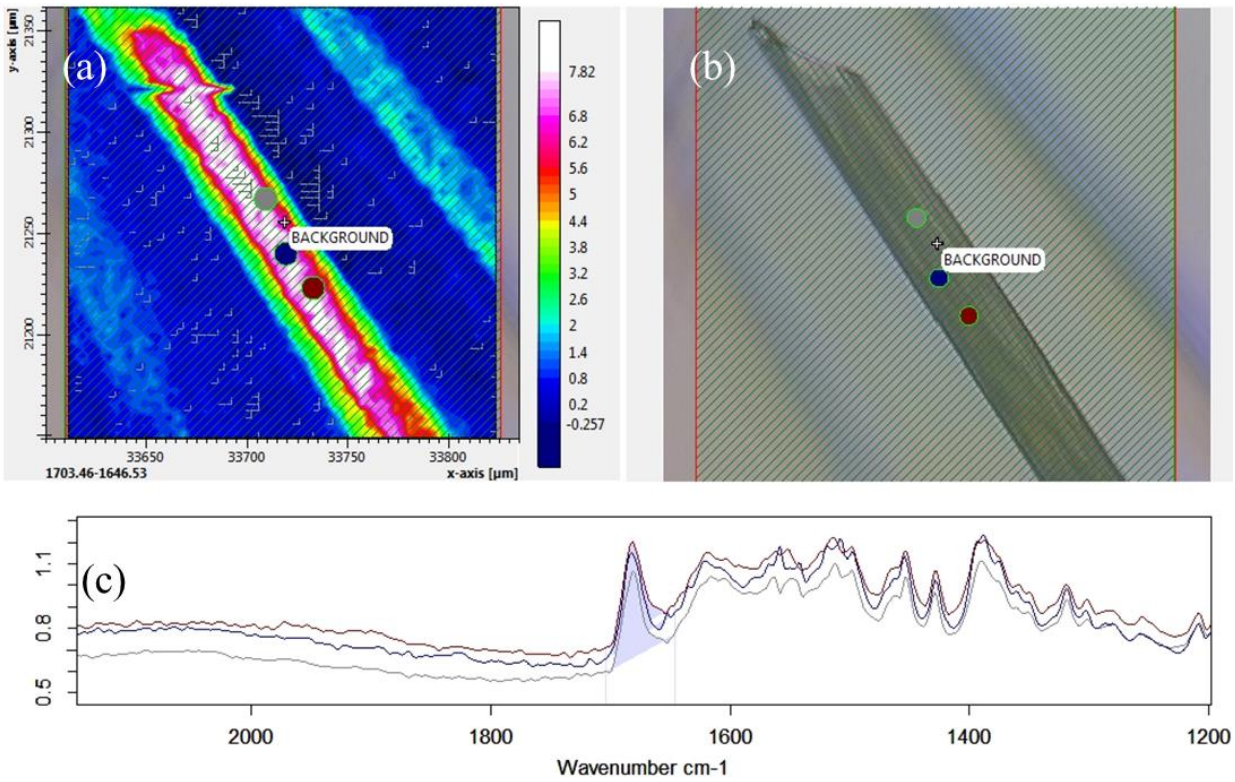

Figure 2.11 FTIR microscopy data of a Phe-Phe nanotube formed in D_2O. (b) The bright field image of the nanotube with the three dots on the image, colored grey, blue, and red, corresponding to locations of extracted FTIR spectra shown in (c). The blue-grey area in (c) corresponds to the amide I region of the peptide bond. This region is integrated over such that the intensity of that transition corresponds to the color map shown in (a).

Figure 2.12 is the same Phe-Phe nanotube shown in Figure 3.3, however, instead of integrating over the amide I stretch, Figure 2.12 integrates over the D-O stretch of D_2O. This integration shows D2O is trapped within the nanotubes as it forms.

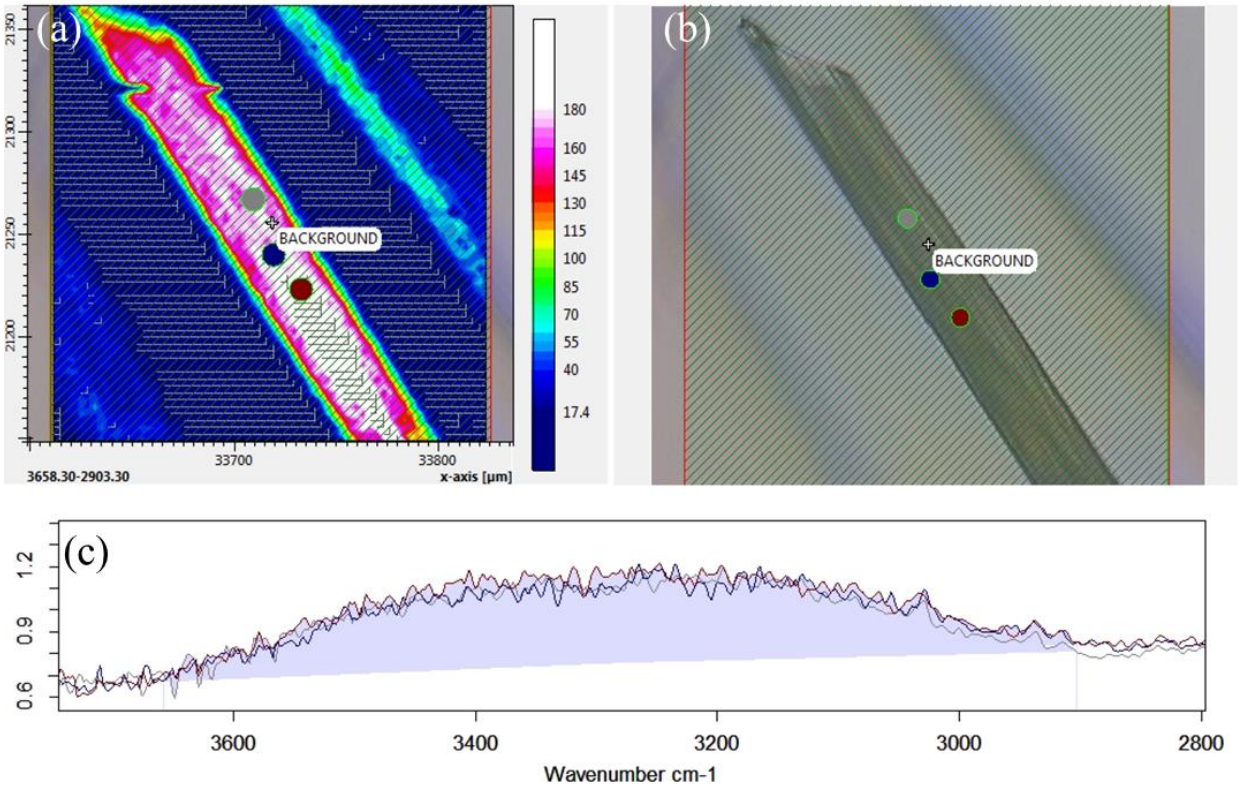

Figure 2.12 FTIR microscopy data of Phe-Phe formed in D_2O. (b) The bright field image of the nanotube with the three dots on the image, colored grey, blue, and red, correspond to locations of extracted FTIR spectra shown in (c). The blue-grey area in (c) corresponds to the D-O stretch of heavy water that is trapped inside of the nanotube. This region is being integrated over, and with the intensity of that transition corresponding to the color map shown in (a).

Figures 2.13 and 2.14 show a different nanotube then the one shown in Figures 2.11 and 2.12. Presented here is a nanotube where heavy water is trapped in a portion of it and in the other, there is no D_2O is trapped. In the region where there is no heavy water present, the amide I peak is stretched from approximately 1675 cm^{-1} down to 1625 cm^{-1}, as seen in Figure 2.13c. This large distribution of frequencies suggests two things: one, that the dipeptide exists in a variety of different chemical environments, and two, that the secondary structure of the aggregated dipeptide varies throughout the structure.

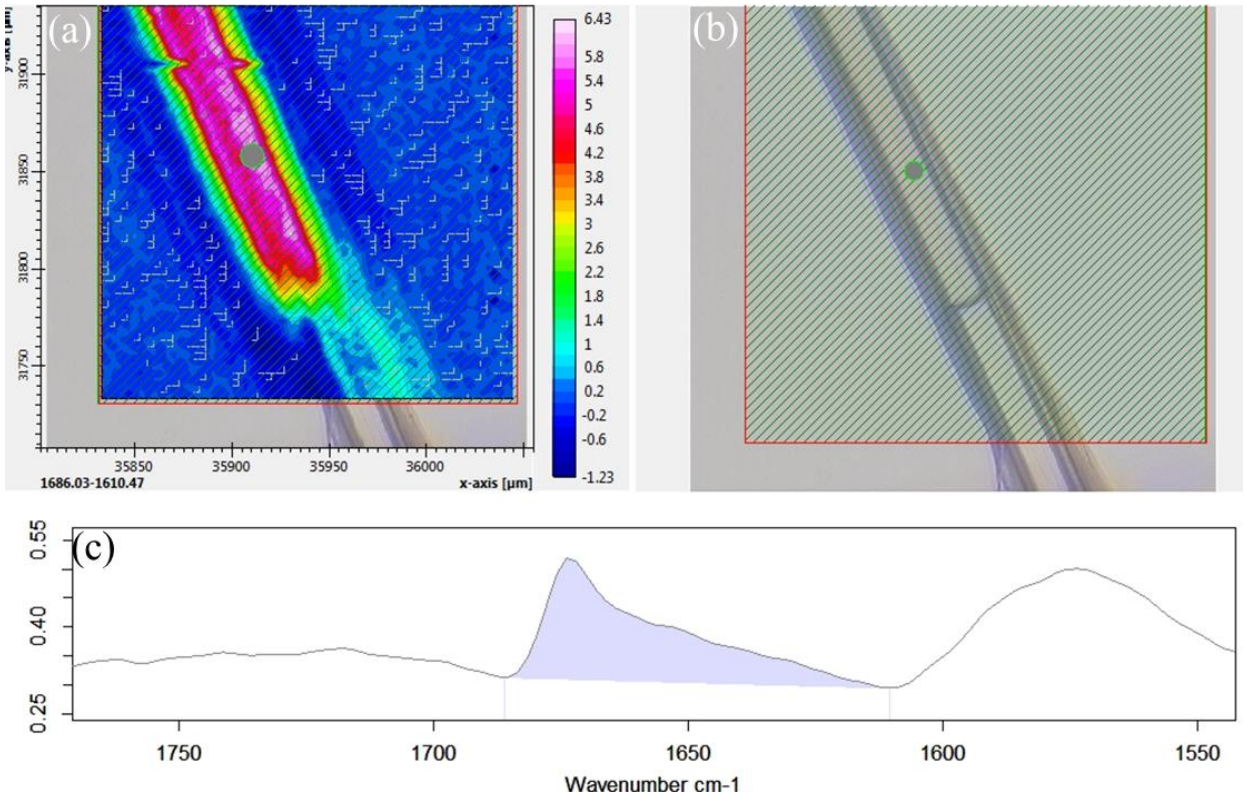

Figure 2.13 FTIR microscopy data of a Phe-Phe formed in D_2O. (b)The bright field image of the nanotube with the green dot corresponding to the location of the extracted FTIR spectrum shown in (c). In this image, spectra are being extracted from a region of the nanotube where D_2O is not trapped inside of the tube. The blue-grey area in (c) corresponds to the amide I region of the peptide bond. This region is integrated over, and with the intensity, of the transition corresponding to the color map shown in (a).

Figure 2.14 is of the same nanotube, but with a spectrum extracted in a region where D_2O is trapped within the nanotube, as shown by the green dot in Figure 3.6b. In this spectrum, the amide I is much narrower, which suggests that the self-assembled structure is much more uniform when D_2O is trapped in the tube.

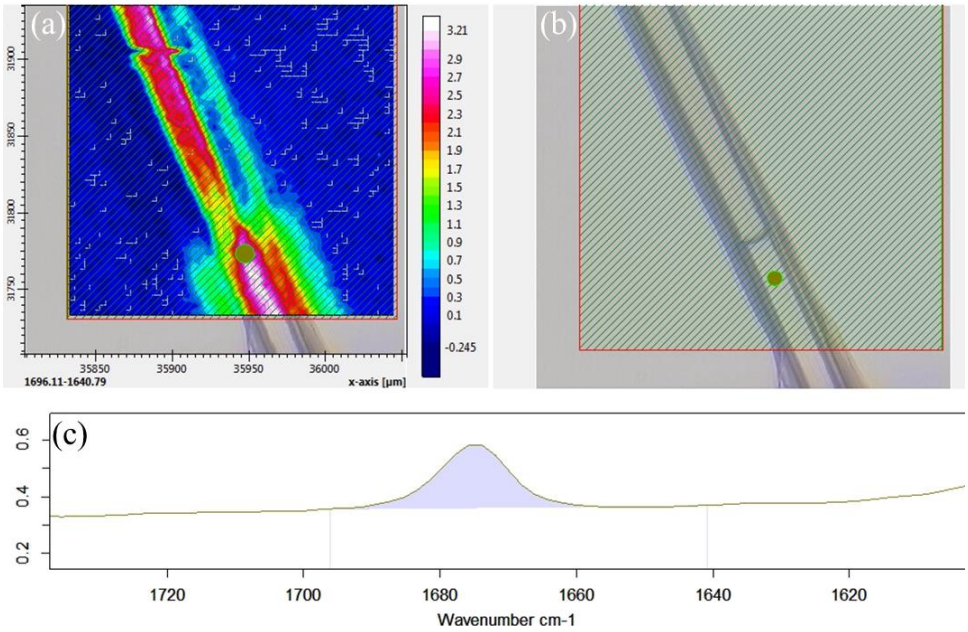

Figure 2.14 FTIR microscopy data of a Phe-Phe formed in D_2O. (b) The bright field image of the nanotube with the green dot corresponding to the location of the extracted FTIR spectrum shown in (c). In this image, spectra are being extracted from a region of the nanotube where D_2O is trapped inside of the tube. The blue-grey area in (c) corresponds to the amide I region of the peptide bond. This region is integrated over, and with the intensity, of the transition corresponding to the color map shown in (a).

2.8.4 Diphenylalanine Derivatives: Isoleucine-Phenylalanine

To develop a model of diphenylalanine's molecular properties that drive the formation of the highly ordered structures, different diphenylalanine derivatives were considered. Isoleucine-phenylalanine, shown in Figure 2.15a, forms disordered structures, and valine- phenylalanine, Figure 2.15b, does not self-assemble. When comparing these two dipeptides, the only difference is the presence of an additional methyl in isoleucine. Identifying the molecular properties of these two dipeptides will enlighten the investigation into diphenylalanine's properties.

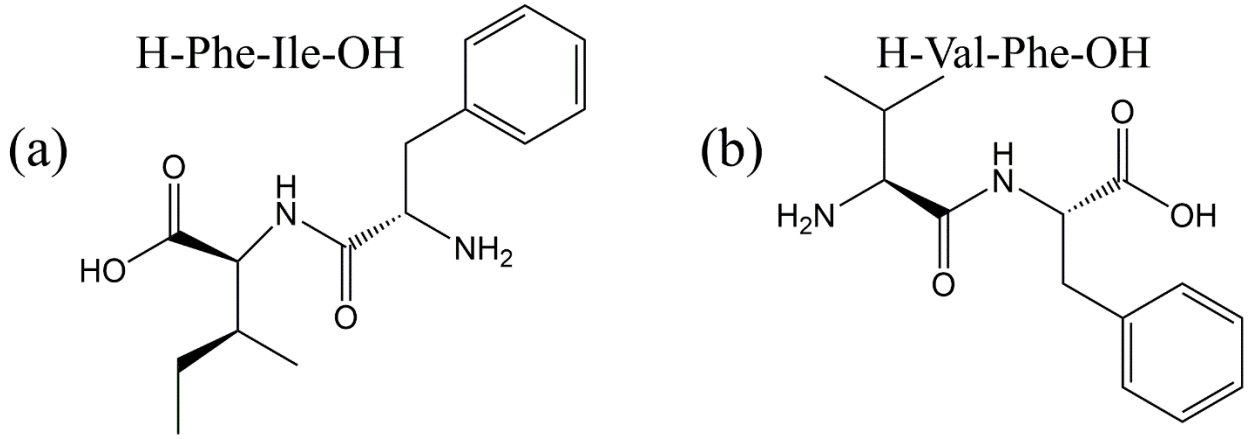

Figure 2.15 Chemical structures of Phe derivatives Phe-Ile (a) and Val-Phe (b). Phe-Ile will form non-ordered structures in water, while Val-Phe does not self-assemble.

This section and in Apendix II, the results of isoleucine-based dipeptides will be presented. Chapter 3 will present an in-depth look at valine-based phenylalanine dipeptides. At the beginning of this investigation a very import question arises: Does the primary sequence of the dipeptide affect the observed self-assembled structure? Shown in Figure 2.16 are two different isomers of the Isoleucine phenylalanine derivatives, Ile-Phe and Phe-Ile. To answer this question, we use microscope images coupled with FTIR microscopy to study the different dipeptides.

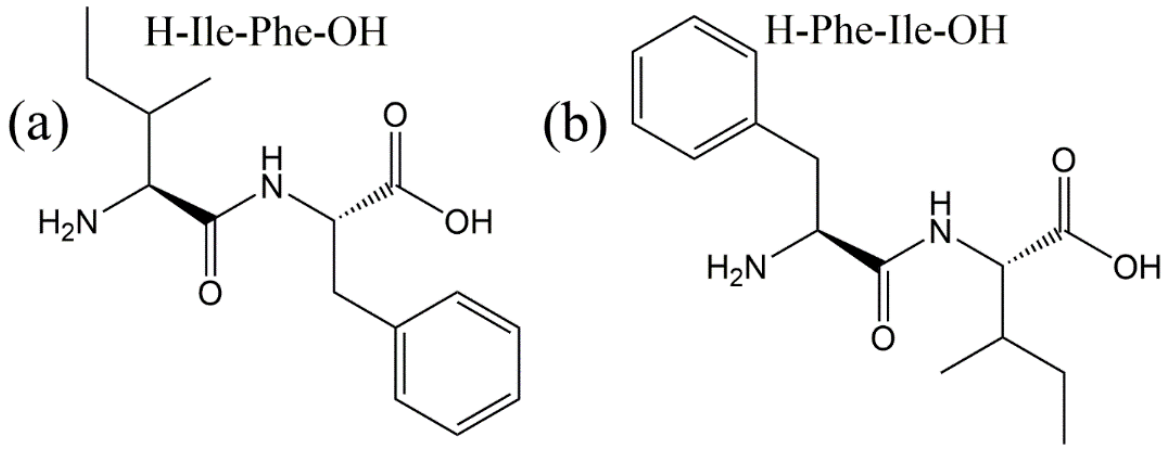

Figure 2.16 The two primary structures of Phe and Ile based dipeptides, Ile-Phe, (a), and Phe-Ile, (b).

2.8.5 Isoleucine-Phenylalanine and Phenylalanine-Isoleucine Experimental Results

The effect of solvent on the self-assembled systems was also examined by comparing structures formed in D_2O to aggregates formed in dimethyl sulfoxide (DMSO). Figure 2.17 shows bright field images of the different structures formed from the dipeptides IF and FI in the solvents D_2O and water.

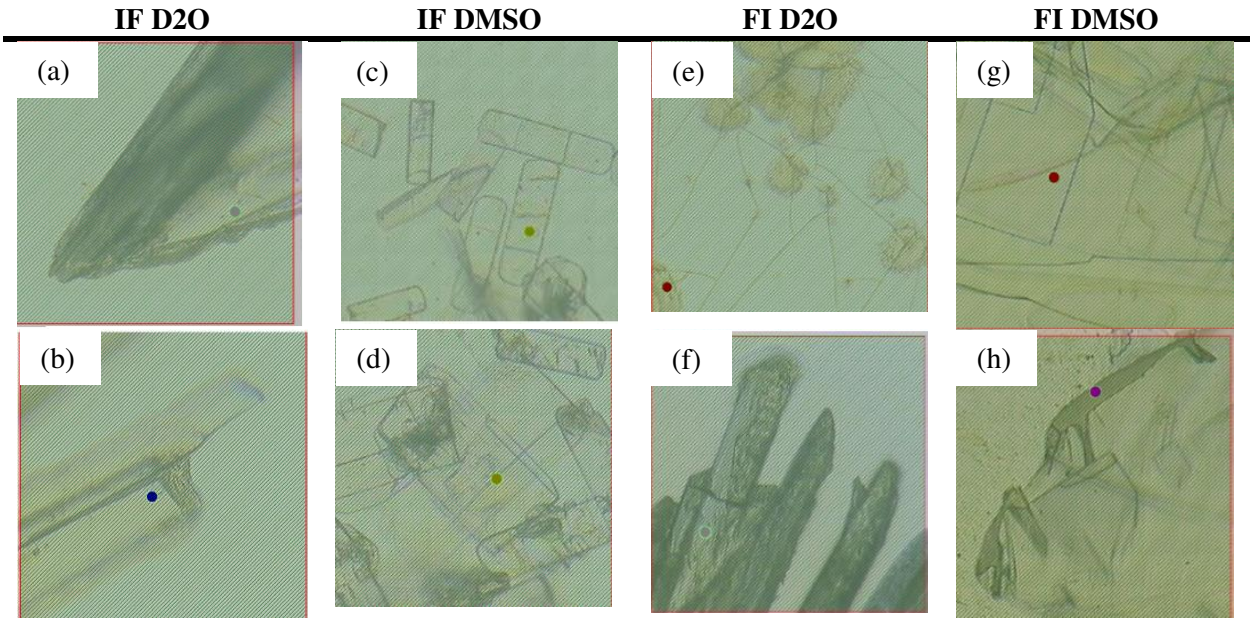

Figure 2.17 Bright field images of the different structures 75mM IF and FI can form. Figures (a) and (b) are of IF in D_2, Figures (c) and (d) are of IF in DMSO, Figure (e) and (f) are of FI in D_2O and Figures (g) and (h) are of FI in DMSO.

References

(1) Hamm, P.; Zanni, M. T. *Concepts and Methods of 2D Infrared Spectrscopy*, First.; Cambridge Univesrity Press: Cambridge, New York, 2011.

(2) Hochstrasser, R. M. Two-Dimensional IR-Spectroscopy: Polarization Anisotropy E€ ects. *Chemical Physics* **2001**, 12.

(3) Marroux, H. J. B.; Orr-Ewing, A. J. Distinguishing Population and Coherence Transfer Pathways in a Metal Dicarbonyl Complex Using Pulse-Shaped Two-Dimensional Infrared Spectroscopy. *J. Phys. Chem. B* **2016**, *120* (17), 4125–4130. https://doi.org/10.1021/acs.jpcb.6b02979.

(4) Hamm, P.; Lim, M.; Hochstrasser, R. M. Structure of the Amide I Band of Peptides Measured by Femtosecond Nonlinear-Infrared Spectroscopy. *The Journal of Physical Chemistry B* **1998**, *102* (31), 6123–6138. https://doi.org/10.1021/jp9813286.

(5) Fichman, G.; Gazit, E. Self-Assembly of Short Peptides to Form Hydrogels: Design of Building Blocks, Physical Properties and Technological Applications. *Acta Biomaterialia* **2014**, *10* (4), 1671–1682. https://doi.org/10.1016/j.actbio.2013.08.013.

(6) Ryan, D. M.; Nilsson, B. L. Self-Assembled Amino Acids and Dipeptides as Noncovalent Hydrogels for Tissue Engineering. *Polym. Chem.* **2012**, *3* (1), 18–33. https://doi.org/10.1039/C1PY00335F.

(7) Yan, X.; Zhu, P.; Li, J. Self-Assembly and Application of Diphenylalanine-Based Nanostructures. *Chem. Soc. Rev.* **2010**, *39* (6), 1877. https://doi.org/10.1039/b915765b.

(8) Schnaider, L.; Brahmachari, S.; Schmidt, N. W.; Mensa, B.; Shaham-Niv, S.; Bychenko, D.; Adler-Abramovich, L.; Shimon, L. J. W.; Kolusheva, S.; DeGrado, W. F.; et al. Self-

Assembling Dipeptide Antibacterial Nanostructures with Membrane Disrupting Activity. *Nat Commun* **2017**, *8* (1), 1365. https://doi.org/10.1038/s41467-017-01447-x.

(9) Reches, M. Casting Metal Nanowires Within Discrete Self-Assembled Peptide Nanotubes. *Science* **2003**, *300* (5619), 625–627. https://doi.org/10.1126/science.1082387.

(10) Paradís-Bas, M.; Tulla-Puche, J.; Zompra, A. A.; Albericio, F. RADA-16: A Tough Peptide – Strategies for Synthesis and Purification. *Eur. J. Org. Chem.* **2013**, *2013* (26), 5871–5878. https://doi.org/10.1002/ejoc.201300612.

(11) Non-Darwinian Evolution. 12.

(12) de Groot, N. S.; Parella, T.; Aviles, F. X.; Vendrell, J.; Ventura, S. Ile-Phe Dipeptide Self-Assembly: Clues to Amyloid Formation. *Biophysical Journal* **2007**, *92* (5), 1732–1741. https://doi.org/10.1529/biophysj.106.096677.

(13) Guo, C.; Luo, Y.; Zhou, R.; Wei, G. Probing the Self-Assembly Mechanism of Diphenylalanine-Based Peptide Nanovesicles and Nanotubes. *ACS Nano* **2012**, *6* (5), 3907–3918. https://doi.org/10.1021/nn300015g.

(14) Wang, J.; Liu, K.; Yan, L.; Wang, A.; Bai, S.; Yan, X. Trace Solvent as a Predominant Factor To Tune Dipeptide Self-Assembly. *ACS Nano* **2016**, *10* (2), 2138–2143. https://doi.org/10.1021/acsnano.5b06567.

(15) Chen, L.; Morris, K.; Laybourn, A.; Elias, D.; Hicks, M. R.; Rodger, A.; Serpell, L.; Adams, D. J. Self-Assembly Mechanism for a Naphthalene−Dipeptide Leading to Hydrogelation. *Langmuir* **2010**, *26* (7), 5232–5242. https://doi.org/10.1021/la903694a.

Chapter 3

The Influence of Dipeptide's Primary Structure on Water's Solvation Shell

This work will be published in a manuscript in 2019. In the processes of designing experiments to study dipeptide self-assembly I discovered that changing the primary sequence of a dipeptide changes it spectroscopic properties. I designed an experiment to examine the differences in the solvation shell in conjugation with Professor Martin McCullagh's research group.

3.1 Introduction

Self-assembling biomimetic materials have garnered significant interest due to their appealing physical properties and ease of synthesis. Naturally occurring protein-based materials outperform current synthetic materials in properties such as strength-to-weight ratio[1] and combined hardness and flexibility[2–4]. Interesting physical properties have been demonstrated for self-assembling peptides as short as two amino acids.[5] Despite the relative simplicity of dipeptide self-assembly, the final goal of choosing a peptide sequence and synthesis to produce a desired macroscopic structure remains elusive. This is due, in part, to the still large number of factors affecting the assembly of these materials and a lack of understanding of the fundamental driving forces of self-assembly.

Solvent environment, molecular functionalization and primary sequence are factors that have a strong influence on the macroscopic properties of self-assembled peptide materials[6,7]. The examination of these self-assembled structures often begins in aqueous environments due to its propensity in biological systems. However, recent work has shown that self-assembly can be altered or mitigated by adding salts[8] or cosolvents[9] to change the self-assembled structure of a given peptide sequence. For example, diphenylalanine forms a distribution of structures depending on its chemical environment. Another parameters that is altered to influence the aggregation of biologically inspired compounds is

functionalization. Changing the functional groups of a protein will alter molecular driving force. For example, a common modification is the addition of One of the more common functionalizations is an FMOC cap[10] due to its use in peptide synthesis. The relatively large aromatic moiety significantly alters the intermolecular interactions of short peptides and thus alter the self-assembly behavior. This kind of synthesis has found utility in drug delivery systems.

In addition to solvent and functional groups, a peptide sequence has a large impact on assembled structure. Slight modifications of sequence can have a large effect on self-assembly but the driving forces behind these differences are poorly understood. This has been observed in short peptides[11] as well as longer peptides.[12] A computational approach has been used to study the self-assembly of the full sequence space of dipeptides[13] and tripeptides in wate[14]. The results demonstrated some important trends, namely hydrophobic residues contribute significantly to aggregation propensity and the reversing of a sequence had little effect on the resulting structure. Important exceptions to this rule include valine-phenylalanine (VF), phenylalanine-valine (FV), phenylalanine-tryptophan (FW), and tryptophan-phenylalanine (WV). This suggests that the one or more of residues V, F and W behave significantly different on the N- and C-termini.

Dipeptides are a well-studied example due to their simplicity and combinatorics accessibility. Additionally, diphenylalanine (FF) is a promising peptide-based biomaterial with proposed applications in drug delivery, antibiotics and piezoelectric materials. The self-assembly of FF has been well studied[15] with a recent computational study having investigated the driving forces of FF self-assembly in water across multiple scales.[16] Slight modifications to this the FF sequence cause significant changes to the assembled structure. This is most salient when one considers changing the N-terminal phenylalanine to an isoleucine. The IF dipeptide is found to assemble into more fibril like structures that exhibit reduced order as compared to their FF counterparts. Even more interestingly, the VF dipeptide is found to not assemble at all[17]. This sequence of peptides clearly exhibits interesting behavior and yet it is not clear why they behave this way.

Here we choose to study the sequence dependent behavior of VF and FV. As noted in a computational study by Frederix et al., flipping the sequence of a variety of different dipeptides resulted in

changes in their aggregation behavior.[13] We use a combined vibrational spectroscopy and computational modeling approach to investigate the solvation structure around these monomers. Linear infrared (IR) spectroscopy and two-dimensional infrared (2D IR) spectroscopy are used to probe the local solvation dynamics surrounding the VF and FV dipeptide structures. Linear IR and 2D IR spectroscopy techniques are ideally suited to reveal differences in solvation dynamics that are promoted by the dipeptide structural fluctuations. The amide I vibrations and the vibrational modes associated with the carboxylate group can be used to report on structures of the dipeptides and are sensitive to local solvation dynamics. In addition, 2D IR spectroscopy experiments allow the solvation dynamics and the structural fluctuations of the dipeptides to be investigated with subpicosecond time resolution. The combined structural sensitivity and high time resolution allow new insights into the way solvation dynamics may promote sequence dependent behaviors in the VF and FV dipeptides. Interestingly, the solvation dynamics and structure are significantly altered by the position of the phenylalanine residue. This behavior will alter the aggregation free energy of these peptides and thus the aggregation propensity.

3.2 Methods:

3.2.1 Experimental

Dipeptides VF and FV were purchased from Bachem without further purification. Each dipeptide was dissolved in D_2O for a final concentration of 150mM. Aliquots of the dipeptide solutions were placed between two calcium fluoride (CaF_2) windows separated by a 25μm Teflon spacer. FTIR spectra were collected using a Vertex 70 with 1 cm^{-1} steps and averaging 64 spectra. Second derivative spectra were smoothed using a Savitzky-Golay filter and scaled by a factor of -4.5 for VF and -1.5 for FV.

Two-dimensional infrared spectra were collected on a home built 2D IR spectrometer, described in greater detail elsewhere. Briefly, a Ti:Sapphire laser operating at 1 kHz generating pulses centered at 790 nm and sub-50fs pulse durations with 2.7 mJ of energy per pulse, was used to pump an optical parametric amplifier (OPA). The OPA generates mid-IR light centered at 6000 nm with 9μJ of energy per pulse and a

FWHM pulse duration of 100fs. A 90:10 beam splitter was used to send 90% of the mid-IR light to a pulse shaper to produce the pump pulses necessary for the 2D IR experiments; the remaining 10% of the mid-IR light was directed into a beam line to produce the necessary probe pulse in the experiments. An acoustic optical modulator (AOM) pulse shaper was used to generate a pulse pair with a specified phase, amplitude, and time delay. The phase, amplitude, and time delays were controlled by driving a series of acoustic waveforms, or masks, across the germanium crystal in the AOM. The time delays between the two pump pulses were scanned from 0 ps to 2.5 ps with 0.025 ps steps. Masks were generated to employ a four-frame phase cycling scheme and a 1400 cm^{-1} rotating frame to reduce both noise and the number of pulse delays required in the spectrum[18]. A computer-controlled delay stage temporally overlapped the pump and probe beams at the sample position. This stage also delayed the probe pulse from 0 ps to 4 ps with 0.1ps steps for chemical exchange experiments. A half-wave plate and polarizer where placed in the pump line to rotate the polarization of the pump light to collect data for cross-polarized and co-polarized experiments. The 2D IR signal is frequency resolved by passing the time domain signal through a grating spectrometer (Triax 190, Horiba) and collecting the signal on a 64-element mercury cadmium telluride (MCT) array detector. The geometry of the spectrometer taken together with the physical size and spacing of the MCT elements produces 5 cm^{-1} resolution along the probe axis of the 2D IR spectrum. The signal-to-noise ratio was improved by multiplying the signal from each pixel by a Hanning window function prior to taking the fast Fourier transform (FFT)[19]. Magic angle spectra where calculated to remove the rotational contribution to the decay rates[20] using spectra collected in the co-polarized (XXXX) configuration and the cross-polarized (XXYY) configuration in accord with the equation XXXX-2·XXYY. In addition, a spline function was used to better differentiate the areas of integration in the 2D IR spectrum.

3.2.2 Methods: Computational

Geometry optimizations and frequency calculations were performed at the ωB97xD/6-311G* level of theory using the Gaussioan09 software package[21,22]. All calculations used the PCM implicit solvent model in an effort to replicate solvent effects. Nitrogen bound hydrogens were deuterated in quantum

calculations as they are experimentally deuterium exchangeable. The frequencies are scaled by a factor of 0.956.

Individual dipeptide molecules in the L-enantiomer zwitterionic conformer were initially generated using the sequence command in tleap within the AmberTools 16 package[23]. All simulations were performed in explicit TIP3P water in the NPT ensemble using the GPU accelerated AMBER16 program[23,24,25]. Simulations with one dipeptide were performed at a concentration of 4 mg/mL for 300 ns for both VF and FV. These systems were then simulated for an additional 10 ns with a 10 fs write frequency in order to better measure hydrogen bonding rates. The ff14ipq force field was chosen due to agreement between experiment and quantum calculations relative to other commonly used Amber force fields.[16,26] A Monte Carlo barostat set to 1 bar and a Langevin thermostat set to 298 K are used. All simulations used an integration timestep of 2 fs with the SHAKE algorithm restraining the bond lengths of bonds including a hydrogen atom. A non-bonding interaction cutoff of 12 Å was used in all simulations with the particle mesh Ewald method calculating long range electrostatic interactions.

The following protocols were performed prior to production runs of unbiased simulations. A steepest descent energy minimization protocol was first performed for 8000 steps, followed by the conjugate gradient method for 4000 steps. During this initial energy minimization, restraints were placed on the peptide atoms with a force constant of 100 kcal/mol/Å^2. The restraints were removed and an energy minimization procedure was again performed with a steepest descent protocol for 12000 steps followed by a conjugate gradient method for 6000 steps. With restraints again placed on the peptide atoms with a force constant of 5 kcal/mol/Å^2, the systems were heated from 0 K to 298 K at constant volume. After heating, the volume was then allowed to relax for 40 ps with restraints kept on the peptides. To avoid transient effects due to initial configurations, productions runs were started after 3 ns of unbiased simulation. The unbiased simulations of FV and VF monomer systems each were simulated for 300 ns for a total of 600 ns.

Umbrella sampling was performed along the N-terminal $\chi 1$ for the FV dipeptide as this dihedral is conformationally restricted. Starting in the conformation produced through tleap, steered umbrella

sampling was used to sample N-terminal χ1 dihedral values with windows ranging from -180° to 180° in 10° increments. A harmonic potential was placed on each window of 0.12184 kcal/mol/deg^2. Each window was simulated for 50 ns for a total of 3.65 μs and a potential of mean force was generated using the weighted histogram method[27].

Dihedral and hydrogen bonding analyses of simulated trajectories were performed using python 2.7 and the MDAnalysis module (version 0.18.0).[28,29] Hydrogen bonding environment rates were then measured assuming classical inference. The VMD software was used to visualize trajectories and generate structural figures[30].

3.3 Results and Discussion

Figure 3.1 shows FTIR spectra, FTIR second derivative spectra, and 2D IR spectra of VF and FV. The FTIR spectra, shown in black, for VF, Figure 3.1a, and for FV, Figure 3.1c, show two vibrational transitions. One corresponding with the carboxylate group, located at 1597 cm^{-1} in VF and at 1590 cm^{-1} in FV. The other absorption reports on the Amide I mode of the dipeptide, appearing at 1661 cm^{-1} in VF and 1665 cm^{-1} in FV. Figures 1a and 1c also contain second derivative spectra, blue curves, that identify different vibrational transitions that lie underneath a single FTIR peak[20,31]. These second derivative spectra are scaled by a factor of -1.5, VF, and -4, FV. Therefore, each maximum of the second derivative spectra corresponds with an underlying vibrational mode. From these second derivative spectra, the amide I mode in each dipeptide contains two separate vibrational frequencies. VF has modes at 1651 cm^{-1} and 1665 cm^{-1} and FV has vibrational transitions at 1664 cm^{-1} and 1668cm^{-1}. The carboxylate mode in VF has three modes, 1583 cm^{-1}, 1596 cm^{-1}, and 1604 cm^{-1}. The dipeptide FV only contains two carboxylate transitions at 1590 cm^{-1} and 1606 cm^{-1}. Figures 2B and 2D show 2D IR spectra of each dipeptide.

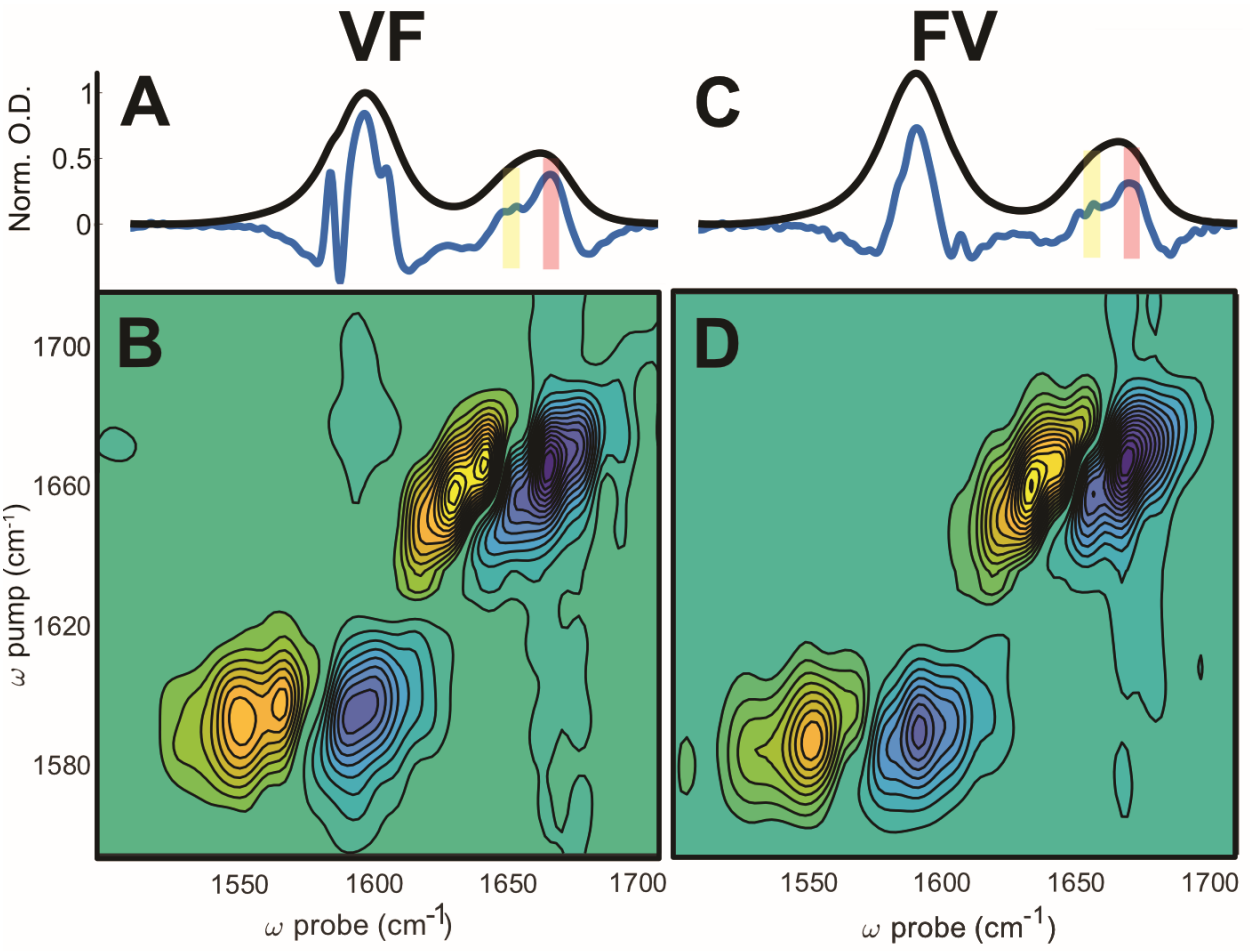

Figure 3.1 Linear infrared spectra shown in black, second derivative spectra shown in blue, and 2D IR spectra of VF and FV.

The underlying structures from the second derivative FTIR spectra indicate both isomers exist in multiple conformations. MD simulations were performed to elucidate the different conformations of each dipeptide. Figure 3.2 shows the Ramachandran plots for each isomer. Within each plot, a percentage of the probability density is listed next to each φ/ψ conformation. These plots show FV has only one predominate φ angle, in contrast to the two for VF.

Quantum mechanic geometry optimization and frequency calculations were performed on the structures isolated from the MD simulations. The results of the frequency calculation are shown in Figure 4.3 In Figure 4.3, the weighted spectra are a convolution of the calculated amide I frequency from the four different configurations found in the Ramachandran plots scaled with their relative intensities.

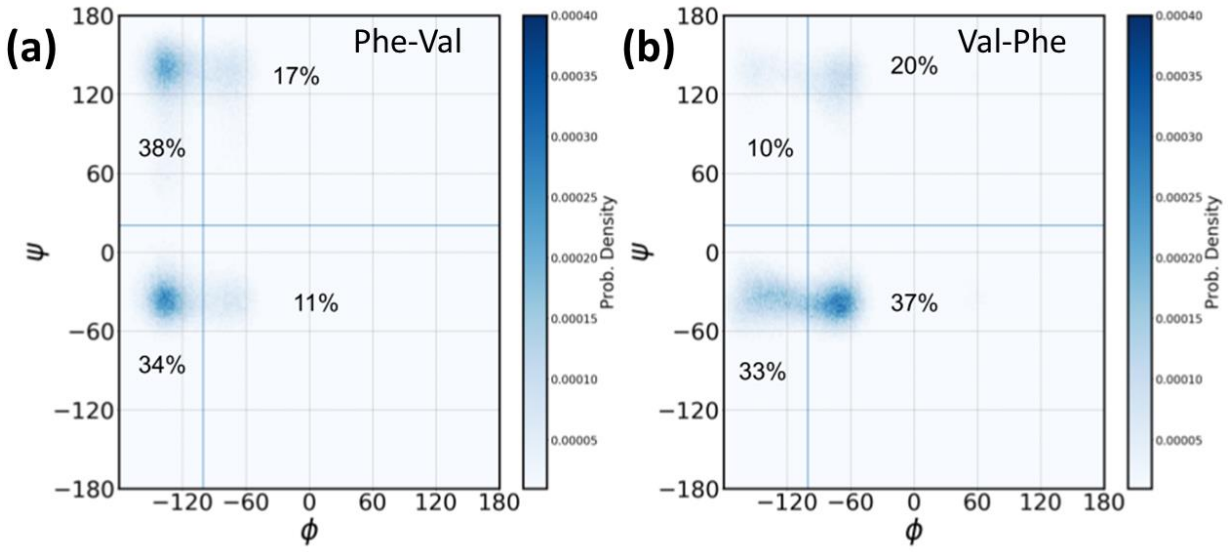

Figure 3.2 Ramachandran plots of FV (a) and VF (b). Each dipeptide has four ϕ/ψ angle populations. However, probability density distribution is different for each dipeptide.

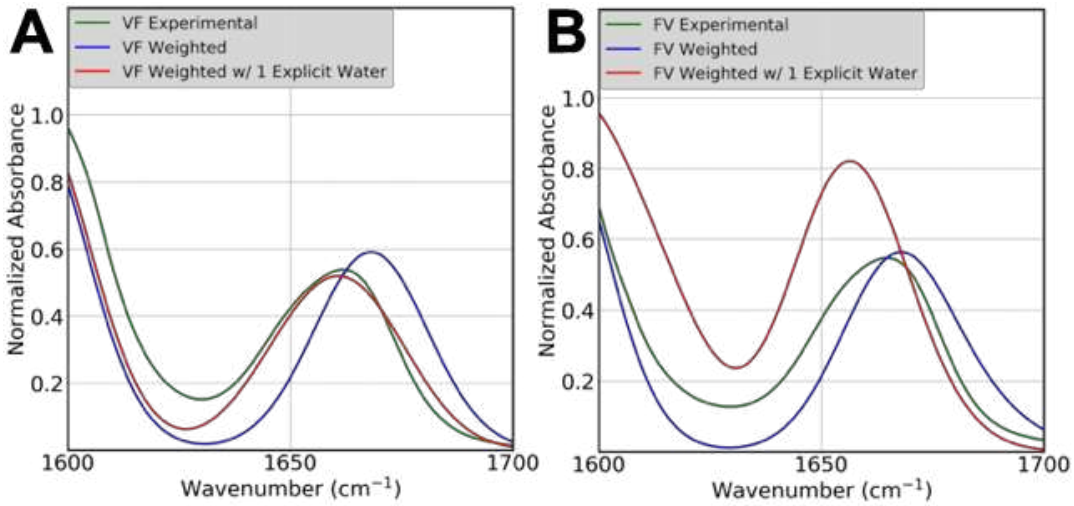

Figure 3.3 Plot of calculated spectra alongside experimental linear infrared spectra of VF, (a), and FV, (b). Weighted frequency calculations are shown in blue, weighted frequencies with an explicit water molecule are shown in red, and experimental spectra are plotted in green.

Computational and experimental results show that the primary structure of the dipeptide will influence the structural conformation and the IR spectrum. Furthermore, the second derivative spectra show different transitions under the amide I peak. This indicates different chemical environment. It was therefore hypothesized that the dipeptide would transition from one environment to another. Chemical experiments

were performed on each dipeptide to monitor the rate of transfer from one state to another. Peak positions were located based on the locations of the transitions in the second derivative spectra. Integration windows were defined for these locations and integrated over for all time steps. The intensities of the integration windows were plotted as a function of time and fit to a single exponential function. These results are shown in Figure 4.4, where Figure 4.4.A is the spectra for VF and Figure 3.4B is the spectra for FV. The red circles indicate the location of the integration areas. Integration peaks are labeled A and B with their corresponding cross peak labeled as AB.

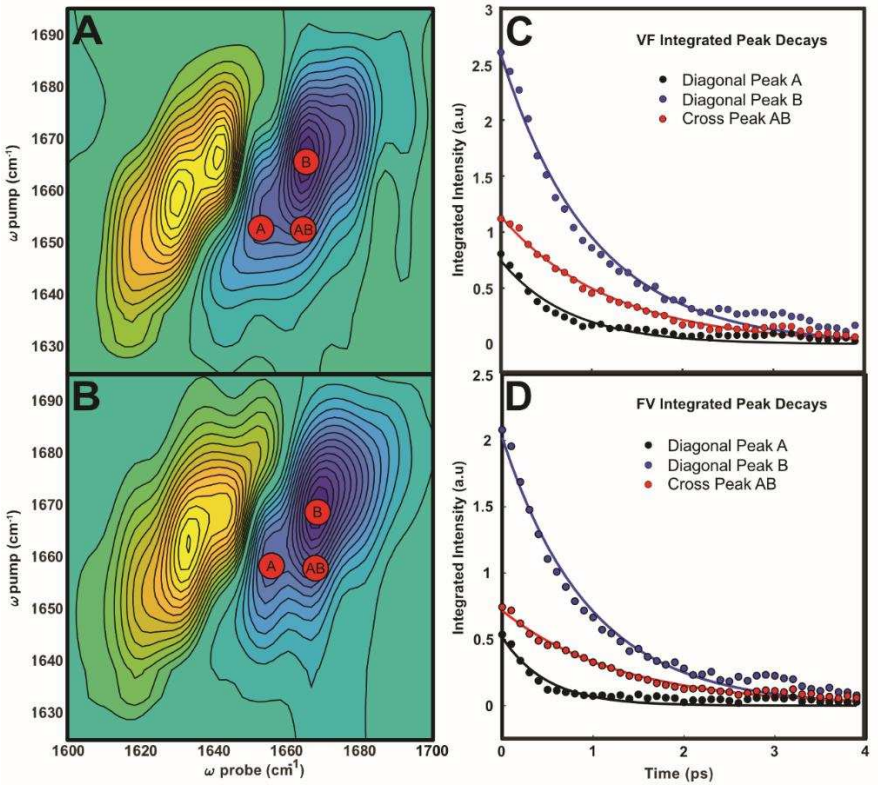

Figure 3.2. Amide I region of VF, Figure 3.4A, and FV, Figure 3.4B. In panel A and B the red circles indicate where the integration box was defined for the on diagonal peaks and cross peaks. Figures 3.4C and 3.4D plot the lifetime decays of the three spectral regions of interest in both dipeptide systems.

Table 3-1. Vibrational decay rates determined from 2D IR waiting time experiments of both dipeptide isomers.

	Vibrational Life Time in D_2O (ps)		
	Transition A (ps)	Transition B (ps)	Cross Peak AB (ps)

VF	0.75 ± 0.08	1.00 ± 0.05	1.21 ± 0.05
FV	0.50 ± 0.07	0.97 ± 0.05	1.70 ± 0.25

$$k_{CP} \cong \frac{k_B + k_A}{2} - \sqrt{\left(\frac{k_B - k_A}{2}\right)^2 + k_{BA}k_{AB}} \tag{3.1}$$

The vibrational lifetimes generated from these fits were used in Equation 3.1 to determine the rate constant associated with chemical exchange. These decay rate constants are shown in Table 3-1. By inserting the rates shown in Table 3-1 and solving for $k_{AB}k_{BA}$ in Equation 1 the exchange rate constant were determined to be $(3.46 \pm 0.60 \text{ ps})^{-1}$ for VF and $(1.7 \pm 0.25 \text{ ps})^{-1}$ for FV. This was done by assuming k_{AB} is equal to k_{BA}. These exchange rates are too fast for peptide conformational changes, typically in the tens of femtoseconds, but are comparable to rate of hydrogen making and breaking. Based on this hypothesis peak B would be the peptide in a hydrogen bonded environment and peak A would be in a nonbonded environment for both dipeptides. Computational hydrogen bonding dynamics were generated from MD simulations for the four conformations of each dipeptide. These are tabulated in terms the length of hydrogen bond lifetime, shown in Table 3-2.

Table 3-2. Computational hydrogen bond lifetime for each conformation of FV and VF.

	Lifetime of water (ps)	
	FV	VF
State A	0.57	0.66
State B	0.66	0.60

State C	0.65	0.71
State D	0.60	0.68
State Averaged	0.62	0.67

Table 3-2 shows that the hydrogen of a water molecule stays coordinated longer to the amide I group in VF than FV. This is consistent with the observed longer vibrational lifetime of VF's hydrogen-bonded state as well as the slower exchange rate of VF. A structural explanation for this is shown in Figure 3.5. Figure 3.5 shows the four different structures from the Ramachandran plots seen in Figure 4.2. In Figure 3.5 each of FV and VF's conformation states, A, B, C, and D, are presented together to identify differences. The most significant difference is in state C. In state C the phenol ring of VF is positioned next to the peptide linkage. However, FV's phenol group is positioned away from the linkage. The result is a larger density of water surrounding the amide I group in VF versus FV. This larger water density would explain the slower vibrational lifetimes and slower exchange rates observed experimentally.

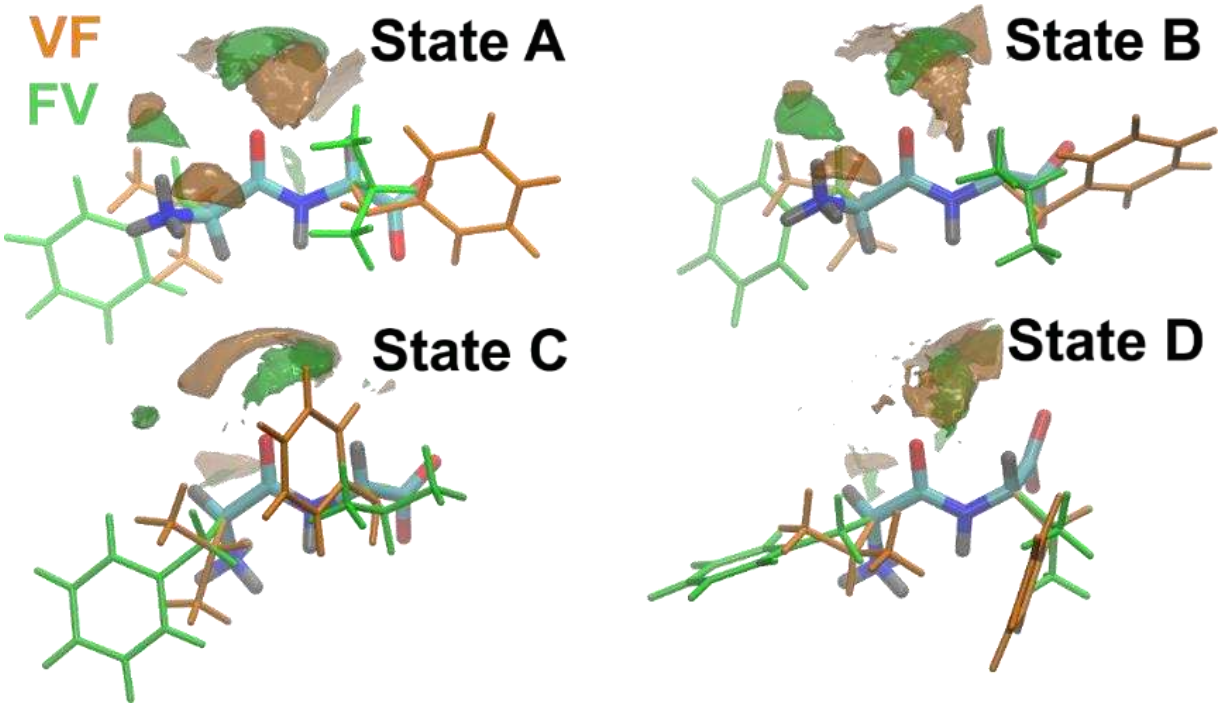

Figure 3.3 Depictions of the four conformation states of VF and FV with water density maps. Strong distinction can be seen in State C where VF's conformation has a larger water density surrounding its peptide linkage.

3.4 Conclusions

This work has shown differences between VF and FV's first solvation shells. Molecular dynamics simulations show conformational differences between the isomers resulting in an increase water density in VF. The increase in water density is observed experimentally from both longer vibrational lifetime of the hydrogen-bonded amide I stretch and slower transfer rates between a hydrogen bonded environment to a nonhydrogen-bonded environment.

References

(1) Görbitz, C. H. Nanotube Formation by Hydrophobic Dipeptides. *Chem. Eur. J.* **2001**, *7* (23), 5153–5159. https://doi.org/10.1002/1521-3765(20011203)7:23<5153::AID-CHEM5153>3.0.CO;2-N.

(2) Azuri, I.; Adler-Abramovich, L.; Gazit, E.; Hod, O.; Kronik, L. Why Are Diphenylalanine-Based Peptide Nanostructures so Rigid? Insights from First Principles Calculations. *J. Am. Chem. Soc.* **2014**, *136* (3), 963–969. https://doi.org/10.1021/ja408713x.

(3) Mahler, A.; Reches, M.; Rechter, M.; Cohen, S.; Gazit, E. Rigid, Self-Assembled Hydrogel Composed of a Modified Aromatic Dipeptide. *Adv. Mater.* **2006**, *18* (11), 1365–1370. https://doi.org/10.1002/adma.200501765.

(4) Zelenovskiy, P.; Kornev, I.; Vasilev, S.; Kholkin, A. On the Origin of the Great Rigidity of Self-Assembled Diphenylalanine Nanotubes. *Phys. Chem. Chem. Phys.* **2016**, *18* (43), 29681–29685. https://doi.org/10.1039/c6cp04337b.

(5) Schnaider, L.; Brahmachari, S.; Schmidt, N. W.; Mensa, B.; Shaham-Niv, S.; Bychenko, D.; Adler-Abramovich, L.; Shimon, L. J. W.; Kolusheva, S.; DeGrado, W. F.; et al. Self-Assembling Dipeptide Antibacterial Nanostructures with Membrane Disrupting Activity. *Nat. Commun.* **2017**, *8* (1), 1365. https://doi.org/10.1038/s41467-017-01447-x.

(6) Huang, R.; Qi, W.; Su, R.; Zhao, J.; He, Z. Solvent and Surface Controlled Self-Assembly of Diphenylalanine Peptide: From Microtubes to Nanofibers. *Soft Matter* **2011**, *7* (14), 6418–6421. https://doi.org/10.1039/C1SM05752A.

(7) Rissanou, A. N.; Georgilis, E.; Kasotakis, E.; Mitraki, A.; Harmandaris, V. Effect of Solvent on the Self-Assembly of Dialanine and Diphenylalanine Peptides. *J. Phys. Chem. B* **2013**, *117* (15), 3962–3975. https://doi.org/10.1021/jp311795b.

(8) Mayans, E.; Ballano, G.; Sendros, J.; Font-Bardia, M.; Campos, J. L.; Puiggalí, J.; Cativiela, C.; Alemán, C. Effect of the Solvent Choice in the Self-Assembly Properties in a Diphenylalanine Amphiphile Stabilized by an Ion Pair. *ChemPhysChem* **2017**, *300*, 625. https://doi.org/10.1002/cphc.201700180.

(9) Wang, J.; Liu, K.; Yan, L.; Wang, A.; Bai, S.; Yan, X. Trace Solvent as a Predominant Factor To Tune Dipeptide Self-Assembly. *ACS Nano* **2016**, *10* (2), 2138–2143. https://doi.org/10.1021/acsnano.5b06567.

(10) Wijerathne, N. K.; Kumar, M.; Ulijn, R. V. Fmoc-Dipeptide/Porphyrin Molar Ratio Dictates Energy Transfer Efficiency in Nanostructures Produced by Biocatalytic Coassembly. *Chem. Eur. J.* **2019**, chem.201902819. https://doi.org/10.1002/chem.201902819.

(11) Sahoo, J. K.; Nazareth, C.; VandenBerg, M. A.; Webber, M. J. Self-Assembly of Amphiphilic Tripeptides with Sequence-Dependent Nanostructure. *Biomater. Sci.* **2017**, *5* (8), 1526–1530. https://doi.org/10.1039/C7BM00304H.

(12) Kar, K.; Wang, Y.-H.; Brodsky, B. Sequence Dependence of Kinetics and Morphology of Collagen Model Peptide Self-Assembly into Higher Order Structures. *Protein Science* **2008**, *17* (6), 1086–1095. https://doi.org/10.1110/ps.083441308.

(13) Frederix, P. W. J. M.; Ulijn, R. V.; Hunt, N. T.; Tuttle, T. Virtual Screening for Dipeptide Aggregation: Toward Predictive Tools for Peptide Self-Assembly. *J. Phys. Chem. Lett.* **2011**, *2* (19), 2380–2384. https://doi.org/10.1021/jz2010573.

(14) Frederix, P. W. J. M.; Scott, G. G.; Abul-Haija, Y. M.; Kalafatovic, D.; Pappas, C. G.; Javid, N.; Hunt, N. T.; Ulijn, R. V.; Tuttle, T. Exploring the Sequence Space for (Tri-

)Peptide Self-Assembly to Design and Discover New Hydrogels. *Nature Chem* **2015**, *7* (1), 30–37. https://doi.org/10.1038/nchem.2122.

(15) Yan, X.; Zhu, P.; Li, J. Self-Assembly and Application of Diphenylalanine-Based Nanostructures. *Chem. Soc. Rev.* **2010**, *39* (6), 1877–1890. https://doi.org/10.1039/b915765b.

(16) Anderson, J.; Lake, P. T.; McCullagh, M. Initial Aggregation and Ordering Mechanism of Diphenylalanine from Microsecond All-Atom Molecular Dynamics Simulations. *The Journal of Physical Chemistry B* **2018**, *122* (51), 12331–12341. https://doi.org/10.1021/acs.jpcb.8b10335.

(17) de Groot, N. S.; Parella, T.; Aviles, F. X.; Vendrell, J.; Ventura, S. Ile-Phe Dipeptide Self-Assembly: Clues to Amyloid Formation. *Biophys. J.* **2007**, *92* (5), 1732–1741. https://doi.org/10.1529/biophysj.106.096677.

(18) Shim, S.-H.; Zanni, M. T. How to Turn Your Pump–Probe Instrument into a Multidimensional Spectrometer: 2D IR and Vis Spectroscopies via Pulse Shaping. *Phys. Chem. Chem. Phys.* **2009**, *11* (5), 748–761. https://doi.org/10.1039/B813817F.

(19) MacKenzie, K. J. D.; Smith, M. E. *Multinuclear Solid-State NMR of Inorganic Materials*, 1st ed.; Pergamon materials series; Pergamon: Oxford ; New York, 2002.

(20) Feng, C. J.; Tokmakoff, A. The Dynamics of Peptide-Water Interactions in Dialanine: An Ultrafast Amide i 2D IR and Computational Spectroscopy Study. *Journal of Chemical Physics* **2017**, *147* (8). https://doi.org/10.1063/1.4991871.

(21) Chai, J.-D.; Head-Gordon, M. Long-Range Corrected Hybrid Density Functionals with Damped Atom–Atom Dispersion Corrections. *Phys. Chem. Chem. Phys.* **2008**, *10* (44), 6615–6620. https://doi.org/10.1039/b810189b.

(22) Frisch, M. J.; Trucks, G. W.; Schlegel, H. B.; Scuseria, G. E.; Robb, M. A.; Cheeseman, J. R.; Barone, V.; Mennucci, B.; Petersson, G. A.; Nakatsuji, H.; et al. *Gaussian ~09, Revision D.01*; Gaussian, Inc.: Wallingford CT, 2013.

(23) Case, D. A.; Cerutti, D. S.; Cheatham, "T.E., 3rd"; Darden, T. A.; Duke, R. E.; Giese, T. J.; Gohlke, H.; Goetz, A. W.; Greene, D.; Homeyer, N.; et al. *AMBER 2017*; University of California, San Francisco, 2017.

(24) Salomon-Ferrer, R.; Götz, A. W.; Poole, D.; Le Grand, S.; Walker, R. C. Routine Microsecond Molecular Dynamics Simulations with AMBER on GPUs. 2. Explicit Solvent Particle Mesh Ewald. *J. Chem. Theory Comput.* **2013**, *9* (9), 3878–3888. https://doi.org/10.1021/ct400314y.

(25) Le Grand, S.; Götz, A. W.; Walker, R. C. SPFP: Speed without Compromise—A Mixed Precision Model for GPU Accelerated Molecular Dynamics Simulations. *Computer Physics Communications* **2013**, *184* (2), 374–380. https://doi.org/10.1016/J.CPC.2012.09.022.

(26) Cerutti, D. S.; Swope, W. C.; Rice, J. E.; Case, D. A. Ff14ipq: A Self-Consistent Force Field for Condensed-Phase Simulations of Proteins. *J. Chem. Theory Comput.* **2014**, *10*, 4515–4534. https://doi.org/10.1021/ct500643c.

(27) Kumar, S.; Rosenberg, J. M.; Bouzida, D.; Swendsen, R. H.; Kollman, P. A. THE Weighted Histogram Analysis Method for Free-Energy Calculations on Biomolecules. I. The Method. *J. Comput. Chem.* **1992**, *13* (8), 1011–1021. https://doi.org/10.1002/jcc.540130812.

(28) Gowers, R. J.; Linke, M.; Barnoud, J.; Reddy, T. J. E.; Melo, M. N.; Seyler, S. L.; Domański, J.; Dotson, D. L.; Buchoux, S.; Kenney, I. M.; et al. MDAnalysis: A Python Package for the Rapid Analysis of Molecular Dynamics Simulations. In *Proceedings of the 15th Python in Science Conference*; Benthall, S., Rostrup, S., Eds.; 2016; pp 98–105.

(29) Michaud-Agrawal, N.; Denning, E. J.; Woolf, T. B.; Beckstein, O. MDAnalysis: A Toolkit for the Analysis of Molecular Dynamics Simulations. *Journal of Computational Chemistry* **2011**, *32* (10), 2319–2327. https://doi.org/10.1002/jcc.21787.

(30) Humphrey, W.; Dalke, A.; Schulten, K. VMD – Visual Molecular Dynamics. *J. Mol. Graph.* **1996**, *14*, 33–38.

(31) Rieppo, L.; Saarakkala, S.; Närhi, T.; Helminen, H. J.; Jurvelin, J. S.; Rieppo, J. Application of Second Derivative Spectroscopy for Increasing Molecular Specificity of Fourier Transform Infrared Spectroscopic Imaging of Articular Cartilage. *Osteoarthritis and Cartilage* **2012**, *20* (5), 451–459. https://doi.org/10.1016/j.joca.2012.01.010.

Chapter 4

Vibrational Properties and Population Transfer Rates of Solvent Dependent Violanthrone-79 Aggregates

This chapter is based on a manuscript that will be submitted to the American Chemical Society's Journal of Physical Chemistry B in 2019. In this work, I designed experiments to examine the vibrational exciton properties of violathrone-79. I also worked with my colleague Max A. Mattson to use molecular dynamics simulations and quantum mechanics calculations to study the possible violathrone-79 aggregates.

4.1 Introduction

Understanding molecular aggregation driven by π-stacking is critical for elucidating a variety of self-assembled systems. The π-π interaction of aromatic compounds is key for the self-assembly of DNA[1,2], protein tertiary structure[3,4], and polycyclic aromatic hydrocarbons (PAH)[5–7]. These polycyclic aromatic hydrocarbons are generally classified as organic species with fused poly-aromatic cores, and are particularly interesting because they are used as the precursor to many material science disciplines.

Control over functionalizing PAH have led to technological advancements in solar cells[8], laser dyes[9], and liquid crystals[10]. However, tailoring functional groups on the PAH core is only one knob to manipulate the molecular aggregation of these organic dyes. The choice of solvent is also crucial to controlling the structural characteristics of PAH aggregates. A great deal of work has been focused on the effect solvent has on π-π interaction[11–13]. Research has shown that a polar solvent will promote π-π interaction as explained by solvophobic theory. However, the effect of solvent polarity on molecular orientation and energy delocalization, concepts that are critical in

photoelectrochemical cells, is still unclear. Molecular orientation and its impact on energy delocalization can be explored by employing experimental techniques that examine vibrational characteristics in PAH aggregates. In doing so, the effect of solvent on structural and energy delocalization properties can be better understood.

One PAH that has received attention over the years is violanthrone. Violanthrone is a PAH that has been used as an analog to asphaltenes, but it has also shown promise as an organic dye for solar cell technology due to its large aromatic core making it ideal for absorbing solar radiation. Recently, investigations have examined how the polarity of the solvent influences the degree of π-π interactions in violanthrone aggregates.[14] These efforts have revealed that non-polar solvents promote π-π interaction, which is in contrast with other aromatic π stacking systems. However, little work has been done to understand how the structural characteristics of violanthrone aggregates are influenced by solvent effects or how the aggregate structural characteristics influence the movement of vibrational energy through the molecule. In this work, vibrational modes of violanthrone-79 (V-79) are used to characterize the aggregate structures formed in different solvents.

Vibrational spectroscopy experiments, including linear infrared (IR) spectroscopy and two-dimensional infrared (2D IR) spectroscopy, are a powerful techniques to observe the structural and dynamic characteristics of a molecular system. The vibrational modes of a molecular system are sensitive to changes in the local environment surrounding it and aggregate structure. The energies and dipole strengths of the vibrational modes in the aggregate can be modulated by changes in local environment surrounding the oscillators and changes in the structures of the molecular aggregates. Changes in the vibrational characteristics of the aggregates can be monitored with linear IR spectroscopy and 2D IR spectroscopy techniques. In particular, 2D IR spectroscopy,

provides structural information on molecular aggregates through the examination of cross peaks observed in the spectra. In addition, 2D IR experiments can be used to probe dynamic properties of a system by monitoring how 2D IR peak shapes and intensities change as a function of delay times between pulses in the experiments. 2D IR spectroscopy experiments have been used at length to better understand the structure of DNA[1], proteins[3], PAH[5], and anti-HIV agents[15]. Chemical dynamics investigated with 2D IR spectroscopy have contributed to our understanding of solvent dynamics and structural dynamics of water[16], dipeptides, and membranes.[17] In this work, we take advantage of these strengths of 2D IR experiments to study molecular aggregates of violanthrone and the manner in which the aggregate structure influences the vibrational energy delocalization within the aggregates. In addition, the interpretation of the experimental results is aided with molecular dynamics (MD) simulations and quantum mechanic (QM) calculations to explore the possible aggregate structures formed by V-79. Solvent-dependent aggregate structures of V-79 are observed and changes in the vibrational energy transfer between V-79 molecules in the aggregates are discussed.

4.2 Methods:

4.2.1 Experimental

Violanthrone-79 was purchased from Ark Pharma and used without further purification. THF and $HCCl_3$ were purchased from Fisher scientific. Samples of V-79 where prepared at 10 mM concentration in each solvent and sonicated to insure full solvation prior to aggregation. Aliquots of stock solutions were placed between two calcium fluoride (CaF_2) windows with a 250μm spacer. Linear IR spectra were collected with 1 cm^{-1} spectral resolution and are an average of 64 spectra (Vertex 70 spectrometer, Bruker).

The 2D IR spectrometer used here has been described in detailed elsewhere.[6,7] Briefly, ultrafast mid-IR pulses were generated using a Ti:Sapphire regenerative amplifier to pump an optical parametric amplifier (OPA). The regenerative amplifier produces <50 fs laser pulses centered at 790 nm with an average pulse energy of 2.7 mJ at a repetition rate of 1 kHz. The OPA generates mid-IR light centered at 5800 nm with 9 μJ of energy per pulse. A 90:10 beam splitter is used to direct 90% of the mid-IR light to a home-built pulse shaper used to generate the pulse pairs with specified time delays required to pump the sample and generate third order signal in these experiments. The remaining 10% of the mid-IR light from the OPA is used as a probe pulse in these 2D IR experiments. An off-axis parabolic mirror is used to focus the pump and probe beams onto the sample in the pump-probe beam geometry. A retro-reflector set on a computer-controlled stage is used to control the time delay of the probe pulse relative to the pump pulses. The computer-controlled time delay is also used to control the timing between the second and third laser pulses when collecting 2D IR spectra as a function of coherence time, T_w. A second off-axis parabolic mirror collimates the third order signal field emitted from the sample and directs it into a Horiba Triax 190 spectrometer. The spectrometer is used to frequency resolve the signal across a 64-element mercury cadmium telluride (MCT) detector. The spectrometer geometry in conjunction with the physical geometry of the array detector produces data with ~5cm^{-1} spectral resolution.

The AOM-based mid-IR pulse shaper is used to control the amplitude and phase of the individual frequencies in the mid-IR optical pulse.[18–20] This allows the relative phase and time delays between the pulses generated in the pulse pair to be changed with each acoustic wave. In these experiments, pump pulses were scanned from 0 ps to 2.5 ps with 0.025 ps steps; a 1400 cm^{-1} rotating frame was applied to allow for faster data collection.[20] T_w-dependent 2D IR spectra were

collected from 0 ps to 8 ps in 0.1 ps steps for the first 5 ps and with intervals of 1 ps from 5 ps to 8 ps. Additional pulse shaping was used in some data sets to remove contributions from quantum beating and coherence transfer. The pump pulses were clipped at 1615 cm^{-1} in order to only pump the vibrational modes above 1615 cm^{-1}. The pump pulses were truncated in the frequency domain by blocking a portion of the beam at the Fourier plane of the pulse shaper. This approach allowed for the carbonyl normal mode to be pumped without pumping the normal modes associated with the in-plane stretching motions of V-79.

Polarization dependent experimental were conducted on V-79 aggregates in both solvents to determine relative angle between vibrational normal modes. For these experiments, polarization dependent 2D IR spectra were collected in both XXXX and XXYY polarization configurations. The polarizations were controlled using a half-waveplate and wire grid polarizer combination in the pump beam path to rotate the beam 90°. Furthermore, a wire grid polarizer was placed in the probe beam path to insure a single polarization of mid-IR light was impinging on the sample.

4.2.2. Methods: Molecular Dynamics

Molecular Dynamics (MD) simulations were performed using Replica Exchange Umbrella Sampling (REUS) in the AMBER molecular dynamics software package,[21] to sample the potential energy surface of dimerization between two V-79 molecules in $HCCl_3$ and THF as a function of center-of-mass distance between the two molecules. V-79 was parameterized using GAFF[22] and charges were found with RESP;[23] the AMBER chloroform box was used for the solvent,[24] and a self-parameterized THF model was used. Harmonic biasing potentials were placed 0.5 Å apart along the collective variable axis and were given spring constants of 20.0 kcal mol^{-1} $Å^{-2}$. The resultant center-of-mass distances were analyzed using the weighted histogram analysis method (WHAM)[25] to build the potential of mean force (PMF). The PMF was constructed using a home

built binning script to check for non-ergodicity among the biased windows. Each window in the REUS simulations was run for 100 ns in the NPT ensemble.

4.2.3. Methods: Quantum Calculations

Vibrational frequency calculations were performed using Gaussian 09 for the V-79 dimer structures that were representative of the two most probable π-stacked dimer configurations. The APFD functional was used for its dispersive properties to stabilize π-stacking interactions between the two monomers. During the geometry optimization four atoms on each molecule were frozen to keep the relative orientation of the molecules unchanged; the atoms chosen were not active in the pertinent normal modes being studied in this work. As stated in our previous work, this will lead to imaginary frequencies in vibrational modes comprised of these atoms, so we also gave each frozen atom a mass of 1000 AMU to effectively remove its contribution from the vibrational frequency calculation. As a result, each of the V-79 dimer structures were effectively frozen in their initial configurations, able to rotate or translate minimally relative to one another. The protocol described here is essential because the relative orientations of the monomers in the dimer configuration govern the strength and nature of vibrational coupling between the monomer units. Without instituting this position constraining procedure, the dimers change relative orientations and positions significantly during the geometry optimization and differences in relative orientations are lost.

4.3. Results and Discussion

Figure 2a and 2b present the linear IR spectra of 10mM V-79 in $HCCl_3$ and THF. Each spectrum contains four sperate spectroscopic features. These features are represented by the letters α, β, γ, δ. This investigation focuses on the features α and δ due to their correlation with the dominate ring mode and the carbonyl mode of V-79 respectively. Spectral features β and γ are ignored because of their relatively low

intensity. Comparing the carbonyl mode δ in both solvents reveal clear differences in height, width, and frequency position. The differences in the peak height and width suggest the aggregated carbonyl mode exists in different solvation environments, homogeneous in THF and inhomogeneous in HCC_3, depending on the aggregate formed. The cause behind the difference in frequency position was examined with MD and QM calculations and is discussed later in this section.

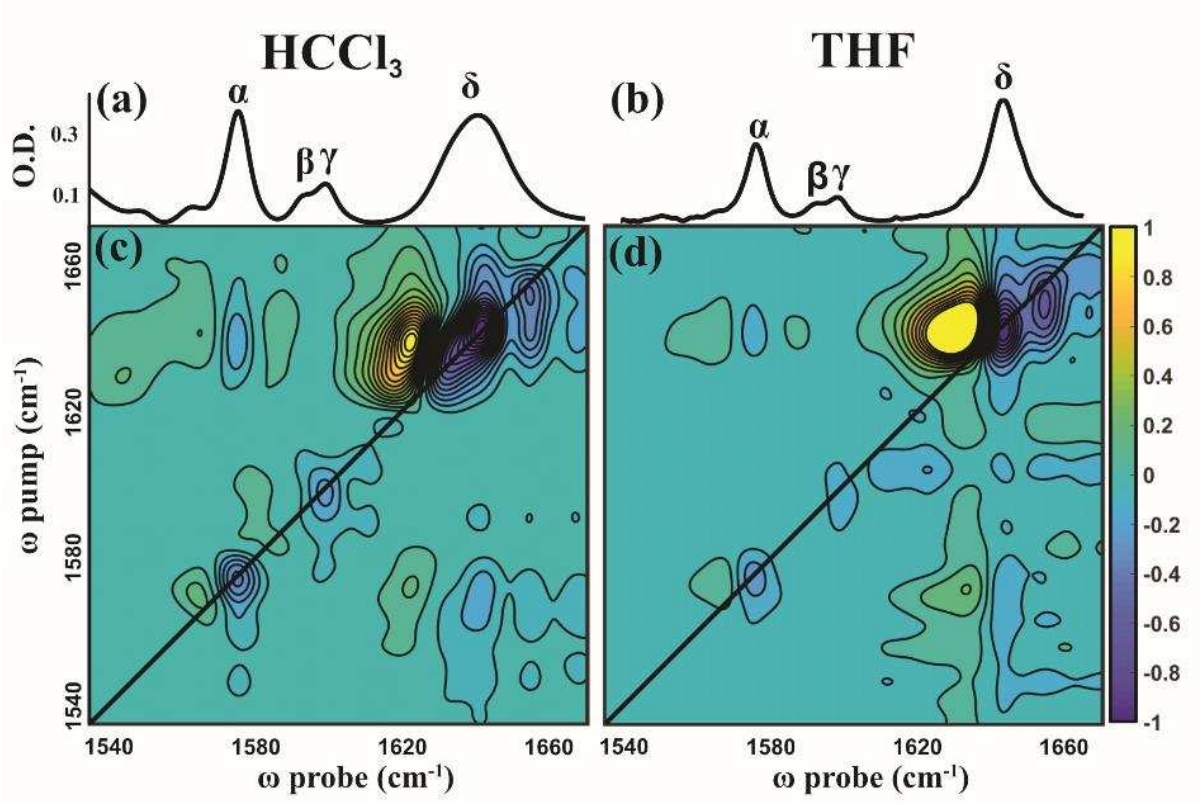

Figure 4.1 FTIR and 2D IR spectra of violanthrone-79 in $HCCl_3$, (a) and (c), and in THF, (b) and (d). Each sample was prepared at a 10 mM concentration.

Figure 4.1c and 4.1d show the 2D IR spectra of V-79 in $HCCl_3$ and THF. Within each spectrum there are three spectral features of interest. The diagonal peaks located at approximately pump-probe positions 1580cm^{-1} and 1640 cm^{-1} correspond with the transitions α and δ observed in Figures 4.1a and 4.12b. The differences in peak shape and intensity of the 2D IR feature located at pump-probe position 1640cm^{-1} is related to the differences in frequency distribution discussed above. The last notable 2D IR feature in Figures 4.1c and 4.1d is the cross peak between the ring and carbonyl modes located at pump position 1640cm^{-1} and probe position 1580cm^{-1}. The intensity of this cross peak relative to the on diagonal

feature located at pump-probe position 1640cm^{-1} will be used to examine the chemical dynamics of the molecular systems.

Figure 4.2 is a pictorial representation of the two different π stacking configurations isolated from MD simulations. Figure 4.2 a is the chemical structure of V-79, which can be split into two halves, shown as green and yellow. This splitting is important because there is an internal twist angle between each half in both dimer configurations. Figure 4.2 b shows V-79 in an antiparallel configuration while Figure 4.2 c presents V-79 in a parallel configuration. This parallel vs antiparallel distention is relative to colors, green or yellow, being on top of one another or across. The MD simulations showed the ratio of antiparallel to parallel stacks are solvent dependent, with a ratio of 11:1 in $HCCl_3$ and 2.5:1 in THF. From this ratio difference it can be hypothesized that THF promotes parallel π stacked V-79 aggregates, while $HCCl_3$ promotes antiparallel π stacked aggregates.

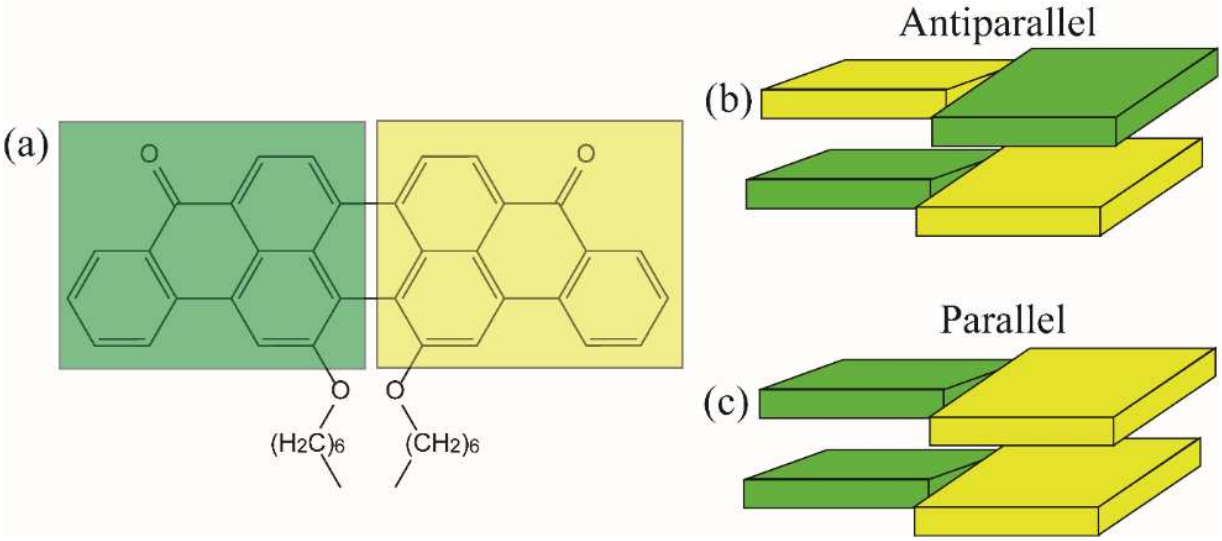

Figure 4.2 Representations of the two dimer states observed form MD simulations. The aromatic core of V-79 can be split into two parts, green and yellow, as shown in (a). V-79 has an internal twist angle between the two. V-79 can stack in either an antiparallel fashion (b), or in a parallel fashion (c). V-79 has an internal twist angle between its two haves as shown by the twist between green and yellow in (b) and (c).

Figure 4.3 shows the results of the QM frequency calculations on the antiparallel, 4a, and parallel, 4b, dimer configurations isolated from MD simulations shown in Figures 4.3b and 4.3c. These spectra are truncated to show only the modes related to the carbonyl region of the dimer. These results show each dimer

configuration contains four different carbonyl vibrational modes. However, the parallel configuration's center frequency is higher, 1745cm^{-1}, than the antiparallel configuration, 1735cm^{-1}. Figure 4.3b showed THF supported aggregates were at a higher vibrational frequency than $HCCl_3$ supported aggregates, Figure 4.3a. The hypothesis that THF promotes parallel π stacking and $HCCl_3$ promotes antiparallel is supported by comparing the relative frequency positions both experimentally, Figures 4.1a and 4.1b, and from QM calculations, Figures 4.3a and 4.3b. Quantum mechanics calculations also showed vibrational energy being delocalized across the parallel dimer configuration but localized in the antiparallel one. Cross relaxation rate 2D IR experiments were used to investigate this energy delocalization.

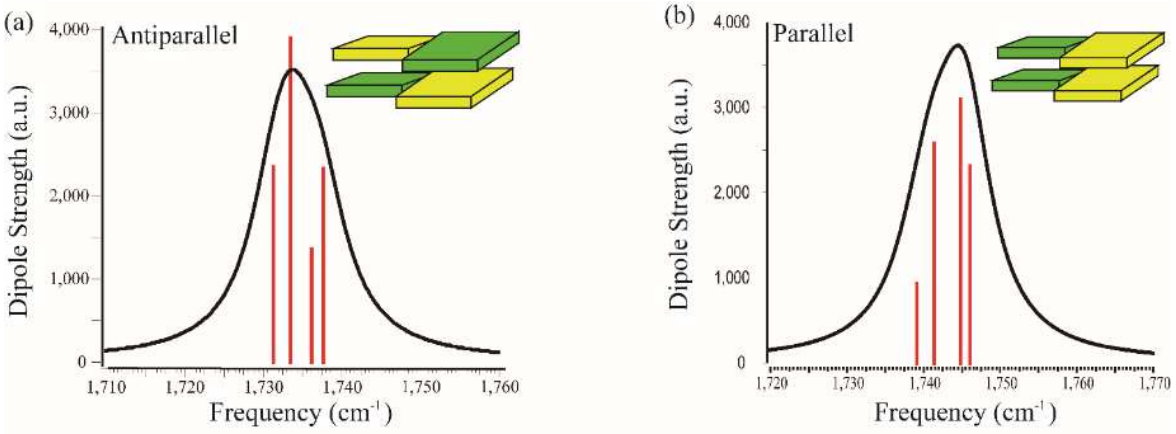

Figure 4.3. QM calculated vibrational spectra for the two dimer configurations for V-79. Spectrum (a) is produced from the antiparallel structure and spectrum (b) from the parallel structure.

Time dependent clipped pump 2D IR experiments were used to examine vibrational energy transfer within the two aggregate systems. The pump spectra were clipped such that the ring mode α was not pumped, removing contributions from coherence transfer in the cross peak intensity. Spectra were collected from 0 ps out to 7.5 ps in 0.1 ps steps. The ratio of the integrated intensity between the cross peak located at pump position 1640cm^{-1} and probe position 1580cm^{-1} and the on diagonal peak at pump-probe position 1640cm^{-1} was found at each time step. This ratio is used to track the relative change in intensity, thereby taking into account the loss in intensity from the vibrational life time.

Figure 4.4 plots this intensity ratio as a function of time. In this figure, the THF supported aggregates are shown in black and the $HCCl_3$ supported aggregates are shown in red. Based on exponential

fits of the data shown in Figure 5, the cross relaxational energy transfer rate was found to be 4.4±1.2ps in THF and 7.2±1.4ps in $HCCl_3$. The faster rate observed in THF systems suggests vibrational energy is more delocalized in these systems when compared to $HCCl_3$ supported V-79 aggregates.

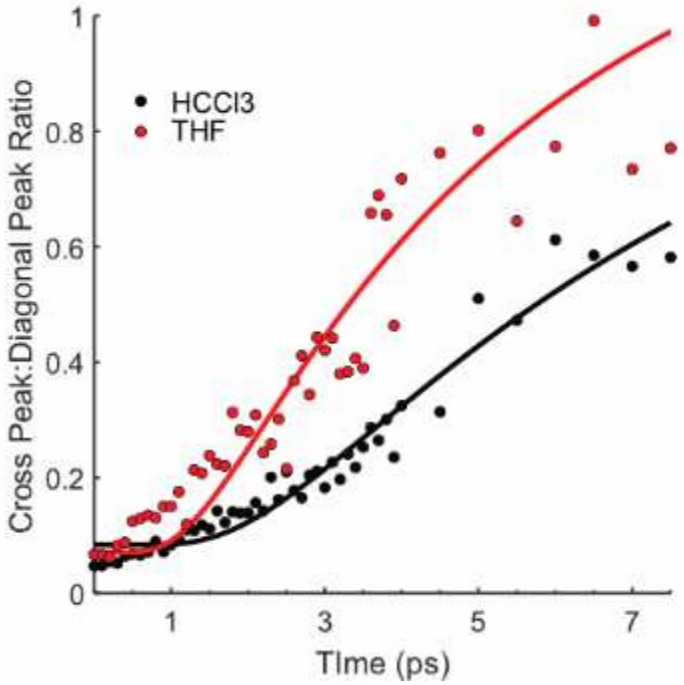

Figure 4.4. Plot of the peak ratio between the diagonal peak and cross peak of V-79 in each solvent system.

This work shows THF supports the formation of parallel π stacking V-79 aggregates, while $HCCl_3$ facilitates the formation of antiparallel π stacking V-79 aggregates. This is shown by comparing the relative frequency of carbonyl region, peak δ in the experimental linear spectra of Figures 2a and 2b with the QM frequency calculations shown in Figures 4a and 4b. Furthermore, the QM calculations showed vibrational energy was delocalized in parallel aggregates. Time dependent 2D IR measurements showed vibrational energy delocalization was greater in THF molecular systems. This observation of faster energy delocalization in THF supports the hypothesizes that THF supports parallel π stacking and $HCCl_3$ antiparallel π stacking in V-79.

4.4. Conclusions

Infrared spectroscopic techniques coupled with molecular dynamics simulations were used to examine different π-stacking environments in violanthrone-79. In the solvents $HCCl_3$ and THF, this work has shown that differences in the polarity of the solvent leads to differences in the π-stacking properties of the aggregates. From molecular dynamics simulations, two different dimer configurations were found, rotated and parallel. Using quantum mechanical frequency calculations, differences in frequency distribution and vibrational energy delocalization were found for each dimer configuration. By correlating these results with linear spectra and 2D IR population transfer experiments, the parallel structure has been assigned to $HCCl_3$ aggregates and rotated dimers to THF aggregates. This examination demonstrates moving to a more non-polar solvent like THF will disrupt the π-π interaction. In the case of V-79 aggregates, this disruption leads to a greater degree of vibrational energy delocalization. Elucidating the role of solvent choice in aggregate formation provides crucial information to yield parameters for controlling the aggregate structure formed by violanthrone dyes. Thus, solvent choice can be a parameter used to tailor aggregate structures to specific applications in photochemical technologies.

References

(1) Krummel, A. T.; Zanni, M. T. DNA Vibrational Coupling Revealed with Two-Dimensional Infrared Spectroscopy: Insight into Why Vibrational Spectroscopy Is Sensitive to DNA Structure. *J. Phys. Chem. B* **2006**, *110* (28), 13991–14000. https://doi.org/10.1021/jp062597w.

(2) Sanstead, P. J.; Tokmakoff, A. Direct Observation of Activated Kinetics and Downhill Dynamics in DNA Dehybridization. *J. Phys. Chem. B* **2018**, *122* (12), 3088–3100. https://doi.org/10.1021/acs.jpcb.8b01445.

(3) Ganim, Z.; Chung, H. S.; Smith, A. W.; DeFlores, L. P.; Jones, K. C.; Tokmakoff, A. Amide I Two-Dimensional Infrared Spectroscopy of Proteins. *Acc. Chem. Res.* **2008**, *41* (3), 432–441. https://doi.org/10.1021/ar700188n.

(4) Ghosh, A.; Ostrander, J. S.; Zanni, M. T. Watching Proteins Wiggle: Mapping Structures with Two-Dimensional Infrared Spectroscopy. *Chemical Reviews* **2017**, *117* (16), 10726–10759. https://doi.org/10.1021/acs.chemrev.6b00582.

(5) Mattson, M. A.; Green, T. D.; Lake, P. T.; McCullagh, M.; Krummel, A. T. Elucidating Structural Evolution of Perylene Diimide Aggregates Using Vibrational Spectroscopy and Molecular Dynamics Simulations. *The Journal of Physical Chemistry B* **2018**, *122* (18), 4891–4900. https://doi.org/10.1021/acs.jpcb.8b02355.

(6) Cyran, J. D.; Nite, J. M.; Krummel, A. T. Characterizing Anharmonic Vibrational Modes of Quinones with Two-Dimensional Infrared Spectroscopy. *J. Phys. Chem. B* **2015**, *119* (29), 8917–8925. https://doi.org/10.1021/jp506900n.

(7) Cyran, J. D.; Krummel, A. T. Probing Structural Features of Self-Assembled Violanthrone-79 Using Two Dimensional Infrared Spectroscopy. *The Journal of Chemical Physics* **2015**, *142* (21), 212435. https://doi.org/10.1063/1.4919637.

(8) Choi, H.; Paek, S.; Song, J.; Kim, C.; Cho, N.; Ko, J. Synthesis of Annulated Thiophene Perylene Bisimide Analogues: Their Applications to Bulk Heterojunction Organic Solar Cells. *Chem. Commun.* **2011**, *47* (19), 5509. https://doi.org/10.1039/c0cc05448h.

(9) Díaz-García, M. A.; Calzado, E. M.; Villalvilla, J. M.; Boj, P. G.; Quintana, J. A.; Céspedes-Guirao, F. J.; Fernández-Lázaro, F.; Sastre-Santos, Á. Effect of Structural Modifications in the Laser Properties of Polymer Films Doped with Perylenebisimide Derivatives. *Synthetic Metals* **2009**, *159* (21–22), 2293–2295. https://doi.org/10.1016/j.synthmet.2009.07.016.

(10) Schmidt-Mende, L. Self-Organized Discotic Liquid Crystals for High-Efficiency Organic Photovoltaics. *Science* **2001**, *293* (5532), 1119–1122. https://doi.org/10.1126/science.293.5532.1119.

(11) Shetty, A. S.; Zhang, J.; Moore, J. S. Aromatic π-Stacking in Solution as Revealed through the Aggregation of Phenylacetylene Macrocycles. *J. Am. Chem. Soc.* **1996**, *118* (5), 1019–1027. https://doi.org/10.1021/ja9528893.

(12) Martinez, C. R.; Iverson, B. L. Rethinking the Term "Pi-Stacking." *Chem. Sci.* **2012**, *3* (7), 2191. https://doi.org/10.1039/c2sc20045g.

(13) Waters, M. L. Aromatic Interactions in Model Systems. *Current Opinion in Chemical Biology* **2002**, *6* (6), 736–741. https://doi.org/10.1016/S1367-5931(02)00359-9.

(14) Shi, M.-M.; Chen, Y.; Nan, Y.-X.; Ling, J.; Zuo, L.-J.; Qiu, W.-M.; Wang, M.; Chen, H.-Z. Π−π Interaction among Violanthrone Molecules: Observation, Enhancement, and Resulting

Charge Transport Properties. *J. Phys. Chem. B* **2011**, *115* (4), 618–623. https://doi.org/10.1021/jp109683h.

(15) Peng, C. S.; Fedeles, B. I.; Singh, V.; Li, D.; Amariuta, T.; Essigmann, J. M.; Tokmakoff, A. Two-Dimensional IR Spectroscopy of the Anti-HIV Agent KP1212 Reveals Protonated and Neutral Tautomers That Influence PH-Dependent Mutagenicity. *Proc Natl Acad Sci USA* **2015**, *112* (11), 3229–3234. https://doi.org/10.1073/pnas.1415974112.

(16) Fayer, M. D.; Moilanen, D. E.; Wong, D.; Rosenfeld, D. E.; Fenn, E. E.; Park, S. Water Dynamics in Salt Solutions Studied with Ultrafast Two-Dimensional Infrared (2D IR) Vibrational Echo Spectroscopy. *Acc. Chem. Res.* **2009**, *42* (9), 1210–1219. https://doi.org/10.1021/ar900043h.

(17) Volkov, V.; Hamm, P. A Two-Dimensional Infrared Study of Localization, Structure, and Dynamics of a Dipeptide in Membrane Environment. *Biophysical Journal* **2004**, *87* (6), 4213–4225. https://doi.org/10.1529/biophysj.104.045435.

(18) Tan, H.-S.; Warren, W. S. Mid Infrared Pulse Shaping by Optical Parametric Amplification and Its Application to Optical Free Induction Decay Measurement. *Optics Express* **2003**, *11* (9), 1021. https://doi.org/10.1364/OE.11.001021.

(19) Kuhs, C.; Luther, B.; Krummel, A. Recent Advances in 2D IR Spectroscopy Driven by Advances in Ultrafast Technology. *IEEE Journal of Selected Topics in Quantum Electronics* **2019**, 1–1. https://doi.org/10.1109/JSTQE.2019.2900597.

(20) Shim, S.-H.; Zanni, M. T. How to Turn Your Pump–Probe Instrument into a Multidimensional Spectrometer: 2D IR and Vis Spectroscopies via Pulse Shaping. *Phys. Chem. Chem. Phys.* **2009**, *11* (5), 748–761. https://doi.org/10.1039/B813817F.

(21) Phillips, J. C.; Braun, R.; Wang, W.; Gumbart, J.; Tajkhorshid, E.; Villa, E.; Chipot, C.; Skeel, R. D.; Kalé, L.; Schulten, K. Scalable Molecular Dynamics with NAMD. *J. Comput. Chem.* **2005**, *26* (16), 1781–1802. https://doi.org/10.1002/jcc.20289.

(22) Wang, J.; Wolf, R. M.; Caldwell, J. W.; Kollman, P. A.; Case, D. A. Development and Testing of a General Amber Force Field. *J. Comput. Chem.* **2004**, *25* (9), 1157–1174. https://doi.org/10.1002/jcc.20035.

(23) Bayly, C. I.; Cieplak, P.; Cornell, W.; Kollman, P. A. A Well-Behaved Electrostatic Potential Based Method Using Charge Restraints for Deriving Atomic Charges: The RESP Model. *J. Phys. Chem.* **1993**, *97* (40), 10269–10280. https://doi.org/10.1021/j100142a004.

(24) Fox, T.; Kollman, P. A. Application of the RESP Methodology in the Parametrization of Organic Solvents. *J. Phys. Chem. B* **1998**, *102* (41), 8070–8079. https://doi.org/10.1021/jp9717655.

(25) Kumar, S.; Rosenberg, J. M.; Bouzida, D.; Swendsen, R. H.; Kollman, P. A. THE Weighted Histogram Analysis Method for Free-Energy Calculations on Biomolecules. I. The Method. *J. Comput. Chem.* **1992**, *13* (8), 1011–1021. https://doi.org/10.1002/jcc.540130812.

(26) Woutersen, S.; Mu, Y.; Stock, G.; Hamm, P. Subpicosecond Conformational Dynamics of Small Peptides Probed by Two-Dimensional Vibrational Spectroscopy. *Proceedings of the National Academy of Sciences* **2001**, *98* (20), 11254–11258. https://doi.org/10.1073/pnas.201169498.

Chapter 5

Conclusions and Future Work

5.1 Conclusions

The experimental work presented here is split into two parts, work done on the self-assembly of dipeptides and solvent effects on violanthrone-79 aggregates. This thesis shows that the primary structure of the dipeptide influences both intermolecular and intramolecular properties of dipeptide secondary, tertiary, and quaternary structure. This is first shown in chapter 2, where images of the different structures of the isomers Ile-Phe and Phe-Ile prepared in DMSO and D_2O show this differences in aggregation. A further example of this phenomenon comes in chapter 3 by examining Val-Phe and Phe-Val solvent properties.

Various spectroscopic properties where influenced by the intramolecular differences between Val-Phe and Phe-Val, such as the change in relative peak intensity between cross peaks and on diagonal peaks as a function of population time. These differences relate to the rate of hydrogen making/breaking dynamics of the amide I vibrational mode. The experiments presented here show that Val-Phe has slower hydrogen bond dynamics when compared to Phe-Val. These results support the results of MD simulations, which show a difference in the water environment around each dipeptide and differences in the water on/off rate that follow the same trends.

The next part of this thesis used MD simulations to demonstrate V-79 forms two different π-stacked aggregates, antiparallel and parallel. QM calculations of these different structures show a different distribution of vibrational frequencies, and the dimer with the greater amount of π stacking, antiparallel, has vibrational energy is more delocalized. 2D-IR experiments performed

on V-79 aggregates formed in THF and $HCCl_3$ also showed frequency and vibrational energy distribution differences. Aggregates formed in THF haver smaller distribution of vibrational frequencies in the carbonyl region and a greater degree of vibrational energy delocalization. From these results, it was hypothesized that aggregates formed in $HCCl_3$ are more antiparallel to adjacent units, while THF aggregates are parallel. Therefore, this work shows that differences in the solvent polarity effects the preferential stacking configurations.

5.2 Future work

From the work presented here, a variety of different research opportunities present themselves for both violanthrone-79 and dipeptide projects. First, consider the possibilities of V-79. This work hypothesizes that changes in solvent change the nature of the π stacking network in V-79 aggregates. This results in greater delocalization of vibrational energy though the molecule from the carbonyl mode into the ring modes. Further work would build on this hypothesis by first conducting population transfer experiments with V-79 in a non-polar solvent such as carbon tetrachloride (CCl_4). This solvent should provide the least support for π-stacking, resulting in slower population dynamics than aggregates formed in $HCCl_3$. In addition, doping in small amounts of D_2O into the CCl_4 system would test two different parameters. First, does D_2O form a preferential solvation cell around the aggregate and what amount of D_2O is necessary to disrupt the π-stacking network.

In addition, the end of chapter 2 reveals a difference in the Ile-Phe aggregate verses the Phe-Val aggregate. Performing 2D IR experiments on these two dipeptide systems would provide valuable information on both differences in the solvent dynamics that drive this variation in aggregation and inform on the structural differences. Preliminary work has shown that small amounts of salt disrupts the self-assemble of these two dipeptides, thereby allowing for a solution

based 2D-IR study. To gain information on the structural information, 8 frame phase cycling would have to be used to minimizing scattering artifacts in the data. The final phase of the dipeptide project would to examine the aggregate properties of diphenylalanine. Using the information gained from examining the Val and Ile dipeptide systems long side diphenylalanine experiments, future work would develop a complete model of dipeptide self-assembly.

Appendix I

MATLAB Programs

A1.1 MATLAB program for importanting and integrated peak for population transfer for V-79

Pop_transfer.m

```
%% population transfer of v79 Data Splines
clc
clear all clear
close all
%% Importing the Data
jj = 81;
% the "cd" command takes you to the directory where the data is
stored
cd 'C:\Users\Christopher\OneDrive - Colostate\V-79\2D Round
2\July 24 2018\Anisotropy\XXXX'
for k =1:jj
    % looping over the data files to inport them all into a
given data
    % variable
    FileName = ['v79_HCCl3_Anti_XXXX_0_ ' num2str(k) '_25_'];
    D = importdata(FileName);
    data_HCCl3_XX(:,:,k) = D(:,:);
end
jj = 81;
cd 'C:\Users\Christopher\OneDrive - Colostate\V-79\2D Round
2\July 24 2018\Anisotropy\XXYY'
for k =1:jj
    FileName = ['v79_HCCl3_Ani_XXYY_0_ ' num2str(k) '_25_'];
    D = importdata(FileName);
    data_HCCl3_XY(:,:,k) = D(:,:);
end
ii = 81;
cd 'C:\Users\Christopher\OneDrive - Colostate\V-79\2D Round
2\July 26 2018\Anisotropy\XXXX'
for i =1:ii
    FileName = ['v79_THF_Ani_XXXX_0_ ' num2str(i) '_25_'];
    D = importdata(FileName);
    data_THF_XX(:,:,i) = D(:,:);
end
kk = 81;
```

```
cd 'C:\Users\Christopher\OneDrive - Colostate\V-79\2D Round
2\July 26 2018\Anisotropy\XXYY'
for i =1:kk
    FileName = ['v79_THF_Ani_XXYY_0_ ' num2str(i) '_25_'];
    D = importdata(FileName);
    data_THF_XY(:,:,i) = D(:,:);
end
%% Defining the axie postions
 % Pump axis
fft_length = linspace(0,255, 256);
step_size = 25;
step_size = (step_size/1e15);
time_step = step_size *fft_length;
length_time_step = length(time_step);
delta_v = 1/(step_size*length_time_step);
% making the positive freq range
freq_pos = fft_length(:,2:((length_time_step/2)+1))*delta_v;
freq_neg = -1*fft_length(:,2:((length_time_step/2)))*delta_v;
zero = 0;
%
pump_freq = [fliplr(freq_neg), zero,freq_pos];
pump_freq = (1./((1./pump_freq)*299792458*100))+1327;
y_pump = pump_freq(:,165:200);

% pulling in the calibration file
cd 'C:\Users\Christopher\OneDrive - Colostate\V-79\2D Round
2\July 24 2018\Calibration'
prob = importdata('6200_6micron_probe_axis_cal.txt');
probe = (10000000./prob);
x_probe =  fliplr(probe(:,9:39)-35);
%%
probe_splined_axis = linspace(x_probe(1,1), x_probe(1,31), 100);
pump_splined_axis  = linspace(y_pump(1,1), y_pump(1,36), 100);
HCCl3_pump  = probe_splined_axis - 3;
HCCl3_probe = pump_splined_axis - 3;

THF_probe = probe_splined_axis;
THF_pump = pump_splined_axis;

%% Doing the phase math
% The data file comes out in 4 parts for the four phase cycles.
here we
% just break that apart and do the subtraction
for i = (1:81)
    raw_HCCl3_XX(:,:,i) = ((data_HCCl3_XX(1:64,:,i) -
data_HCCl3_XX(65:128,:,i))...
```

```
        + (data_HCCl3_XX(129:192,:,i) -
data_HCCl3_XX(193:256,:,i)));

    raw_HCCl3_XY(:,:,i) = ((data_HCCl3_XY(1:64,:,i) -
data_HCCl3_XY(65:128,:,i))...
        + (data_HCCl3_XY(129:192,:,i) -
data_HCCl3_XY(193:256,:,i)));


    raw_THF_XX(:,:,i) = ((data_THF_XX(1:64,:,i) -
data_THF_XX(65:128,:,i)) + (data_THF_XX(129:192,:,i)...
        - data_THF_XX(193:256,:,i)));


    raw_THF_XY(:,:,i) = ((data_THF_XY(1:64,:,i) -
data_THF_XY(65:128,:,i)) + (data_THF_XY(129:192,:,i)...
        - data_THF_XY(193:256,:,i)));
end
%% making an array of zeros that get placed at the end of the
data set for
% zeropadding the data for FFTS
padsize       = 256;
padsize       = padsize - length(raw_THF_XY(1,:,1));
pad  = zeros(64,padsize,81);
%% apply the pads
f_HCCl3_XX = [raw_HCCl3_XX,pad];
f_HCCl3_XY = [raw_HCCl3_XY,pad];
f_THF_XX   = [raw_THF_XX,pad];
f_THF_XY   = [raw_THF_XY,pad];
%% apllying a window function to reduce the noie in the FID of
the data set
window =  hamming(180,'symmetric');
window2 = [window(90:180)',zeros(1,10)];
%% Multiplying the FID with the window function to applying it
to the data set
for j = 1:81
    for k = 1:64
        windowed_HCCl3_XX(k,:,j) =
raw_HCCl3_XX(k,:,j);%.*window2;
        windowed_HCCl3_XY(k,:,j) =
raw_HCCl3_XY(k,:,j);%.*window2;
        windowed_THF_XX(k,:,j) = raw_THF_XX(k,:,j);%.*window2;
        windowed_THF_XY(k,:,j) = raw_THF_XY(k,:,j);%.*window2;
    end
end
%%
% for j = 1:81
```

```
%     for k = 1:64
%         windowed_HCCl3_XX(k,:,j) =
raw_HCCl3_XX(k,:,j).*window2;
%         windowed_HCCl3_XY(k,:,j) =
raw_HCCl3_XY(k,:,j).*window2;
%         windowed_THF_XX(k,:,j) = raw_THF_XX(k,:,j).*window2;
%         windowed_THF_XY(k,:,j) = raw_THF_XY(k,:,j).*window2;
%     end
% end
%%
figure()
hold on
plot(raw_THF_XX(38,:,22))
plot(windowed_THF_XX(38,:,22))
hold off

%% with window
f_HCCl3_XX = [windowed_HCCl3_XX,pad];
f_HCCl3_XY = [windowed_HCCl3_XY,pad];
f_THF_XX   = [windowed_THF_XX,pad];
f_THF_XY   = [windowed_THF_XY,pad];
%

%% Taking the FFTs
for j = (1:81)
    for i = (1:64)
        tempft_HCCl3_XX(i,:,j) = -
1*(fftshift(fft((f_HCCl3_XX(i,:,j)))));
    end
    ft_HCCl3_XX(:,:,j) = tempft_HCCl3_XX(20:50,165:200,j);
end
for j = 1:81
    for i = 1:64
    temp_HCCl3_XY(i,:,j) = -
1*(fftshift(fft((f_HCCl3_XY(i,:,j)))));
    end
    ft_HCCl3_XY(:,:,j) = temp_HCCl3_XY(20:50,165:200,j);
end

for j = 1:81
    for i = 1:64
    temp_THF_XY(i,:,j)   = -
1*(fftshift(fft((f_THF_XY(i,:,j)))));
    end
    ft_THF_XY(:,:,j)   = temp_THF_XY(20:50,165:200,j);
end
for j = 1:81
```

```
    for i = 1:64
        temp_THF_XX(i,:,j)   = -
1*(fftshift(fft((f_THF_XX(i,:,j)))));
    end
   ft_THF_XX(:,:,j)   = temp_THF_XX(20:50,165:200,j);
end
%% prepating the data to integrated
x = linspace(1,31,31);
dx = linspace(1,31,100);
y = linspace(1,36,36);
dy = linspace(1,36,100);
%% XX HCCl3 Data
for j = 1:81
    for k = 1:31
        slpine_HCCl3_XX(k,:,j) =
spline(y,real(ft_HCCl3_XX(k,:,j)),dy);
    end
end
for j = 1:81
    for i = 1:100
        full_slpine_HCCl3_XX(:,i,j) =
spline(x,slpine_HCCl3_XX(:,i,j),dx);
    end
end
%% XX THF Data
for j = 1:81
    for k = 1:31
        slpine_THF_XX(k,:,j) =
spline(y,real(ft_THF_XX(k,:,j)),dy);
    end
end
%%
for j = 1:81
    for i = 1:100
        full_slpine_THF_XX(:,i,j) =
spline(x,slpine_THF_XX(:,i,j),dx);
    end
end
%% XY HCCl3 Data
for j = 1:81
    for k = 1:31
        slpine_HCCl3_XY(k,:,j) =
spline(y,real(ft_HCCl3_XY(k,:,j)),dy);
    end
end
for j = 1:81
    for i = 1:100
```

```
        full_slpine_HCCl3_XY(:,i,j) =
spline(x,slpine_HCCl3_XY(:,i,j),dx);
    end
end

%% XX THF Data
for j = 1:81
    for k = 1:31
        slpine_THF_XY(k,:,j) =
spline(y,real(ft_THF_XY(k,:,j)),dy);
    end
end
for j = 1:81
    for i = 1:100
        full_slpine_THF_XY(:,i,j) =
spline(x,slpine_THF_XY(:,i,j),dx);
    end
end
%%
test_test.coefs = slpine_THF_XY(:,:,1)
%% Calculated the magic angle spectra
for j = 1:81
    magic_THF(:,:,j)   = (full_slpine_THF_XX(:,:,j) -
full_slpine_THF_XY(:,:,j))./(full_slpine_THF_XX(:,:,j) +
2*full_slpine_THF_XY(:,:,j));
    magic_HCCl3(:,:,j) = (full_slpine_HCCl3_XX(:,:,j) -
full_slpine_HCCl3_XY(:,:,j))./(full_slpine_HCCl3_XX(:,:,j) +
2*full_slpine_HCCl3_XY(:,:,j));
end
%% Plotting the 2D data of THF
for j = (51:51)
    axes1 = axes('Parent',figure());
    hold(axes1,'on');
    contourf(x_probe, THF_pump,(-
1*slpine_THF_XX(:,:,j)./min(min(slpine_THF_XX(:,:,j))))',
[linspace(-1, -0.05, 10), linspace(0.08, 1, 10)]);
    %contourf((-
1*full_slpine_THF_XX(:,:,j)./min(min(full_slpine_THF_XX(:,:,j)))
)', [linspace(-1, -0.05, 15), linspace(0.08, 1, 15)]);
    %plot(pump_splined_axis,pump_splined_axis,'k')

set(axes1,'FontSize',12,'XMinorTick','on','YMinorTick','on');
    colorbar;
    hold off
    title(['Sub v79 THF XXXX  ',sprintf('%d',j)])
    xlabel('w probe (cm^-^1)');
    ylabel('w pump (cm^-^1)');
```

```
%     savefig(['VF Spectra ' num2str(j) ' with XXXX'])
%     saveas(figure(j), ['VF Spectra ' num2str(j) ' with
XXXX.png'])
end
%% Plotting the 2D data of HCCl3
for j = (31:31)
    axes1 = axes('Parent',figure());
    hold(axes1,'on');
    contourf(HCCl3_pump, HCCl3_probe,(-
1*full_slpine_HCCl3_XX(:,:,j)./min(min(full_slpine_HCCl3_XX(:,:,
j))))', [linspace(-1, -0.05, 5), linspace(0.08, 1, 5)]);
%     contourf((-
1*full_slpine_HCCl3_XX(:,:,j)./min(min(full_slpine_HCCl3_XX(:,:,
j))))', [linspace(-1, -0.05, 15), linspace(0.08, 1, 15)]);
    %plot(pump_splined_axis,pump_splined_axis,'k')

set(axes1,'FontSize',12,'XMinorTick','on','YMinorTick','on');
    colorbar;
    hold off
    title(['Sub v79 HCCl3 XXXX  ',sprintf('%d',j)])
    xlabel('w probe (cm^-^1)');
    ylabel('w pump (cm^-^1)');
%     savefig(['VF Spectra ' num2str(j) ' with XXXX'])
%     saveas(figure(j), ['VF Spectra ' num2str(j) ' with
XXXX.png'])
end
%% Defining the integration boxes in the data sets and
generating an array
%  of these sumations for the different time steps.
for j = 1:81
THF_XX_A(:,j)     = sum(sum(full_slpine_THF_XX(60:63,64:74,j)));
THF_XX_B(:,j)     = sum(sum(full_slpine_THF_XX(24:26,67:74,j)));
THF_magic_A(:,j)  = sum(sum(magic_THF(60:63,64:74,j)));
THF_magic_B(:,j)  = sum(sum(magic_THF(24:26,67:74,j)));

HCCl3_XX_A(:,j)   =
sum(sum(full_slpine_HCCl3_XX(57:62,65:75,j)));
HCCl3_XX_B(:,j)   =
sum(sum(full_slpine_HCCl3_XX(23:26,63:74,j)));
HCCl3_magic_A(:,j)= sum(sum(magic_HCCl3(57:62,65:75,j)));
HCCl3_magic_B(:,j)= sum(sum(magic_HCCl3(23:26,63:74,j)));

THF_XY_A(:,j) = sum(sum(full_slpine_THF_XY(60:63,64:74,j)));
THF_XY_B(:,j) = sum(sum(full_slpine_THF_XY(24:26,67:74,j)));

HCCl3_XY_A(:,j) = sum(sum(full_slpine_HCCl3_XY(57:62,65:75,j)));
HCCl3_XY_B(:,j) = sum(sum(full_slpine_HCCl3_XY(23:26,63:74,j)));
```

```
end

%%
% for j = 1:81
% THF_XX_A(:,j) = min(min(full_slpine_THF_XX(60:63,66:72,j)));
% %THF_XX_A(:,j) = min(min(full_slpine_THF_XX(60:63,64:74,j)));
% THF_XX_B(:,j) = min(min(full_slpine_THF_XX(24:26,67:72,j)));
%
% HCCl3_XX_A(:,j) =
min(min(full_slpine_HCCl3_XX(57:62,65:75,j)));
% HCCl3_XX_B(:,j) =
min(min(full_slpine_HCCl3_XX(23:26,63:74,j)));
%
% THF_XY_A(:,j) = min(min(full_slpine_THF_XY(60:63,66:72,j)));
% %THF_XY_A(:,j) = min(min(full_slpine_THF_XY(60:63,64:74,j)));
% THF_XY_B(:,j) = min(min(full_slpine_THF_XY(24:26,67:72,j)));
%
% HCCl3_XY_A(:,j) =
min(min(full_slpine_HCCl3_XY(57:62,65:75,j)));
% HCCl3_XY_B(:,j) =
min(min(full_slpine_HCCl3_XY(23:26,63:74,j)));

% magic_min_THF_A(:,j)  = THF_XX_A(:,j)+2.*THF_XY_A(:,j);
% magic_min_THF_B(:,j)  = THF_XX_B(:,j)+2.*THF_XY_B(:,j);
% magic_min_HCCl3_A(:,j)= HCCl3_XX_A(:,j)+2.*HCCl3_XY_A(:,j);
% magic_min_HCCl3_B(:,j)= HCCl3_XX_B(:,j)+2.*HCCl3_XY_B(:,j);
% end
% %%
% for j = 1:81
% ratio_THF_XX(:,j) = movmean((THF_XX_B(:,j)./THF_XX_A(:,j)),3);
% ratio_THF_XY(:,j) = movmean((THF_XY_B(:,j)./THF_XY_A(:,j)),3);
% ratio_HCCl3_XX(:,j) =
movmean((HCCl3_XX_B(:,j)./HCCl3_XX_A(:,j)),3);
% ratio_HCCl3_XY(:,j) =
movmean((HCCl3_XY_B(:,j)./HCCl3_XY_A(:,j)),3);
% end
%%  Defining the ratio between the cross peak and the on
diagonal peak
ratio_THF_XX(:,:) = -
1.*movmean((THF_XX_B(:,:)./THF_XX_A(:,:)),1);
ratio_THF_XY(:,:) = -
1.*movmean((THF_XY_B(:,:)./THF_XY_A(:,:)),1);
ratio_HCCl3_XX(:,:) = -
1.*movmean((HCCl3_XX_B(:,:)./HCCl3_XX_A(:,:)),1);
ratio_HCCl3_XY(:,:) = -
1.*movmean((HCCl3_XY_B(:,:)./HCCl3_XY_A(:,:)),1);
```

```
%%
% magic_ratio_THF_sum(:,:)   = magic_sum_THF_B./magic_sum_THF_A;
% magic_ratio_HCCl3_sum(:,:) =
magic_sum_HCCl3_B./magic_sum_HCCl3_A
%
% magic_ratio_THF_min(:,:)   = magic_min_THF_B./magic_min_THF_A
% magic_ratio_HCCl3_min(:,:) =
magic_min_HCCl3_B./magic_min_HCCl3_A
%% Defining the Time axis for the plots
 time = linspace(0, 8000, 81);
%% ploting the ratios between the cross peak and the on diagonal
peak
figure()
hold on
plot(time, ratio_THF_XX,'k')
plot(time, ratio_THF_XY,'b')
title('THF')
hold off

figure()
hold on
plot(time, ratio_HCCl3_XX,'k')
plot(time, ratio_HCCl3_XY,'b')
title('HCCl3')
hold off
%%
aaa = (ratio_THF_XX - ratio_THF_XY)./(ratio_THF_XX +
2*ratio_THF_XY);
bbb = (ratio_HCCl3_XX - ratio_HCCl3_XY)./(ratio_HCCl3_XX +
2*ratio_HCCl3_XY);
figure()
hold on
plot(time, aaa,'k')
title('THF')
hold off


figure()
hold on
plot(time, bbb,'k')
title('HCCl3')
hold off
%% plotting the magic

figure()
hold on
%scatter(time, magic_ratio_THF_sum)
```

```
scatter(time, (magic_ratio_THF_min))
title('THF')
hold off

figure()
hold on
scatter(time, (magic_ratio_HCCl3_sum))
title('HCCl3')
hold off
%%
test_THF = log(magic_ratio_THF_min)
%%
part_magic_THF = [time',  magic_ratio_THF_sum'];
%%
part_magic_HCCl3 = [time',  magic_ratio_HCCl3_sum'];
%%
figure()
scatter(part_magic_THF(:,1), part_magic_THF(:,2))
magic_temp_x = part_magic_THF(:,1)
magic_temp_y = part_magic_THF(:,2)
%%
figure()
scatter(part_magic_HCCl3(:,1), part_magic_HCCl3(:,2));
magic_temp_x_HCCl3 = part_magic_HCCl3(:,1);
magic_temp_y_HCCl3 = part_magic_HCCl3(:,2);
%% Magix angle

% for j = 1:80
%     magic_THF(:,:,j)   = full_slpine_THF_XX(:,:,j) +
2*full_slpine_THF_XY(:,:,j)
%     magic_HCCl3(:,:,j) = full_slpine_HCCl3_XX(:,:,j) +
2*full_slpine_HCCl3_XY(:,:,j)
% end

%% Magic Ratios
for j = 1:81
    ratio_magic_THF(:,j)   = THF_magic_B(:,j)./THF_magic_A(:,j);
    ratio_magic_HCCl3(:,j) =
HCCl3_magic_B(:,j)./HCCl3_magic_A(:,j);
end
```

A.1.2 MATLAB program for Calculating the Chemical Exchange for VF and FV

VF_FV_exhange.m

```
%% Looking at the chemical exchange of VF and FV using splined
data
clc
clear all clear
close all
%%
time = linspace(0, 3900, 40);
%% Number of data sets
jj = 44;
%% Importing the XXXX data
cd 'C:\Users\Christopher\OneDrive - Colostate\Dipeptide\2D Round
2\Aug 7 2018\VF\Full\XXXX'
for k =1:jj
    FileName = ['FV_pi_shift_0_ ' num2str(k) '_25_'];
    D = importdata(FileName);
    data(:,:,k) = D(:,:);
end
%% Importing the XXYY data
cd 'C:\Users\Christopher\OneDrive - Colostate\Dipeptide\2D Round
2\Aug 7 2018\VF\Full\XXYY'
for k =1:jj
    FileName = ['VF_XXYY_0_ ' num2str(k) '_25_'];
    D = importdata(FileName);
    data_XXYY(:,:,k) = D(:,:);
end
%% doing the pahse math
 f_raw = zeros(64,101,jj);
 f_raw_XXYY = zeros(64,101,jj);
for i = (1:jj)
    f_raw(:,:,i) = ((data(1:64,:,i) - data(65:128,:,i)) +
(data(129:192,:,i)...
        - data(193:256,:,i)));
    f_raw_XXYY(:,:,i) = ((data_XXYY(1:64,:,i) -
data_XXYY(65:128,:,i))...
        + (data_XXYY(129:192,:,i) - data_XXYY(193:256,:,i)));
end
%%
window = hann(180,'symmetric');
window2 = [window(90:180)',zeros(1,10)];
%%
for j = 1:jj
    for k = 1:64
        windowed_f_raw(k,:,j)      =  f_raw(k,:,j).*window2;
        windowed_f_raw_XXYY(k,:,j) = f_raw_XXYY(k,:,j).*window2;
    end
end
%%
```

```
padsize = 512;
padsize = padsize - length(data(1,:,1));
pad = zeros(64,padsize,jj);
f = [windowed_f_raw,pad];
f_XXYY = [windowed_f_raw_XXYY,pad];
%% taking the FFT of the data
ftdata = zeros(64, 512, jj);
ftdata_XXYY = zeros(64, 512, jj);
% ftplot = zeros(27, 71, jj);
% ftplot_XXYY = zeros(27, 71, jj);
%% normalizing the FID
for j = (1:jj)
    for i = (1:64)
        cc = 1e6;
        temp_f(i,:,j) = f(i,:,j);
        temp_XXYY(i,:,j) = f_XXYY(i,:,j)./f_XXYY(i,1,j);
    end
end
%%
figure()
plot(temp_f(32,:,1))
%%
%f(:,:,:) = temp(i,:,j);

%%
for j = (1:jj)
    for i = (1:64)
        ftdata(i,:,j) = -1*(fftshift(fft((temp_f(i,:,j)))));
        ftdata_XXYY(i,:,j) = -
1*(fftshift(fft((f_XXYY(i,:,j)))));
    end
    VF_ftplot(:,:,j) = ftdata(9:39,345:405,j);
    VF_ftplot_XXYY(:,:,j) = ftdata_XXYY(9:39,345:405,j);
end
%% clearing some variables
clear data data_XXYY f_raw f_raw_XXYY pad f f_XXYY ftdata
ftdata_XXYY ftdata ftdata_XXYY

%% Importing the FV data
jjj = 40;
%% Importing the XXXX data
cd 'C:\Users\Christopher\OneDrive - Colostate\Dipeptide\2D Round
2\Aug 7 2018\FV\Full\XXXX R2'
for k =1:jjj
    FileName = ['FV_Full_XXXX_0_ ' num2str(k) '_25_'];
    D = importdata(FileName);
    data(:,:,k) = D(:,:);
```

```
end
%% Importing the XXYY data
cd 'C:\Users\Christopher\OneDrive - Colostate\Dipeptide\2D Round
2\Aug 7 2018\FV\Full\XXYY'
for k =1:jjj
    FileName = ['FV_Full_XXYY_0_ ' num2str(k) '_25_'];
    D = importdata(FileName);
    data_XXYY(:,:,k) = D(:,:);
end
%%
 f_raw = zeros(64,101,jjj);
 f_raw_XXYY = zeros(64,101,jjj);
for i = (1:jjj)
    f_raw(:,:,i) = ((data(1:64,:,i) - data(65:128,:,i)) +
(data(129:192,:,i)...
        - data(193:256,:,i)));
    f_raw_XXYY(:,:,i) = ((data_XXYY(1:64,:,i) -
data_XXYY(65:128,:,i))...
        + (data_XXYY(129:192,:,i) - data_XXYY(193:256,:,i)));
end
%%
for j = 1:40
    for k = 1:64
        windowed_f_raw(k,:,j)      = f_raw(k,:,j).*window2;
        windowed_f_raw_XXYY(k,:,j) = f_raw_XXYY(k,:,j).*window2;
    end
end
%%
figure()
hold on
plot(windowed_f_raw(33,:,1))
plot(f_raw(33,:,1))
hold off

%%
padsize = 512;
padsize = padsize - length(data(1,:,1));
pad = zeros(64,padsize,jj);
f = [windowed_f_raw,pad];
f_XXYY = [windowed_f_raw_XXYY,pad];

%% normalizing the FID
for j = (1:jj)
    for i = (1:64)
        cc = 1e6;
        temp_f(i,:,j) = f(i,:,j)./cc;
        temp_XXYY(i,:,j) = f_XXYY(i,:,j)./f_XXYY(i,1,j);
```

```
    end
end


%% taking the FFT of the data
ftdata = zeros(64, 512, jjj);
ftdata_XXYY = zeros(64, 512, jjj);
% ftplot = zeros(27, 71, jj);
% ftplot_XXYY = zeros(27, 71, jj);
for j = (1:jjj)
    for i = (1:64)
        ftdata(i,:,j) = -1*(fftshift(fft((f(i,:,j)))));
        ftdata_XXYY(i,:,j) = -
1*(fftshift(fft((f_XXYY(i,:,j)))));
    end
    fv_ftplot(:,:,j) = ftdata(9:39,345:405,j);
    fv_ftplot_XXYY(:,:,j) = ftdata_XXYY(9:39,345:405,j);
end
%% Defing the magic angle spectra
fv_magic = fv_ftplot +2.*fv_ftplot_XXYY;
vf_magic = VF_ftplot +2.*VF_ftplot_XXYY;
%% Conducting the splines
% Defingin the number of points to smooth the data over
x_s = linspace(1,31,31);
y_s = linspace(1,61,61);

xx_s = linspace(1,31,100);
yy_s = linspace(1,61,100);

for j = 1:40
    for i = 1:61
        fv_spline(:,i,j) =
spline(x_s,real(fv_magic(:,i,j)),xx_s);
        vf_spline(:,i,j) =
spline(x_s,real(vf_magic(:,i,j)),xx_s);

        fv_xx(:,i,j) = spline(x_s,real(fv_ftplot(:,i,j)),xx_s);
        fv_xy(:,i,j) =
spline(x_s,real(fv_ftplot_XXYY(:,i,j)),xx_s);
        vf_xx(:,i,j) = spline(x_s,real(VF_ftplot(:,i,j)),xx_s);
        vf_xy(:,i,j) =
spline(x_s,real(VF_ftplot_XXYY(:,i,j)),xx_s);
    end
end
for j = 1:40
    for i = 1:100
```

```
        fv_full_spline(i,:,j) =
spline(y_s,real(fv_spline(i,:,j)),yy_s);
        vf_full_spline(i,:,j) =
spline(y_s,real(vf_spline(i,:,j)),yy_s);

        fv_xx_full_spline(i,:,j) =
spline(y_s,(fv_xx(i,:,j)),yy_s);
        fv_xy_full_spline(i,:,j) =
spline(y_s,(fv_xy(i,:,j)),yy_s);
        vf_xx_full_spline(i,:,j) =
spline(y_s,(vf_xx(i,:,j)),yy_s);
        vf_xy_full_spline(i,:,j) =
spline(y_s,(vf_xy(i,:,j)),yy_s);
    end
end
%% pulling in the calibration file
% cd 'C:\Users\Christopher\OneDrive - Colostate\Dipeptide\2D
Round 2\Aug 7 2018\FV\Calibration'
% prob = importdata('calibration8');
% %prob = importdata('6200_6micron_probe_axis.txt');
% probe = (10000000./prob);
% x = fliplr( probe(:,9:39));
%%
%%
center = 6000;
res = 21.92;
multi = -1*res;
pix = 64;
off_set = center + 0.90*res*(pix/2-1)
neg_off_set = center - 0.1*res*(pix/2-1)
for i = 1:32
    pos_probe(:,i) = off_set + multi*(i-1);
    neg_probe(:,i) = neg_off_set - multi*(i-1);
end
probe_test = 10000000./[pos_probe(:,2:32),
fliplr(neg_probe(:,1:31))];
probe_test2 = probe_test(:,1:31);
probe_test3 =
[0.98*probe_test2(:,1:15),1.006*probe_test2(:,16:31)]+10;

 %% pulling in the axis
 % Pump axis
fft_length = linspace(0,511, 512);
step_size = 25;
step_size = (step_size/1e15);
time_step = step_size *fft_length;
length_time_step = length(time_step);
```

```
delta_v = 1/(step_size*length_time_step);
% making the positive freq range
freq_pos = fft_length(:,2:((length_time_step/2))+2)*delta_v;
%freq_pos = fft_length(:,2:((length_time_step/2)+1))*delta_v;
freq_neg = -1*fft_length(:,2:((length_time_step/2))+2)*delta_v;
zero = 0;
%
pump_freq = [fliplr(freq_neg), zero,freq_pos];
pump_freq = (1./((1./pump_freq)*299792458*100))+1330;
y = pump_freq(:,345:405);
y2 = [y(:,1:30),y(:,31:61)];
%y2 = [0.9*y(:,1:30),1.004*y(:,31:61)];
% % pulling in the calibration file
% cd 'C:\Users\Christopher\OneDrive - Colostate\Dipeptide\2D
Round 2\Aug 7 2018\FV\Calibration'
% prob = importdata('calibration');
% %prob = importdata('6200_6micron_probe_axis.txt');
% probe = (10000000./prob);
% x = fliplr( probe(:,9:39));


%% spline the calibrated axis
probe_splined_axis = linspace(probe_test3(1,1),
probe_test3(1,31), 100);
%probe_splined_axis2 =
[probe_splined_axis(1:499),1.009*probe_splined_axis(500:1000)];
pump_splined_axis  = linspace(y2(1,1), y2(1,61), 100);
pump_splined_axis2 =
[0.999*pump_splined_axis(1:49),2+pump_splined_axis(50:100)];
vf_probe = probe_splined_axis;
vf_pump = pump_splined_axis2;
fv_probe = probe_splined_axis;
fv_pump =  pump_splined_axis2;
%%
for j = (3:4)
    axes1 = axes('Parent',figure());
    hold(axes1,'on');
    %contourf(vf_probe,vf_pump,(-
1*(vf_full_spline(:,:,j))./min(min(vf_full_spline(:,:,j))))',
[linspace(-1, -0.05, 15), linspace(0.08, 0.8, 15)]);
    contourf((-
1*(vf_full_spline(:,:,j))./min(min(vf_full_spline(:,:,j))))',
[linspace(-1, -0.05, 15), linspace(0.08, 0.8, 15)]);

set(axes1,'FontSize',12,'XMinorTick','on','YMinorTick','on');
    %plot(vf_probe,vf_probe,'k')
    colorbar;
```

```
    hold off
    title(['vf XXXX ',sprintf('%d',j)])
    xlabel('w probe (cm^-^1)');
    ylabel('w pump (cm^-^1)');
%     savefig(['VF Spectra ' num2str(j) ' with XXXX'])
%     saveas(figure(j), ['VF Spectra ' num2str(j) ' with
XXXX.png'])
end
%%
for j = (3:3)
    axes1 = axes('Parent',figure());
    hold(axes1,'on');
    contourf((-
1*(fv_full_spline(:,:,j))./min(min(fv_full_spline(:,:,j))))',
[linspace(-1, -0.05, 15), linspace(0.08, 0.8, 15)]);
    %contourf(fv_probe+3, fv_pump+2,(-
1*(fv_full_spline(:,:,j))./min(min(fv_full_spline(:,:,j))))',
[linspace(-1, -0.05, 15), linspace(0.08, 0.8, 15)]);

set(axes1,'FontSize',12,'XMinorTick','on','YMinorTick','on');
    %plot(fv_probe,fv_probe,'k')
    colorbar;
    hold off
    title(['fv XXXX ',sprintf('%d',j)])
    xlabel('w probe (cm^-^1)');
    ylabel('w pump (cm^-^1)');
%     savefig(['VF Spectra ' num2str(j) ' with XXXX'])
%     saveas(figure(j), ['VF Spectra ' num2str(j) ' with
XXXX.png'])
end
%% Defining boxs for fv

for j = 1:40
    % for the amide group
    fv_A(:,:,j)  = fv_full_spline(72:76,59:63,j);
    fv_B(:,:,j)  = fv_full_spline(78:84,66:72,j);
    fv_AB(:,:,j) = fv_full_spline(78:84,59:63,j);

    fv_xx_B(:,:,j)  = fv_xx_full_spline(78:84,66:72,j);
    fv_xy_B(:,:,j)  = fv_xy_full_spline(78:84,66:72,j);
    % for the carboxal group
    fv_a(:,:,j)  = fv_full_spline(39:43,16:20,j);
    fv_b(:,:,j)  = fv_full_spline(42:46,21:25,j);
    fv_c(:,:,j)  = fv_full_spline(49:53,30:34,j);
    fv_ab(:,:,j) = fv_full_spline(42:46,16:20,j);
    fv_bc(:,:,j) = fv_full_spline(49:53,21:25,j);
    fv_ac(:,:,j) = fv_full_spline(49:53,16:20,j);
```

```
end
%% min
for j = 1:40
    min_fv_A(:,j)  = min(min(fv_A(:,:,j)));
    min_fv_B(:,j)  = min(min(fv_B(:,:,j)));
    min_fv_AB(:,j) = min(min(fv_AB(:,:,j)));

    min_fv_xx(:,j) = min(min(fv_xx_B(:,:,j)));
    min_fv_xy(:,j) = min(min(fv_xy_B(:,:,j)));
end
%% sum
for j = 1:40
    sum_fv_A(:,j)  = sum(sum(fv_A(:,:,j)));
    sum_fv_B(:,j)  = sum(sum(fv_B(:,:,j)));
    sum_fv_AB(:,j) = sum(sum(fv_AB(:,:,j)));

    sum_fv_xx(:,j) = sum(sum(fv_xx_B(:,:,j)));
    sum_fv_xy(:,j) = sum(sum(fv_xy_B(:,:,j)));
    % for the carbox groups
    carbox_sum_fv_a(:,j)  = sum(sum(fv_a(:,:,j)));
    carbox_sum_fv_b(:,j)  = sum(sum(fv_b(:,:,j)));
    carbox_sum_fv_c(:,j)  = sum(sum(fv_c(:,:,j)));
    carbox_sum_fv_ab(:,j) = sum(sum(fv_ab(:,:,j)));
    carbox_sum_fv_bc(:,j) = sum(sum(fv_bc(:,:,j)));
    carbox_sum_fv_ac(:,j) = sum(sum(fv_ac(:,:,j)));
end

%%
time = linspace(0, 3900, 40);
%%
figure()
hold on
plot(time, min_fv_A)
title('fv_A')
hold off


figure()
hold on
plot(time, min_fv_B)
title('fv_B')
hold off


figure()
hold on
plot(time, min_fv_AB)
```

```
title('fv_AB')
hold off
%%
figure()
hold on
plot(sum_fv_xx)
plot(sum_fv_xy)
hold off
%% Defining the boxes for vf


for j = 1:40
    % for the amide group
    vf_A(:,:,j)  = vf_full_spline(73:77,59:63,j);
    vf_B(:,:,j)  = vf_full_spline(78:84,66:72,j);
    vf_AB(:,:,j) = vf_full_spline(78:84,59:63,j);

    vf_xx_B(:,:,j)  = vf_xx_full_spline(78:84,66:72,j);
    vf_xy_B(:,:,j)  = vf_xy_full_spline(78:84,66:72,j);

    % for the carbox group
    vf_a(:,:,j)  = vf_full_spline(42:46,19:23,j);
    vf_b(:,:,j)  = vf_full_spline(46:50,26:30,j);
    vf_c(:,:,j)  = vf_full_spline(50:54,30:34,j);
    vf_ab(:,:,j) = vf_full_spline(46:50,19:23,j);
    vf_bc(:,:,j) = vf_full_spline(50:54,26:30,j);
    vf_ac(:,:,j) = vf_full_spline(50:54,19:23,j);
end
%% min
for j = 1:40
    min_vf_A(:,j)  = min(min(vf_A(:,:,j)));
    min_vf_B(:,j)  = min(min(vf_B(:,:,j)));
    min_vf_AB(:,j) = min(min(vf_AB(:,:,j)));

    min_vf_xx(:,j) = min(min(vf_xx_B(:,:,j)));
    min_vf_xy(:,j) = min(min(vf_xy_B(:,:,j)));
end
%% sum
for j = 1:40
    sum_vf_A(:,j)  = sum(sum(vf_A(:,:,j)));
    sum_vf_B(:,j)  = sum(sum(vf_B(:,:,j)));
    sum_vf_AB(:,j) = sum(sum(vf_AB(:,:,j)));

    sum_vf_xx(:,j) = sum(sum(vf_xx_B(:,:,j)));
    sum_vf_xy(:,j) = sum(sum(vf_xy_B(:,:,j)));
    % for the carbox group
    carbox_sum_vf_a(:,j)  = sum(sum(vf_a(:,:,j)));
```

```
    carbox_sum_vf_b(:,j)  = sum(sum(vf_b(:,:,j)));
    carbox_sum_vf_c(:,j)  = sum(sum(vf_c(:,:,j)));
    carbox_sum_vf_ab(:,j) = sum(sum(vf_ab(:,:,j)));
    carbox_sum_vf_bc(:,j) = sum(sum(vf_bc(:,:,j)));
    carbox_sum_vf_ac(:,j) = sum(sum(vf_ac(:,:,j)));
end
%% Looking at taking the ratios
vf_ratio = sum_vf_AB./sum_vf_B;
fv_ratio = sum_fv_AB./sum_fv_B;
%%
figure()
hold on
plot(time, vf_ratio)
title('vf ratio')
hold off
%%
figure()
hold on
plot(time, fv_ratio)
title('fv ratio')
hold off
%%
figure()
hold on
%plot(sum_vf_xx)
plot(sum_vf_xy)
hold off
%% Getting the fits in the plots

% fv_A_fit  = -5.572e+08*exp(-0.004278*time);
% fv_B_fit  = -2.284e+09*exp(-0.001144*time);
% fv_AB_fit = -6.217e+08 *exp(-0.0006695*time);
%
% vf_A_fit  = -3.351e+08*exp(-0.001721*time);
% vf_B_fit  = -1.242e+09 *exp(-0.0009929*time);
% vf_AB_fit = -4.781e+08*exp(-0.0007989*time);
%% Getting the fits in the plots based on the windowed decays

fv_A_fit  = -5.153e+08*exp(-0.002038*time);
fv_B_fit  = -2.022e+09*exp(-0.001045*time);
fv_AB_fit = -7.171e+08*exp(-0.0007746*time);

vf_A_fit  =  -3.193e+08*exp(-0.001233 *time);
vf_B_fit  = -1.102e+09 *exp(-0.00091*time);
vf_AB_fit =  -4.988e+08*exp( -0.000811*time);
%% plottimg the decays with their fits
figure()
```

```
hold on
plot(time./1000, -1*fv_A_fit, 'k')
plot(time./1000, -1*fv_B_fit, 'b')
plot(time./1000, -1*fv_AB_fit, 'r')

scatter(time./1000, -1*sum_fv_A, 'k')
scatter(time./1000, -1*sum_fv_B, 'b')
scatter(time./1000, -1*sum_fv_AB, 'r')
title('fv')
hold off

%%
figure()
hold on
plot(time./1000, -1*vf_A_fit, 'k')
plot(time./1000, -1*vf_B_fit, 'b')
plot(time./1000, -1*vf_AB_fit, 'r')

scatter(time./1000, -1*sum_vf_A, 'k')
scatter(time./1000, -1*sum_vf_B,'b')
scatter(time./1000, -1*sum_vf_AB, 'r')
title('vf')
hold off
%% ratio of the fits
fv_fit_ratio = fv_AB_fit./fv_B_fit;
vf_fit_ratio = vf_AB_fit./vf_B_fit;
%% plotting the ratios of the fit
figure()
hold on
plot(time, fv_fit_ratio)
title('fv fit ratio')
hold off

figure()
hold on
plot(time, vf_fit_ratio)
title('vf fit ratio')
hold off
%% Looking at the anistory
fv_ant_sum = (sum_fv_xx - sum_fv_xy)./(sum_fv_xx + 2*sum_fv_xy);
vf_ant_sum = (sum_vf_xx - sum_vf_xy)./(sum_vf_xx + 2*sum_vf_xy);

fv_ant_min = (min_fv_xx - min_fv_xy)./(min_fv_xx + 2*min_fv_xy);
vf_ant_min = (min_vf_xx - min_vf_xy)./(min_vf_xx + 2*min_vf_xy);
%%
figure()
hold on
```

```
plot(vf_ant_min,'k')
plot(fv_ant_min,'b')
hold off
%%

figure()
hold on
plot(vf_ant_sum)
plot(fv_ant_sum)
hold off
%%

for j = 1:40
    slice_plot_2d(j,:) = fv_full_spline(81,45:92,j);
end
%%

    axes1 = axes('Parent',figure());
    hold(axes1,'on');
    %contourf(vf_probe,vf_pump,(-
1*(vf_xx_full_spline(:,:,j))./min(min(vf_xx_full_spline(:,:,j)))
)', [linspace(-1, -0.05, 15), linspace(0.08, 0.8, 15)]);
    contourf((-1*(slice_plot_2d)./min(min(slice_plot_2d)))',
[linspace(-1, -0.05, 15), linspace(0.08, 0.8, 15)]);

set(axes1,'FontSize',12,'XMinorTick','on','YMinorTick','on');
    %plot(vf_probe,vf_probe,'k')
    colorbar;
    hold off
    title(['vf XXXX ',sprintf('%d',j)])
    xlabel('w probe (cm^-^1)');
    ylabel('w pump (cm^-^1)');
%     savefig(['VF Spectra ' num2str(j) ' with XXXX'])
%     saveas(figure(j), ['VF Spectra ' num2str(j) ' with
XXXX.png'])
%% Looking at the cross peak between the amide mode and the
carboxal mode
for j = 1:40
    fv_cross_xx(:,:,j) = fv_full_spline(78:85,10:30,j);
    fv_cross_xx_sum(:,j) = sum(sum(fv_cross_xx(:,:,j)));
    fv_cross_xx_min(:,j) = min(min(fv_cross_xx(:,:,j)));

    vf_cross_xx(:,:,j) = vf_full_spline(76:88,19:37,j);
    vf_cross_xx_sum(:,j) = sum(sum(vf_cross_xx(:,:,j)));
    vf_cross_xx_min(:,j) = min(min(vf_cross_xx(:,:,j)));
end
%%
```

```
cross_ratio_vf = vf_cross_xx_sum./sum_vf_B;
cross_ratio_fv = fv_cross_xx_sum./sum_fv_B;
%%
figure()
hold on
plot(fv_cross_xx_sum, 'k')
plot(vf_cross_xx_sum, 'b')
hold off

figure()
hold on
plot(fv_cross_xx_min, 'k')
plot(vf_cross_xx_min, 'b')
title('min')
hold off
%% fits
fv_cross_fit = -4.653e+08*exp( -0.0004791*time);

vf_cross_fit = -8.425e+08*exp( -0.0004695*time);
%%
fv_cross_sub = fv_cross_xx_sum - fv_cross_fit;
vf_cross_sub = vf_cross_xx_sum - vf_cross_fit;
%%
figure()
hold on
plot(time, fv_cross_sub, 'k')
plot(time, vf_cross_sub, 'b')
hold off
%%
ft_fv_cross = fftshift(fft(fftshift([fv_cross_sub, zeros(1,
80)])));
ft_vf_cross = fftshift(fft(fftshift([vf_cross_sub, zeros(1,
80)])));
%%
figure
hold on
plot(real(ft_fv_cross)./max(real(ft_vf_cross)), 'k')
plot(real(ft_vf_cross)./max(real(ft_vf_cross)), 'b')
hold off
%% Defining the carbox fits
carbox_fit_fv_a  = -5.047e+08*exp(-0.003234*time);
carbox_fit_fv_b  = -7.107e+08*exp(-0.003344*time);
carbox_fit_fv_c  = -2.738e+08*exp(-0.00317*time);
carbox_fit_fv_ab = -5.777e+08*exp(-0.003152*time);
carbox_fit_fv_bc = -2.934e+08*exp( -0.002915*time);

carbox_fit_vf_a  = -7.008e+08*exp(-0.002909*time);
```

```
carbox_fit_vf_b  = -9.471e+08*exp(-0.00268*time);
carbox_fit_vf_c  = -7.005e+08*exp(-0.002747*time);
carbox_fit_vf_ab = -7.114e+08*exp(-0.002633*time);
carbox_fit_vf_bc = -4.896e+08*exp(-0.002467*time);
%% looking at the integration of the carbox

figure()
hold on
plot(time, carbox_sum_fv_a, 'k')
plot(time, carbox_sum_vf_a, 'b')
hold off

figure()
hold on
plot(time, carbox_sum_fv_b, 'k')
plot(time, carbox_sum_vf_b, 'b')
hold off

figure()
hold on
plot(time, carbox_sum_fv_ab, 'k')
plot(time, carbox_sum_vf_ab, 'b')
hold off
%%
figure()
hold on
scatter(time, -1*carbox_sum_fv_b, 'k')
plot(time, -1*carbox_fit_fv_b)
scatter(time, -1*carbox_sum_fv_c, 'b')
plot(time, -1*carbox_fit_fv_c)
scatter(time, -1*carbox_sum_fv_bc, 'b')
plot(time, -1*carbox_fit_fv_bc)
title('FV')
hold off
%%
figure()
hold on
scatter(time, -1*carbox_sum_vf_b, 'k')
plot(time, -1*carbox_fit_vf_b, 'k')
scatter(time, -1*carbox_sum_vf_c, 'b')
plot(time, -1*carbox_fit_vf_c, 'b')
scatter(time, -1*carbox_sum_vf_bc, 'r')
plot(time, -1*carbox_fit_vf_bc, 'r')
title('vf')
hold off
%% carbox ratios
carbox_fv_ratio = carbox_sum_fv_ab./carbox_sum_fv_b;
```

```
carbox_vf_ratio = carbox_sum_vf_ab./carbox_sum_vf_b;









%% Doing the robuin subtraction

% for j = 1:40
%     fv_2d_sub(:,:,j) =  fv_full_spline(:,:,j)-
fv_full_spline(:,:,1);
%     vf_2d_sub(:,:,j) =  vf_full_spline(:,:,j)-
vf_full_spline(:,:,1);
% end
% %%
% for j = 1:40
%     vf_A_sub(:,:,j)  = vf_2d_sub(73:77,59:63,j);
%     vf_B_sub(:,:,j)  = vf_2d_sub(78:84,66:72,j);
%     vf_AB_sub(:,:,j) = vf_2d_sub(78:84,59:63,j);
%
%
%     fv_A_sub(:,:,j)  = fv_2d_sub(72:76,59:63,j);
%     fv_B_sub(:,:,j)  = fv_2d_sub(78:84,66:72,j);
%     fv_AB_sub(:,:,j) = fv_2d_sub(78:84,59:63,j);
% end
% %% min
% for j = 1:40
%     min_vf_A_sub(:,j)  = min(min(vf_A_sub(:,:,j)));
%     min_vf_B_sub(:,j)  = min(min(vf_B_sub(:,:,j)));
%     min_vf_AB_sub(:,j) = min(min(vf_AB_sub(:,:,j)));
%
%     min_fv_A_sub(:,j)  = min(min(fv_A_sub(:,:,j)));
%     min_fv_B_sub(:,j)  = min(min(fv_B_sub(:,:,j)));
%     min_fv_AB_sub(:,j) = min(min(fv_AB_sub(:,:,j)));
% end
% %% sum
% for j = 1:40
%     sum_vf_A_sub(:,j)  = sum(sum(vf_A_sub(:,:,j)));
%     sum_vf_B_sub(:,j)  = sum(sum(vf_B_sub(:,:,j)));
%     sum_vf_AB_sub(:,j) = sum(sum(vf_AB_sub(:,:,j)));
%
```

```
%      sum_fv_A_sub(:,j)  = sum(sum(fv_A_sub(:,:,j)));
%      sum_fv_B_sub(:,j)  = sum(sum(fv_B_sub(:,:,j)));
%      sum_fv_AB_sub(:,j) = sum(sum(fv_AB_sub(:,:,j)));
% end
% %% ratios
% time2 = linspace(100, 3900, 39)
% %%

% fv_sub_ratio = -1*(sum_fv_AB_sub(:,2:40)./sum_fv_B_sub(:,2:40));

%

% vf_sub_ratio = -1*(sum_vf_AB_sub(:,2:40)./sum_vf_B_sub(:,2:40));
```

Appendix II

This appendix provides additional bright field images and IR spectra of the various structures formed by IF and FI in D_2O and DMSO.

Table 1. Amide I peak positions of the different aggregates formed by IF and FI and in different solvent systems. In some cases, there are distributions of structures. Therefore there are at least two different Amide I positions. The spectra with multiple Amide I peaks have a second peak position listed.

	Sample Label	Amide I position (cm^{-1})
IF in D_2O	Image A Spec. 1	1672
	Image A Spec. 2	1669
	Image B Spec. 1	1671
	Image C Spec. 1	1668
	Image C Spec. 2	1673
	Image D Spec. 1	1649
	Image D Spec. 2	1648
	Image D Spec. 3	1671
FI in D_2O	Image A Spec. 1	1683
	Image A Spec. 2	1665
	Image B Spec. 1	1678
	Image B Spec. 2	1683
	Image C Spec. 1	1678
	Image D Spec. 1	1680
	Image E Spec. 1	1682
IF in DMSO	Image A Spec. 1	1667
	Image A Spec. 2	1666
	Image A Spec. 3	1667
	Image B Spec. 1	1670
	Image B Spec. 2	1667
	Image B Spec. 3	1667
	Image B Spec. 4	1665
FI in DMSO	Image A Spec. 1	1667
	Image A Spec. 2	1668
	Image B Spec. 1	1664
	Image C Spec. 1	1669
	Image C Spec. 2	1669
	Image D Spec. 1	1668
	Image D Spec. 2	1668

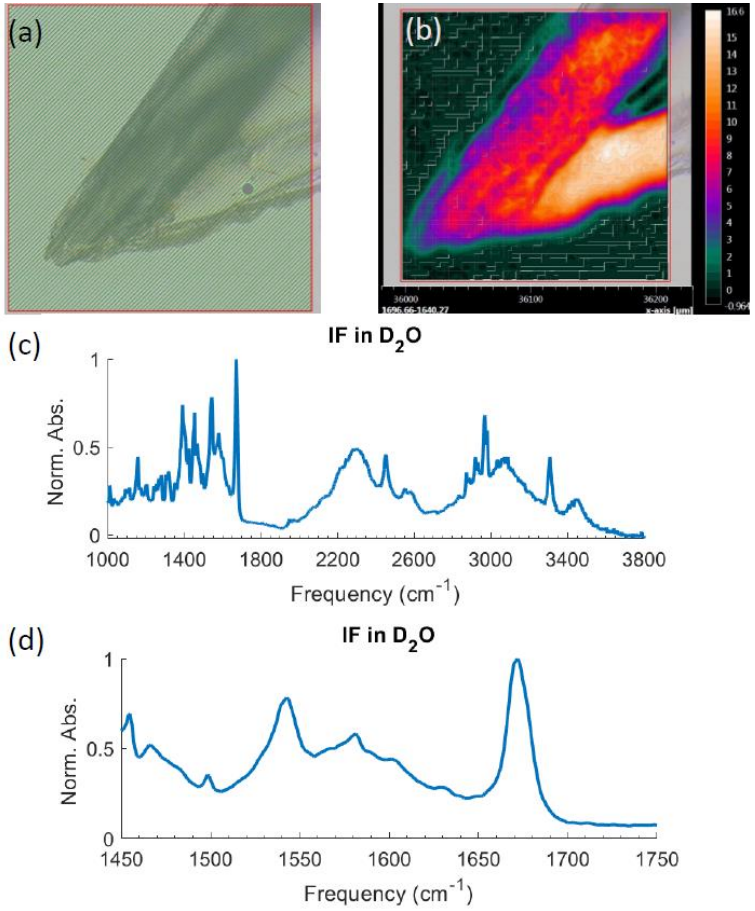

Figure 1 FTIR microscopy data of IF's self-assembled structure in D_2O. Bright field image is shown in (a), the red dot corresponds to the FTIR shown in (c) and (d). Finally, the integration of the amide I peak is shown in (b).

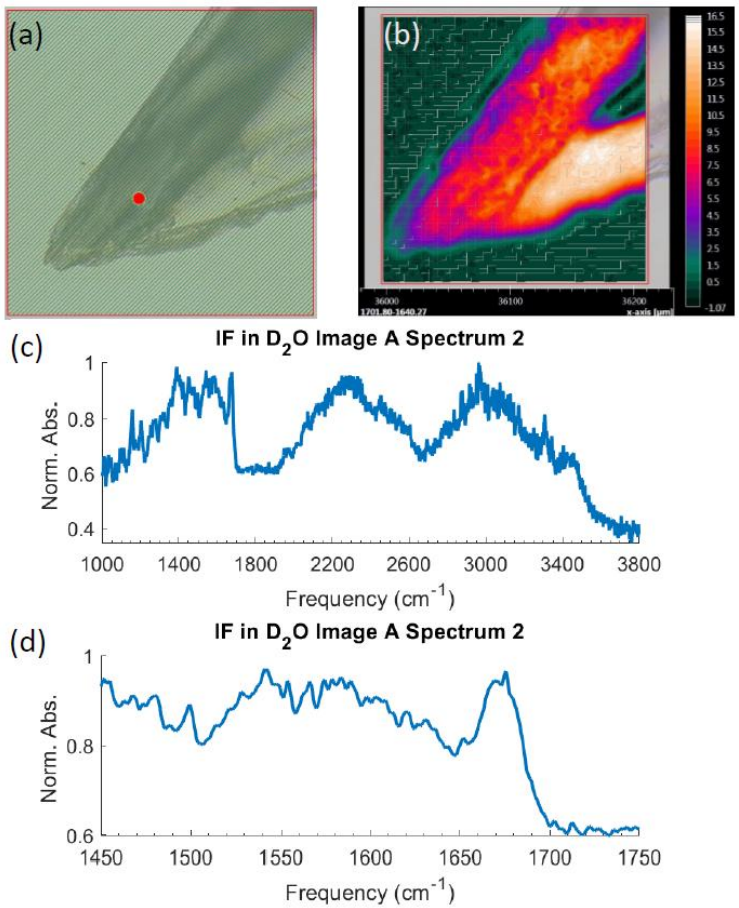

Figure 2 FTIR microscopy data of IF's self-assembled structure in D_2O. Bright field image is shown in (a), the red dot corresponds to the FTIR shown in (c) and (d). Finally, the integration of the amide I peak is shown in (b).

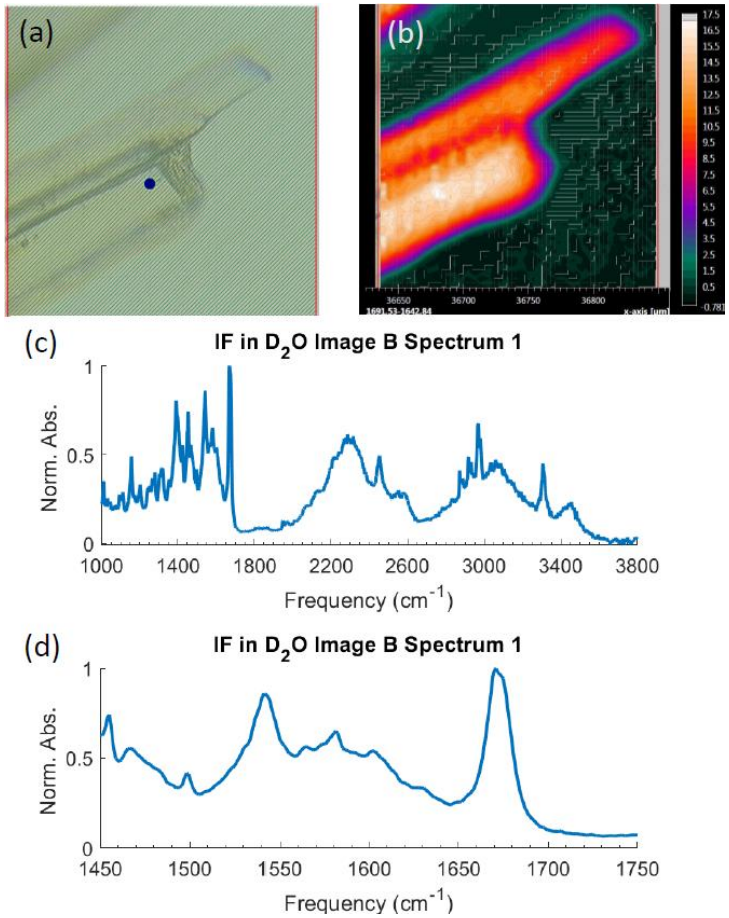

Figure 3 FTIR microscopy data of IF self-assembled structure in D_2O. Bright field image is shown in (a), the red dot corresponds to the FTIR shown in (c) and (d). Finally, the integration of the amide I peak is shown in (b).

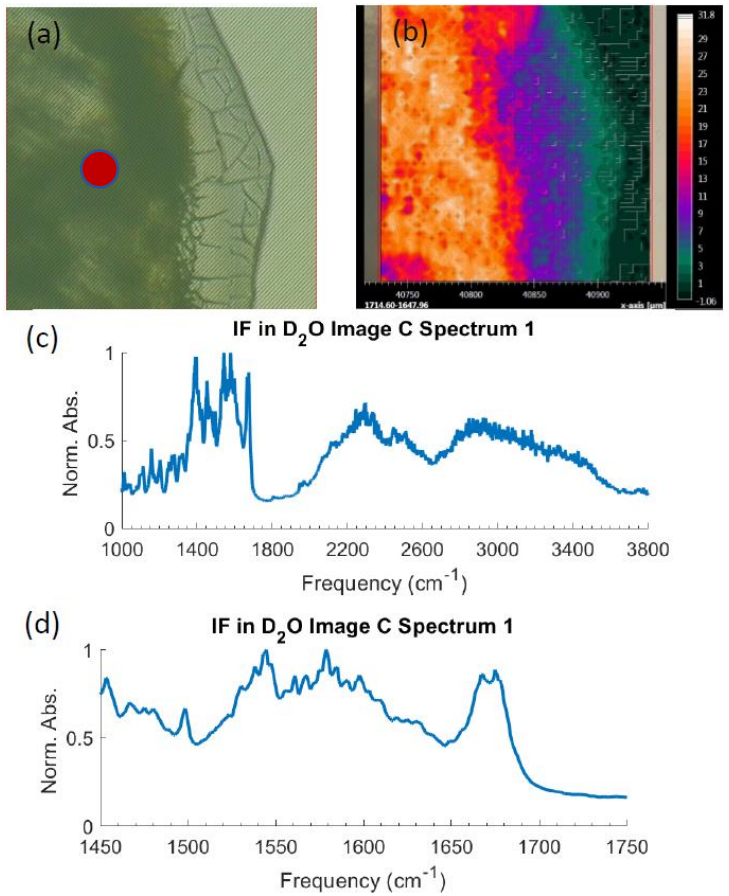

Figure 4 FTIR microscopy data of IF self-assembled structure in D_2O. Bright field image is shown in (a), the red dot corresponds to the FTIR shown in (c) and (d). Finally, the integration of the amide I peak is shown in (b).

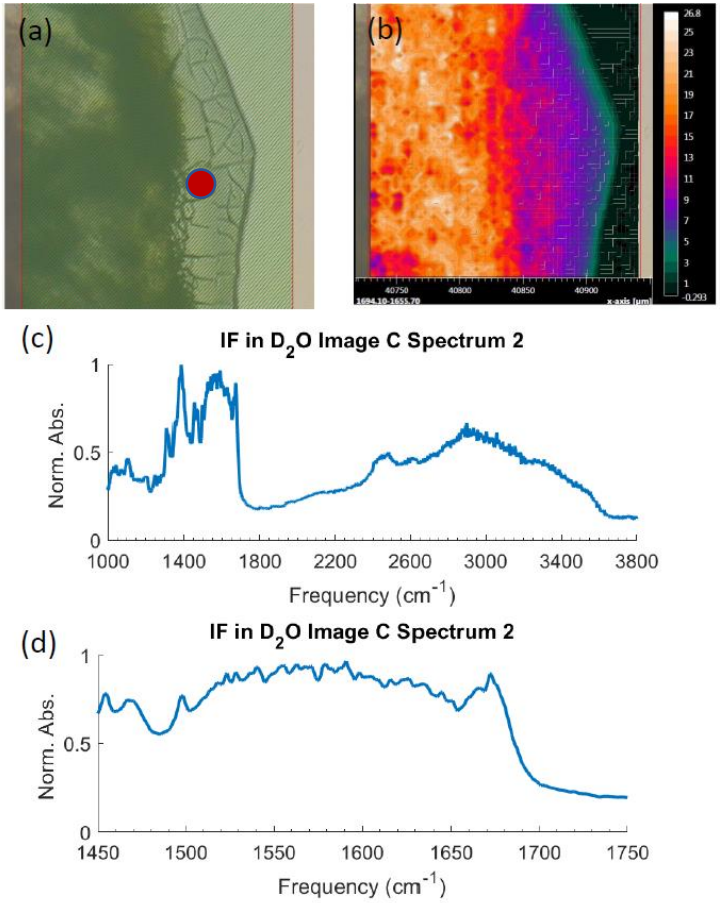

Figure 5 FTIR microscopy data of IF self-assembled structure in D_2O. Bright field image is shown in (a), the red dot corresponds to the FTIR shown in (c) and (d). Finally, the integration of the amide I peak is shown in (b).

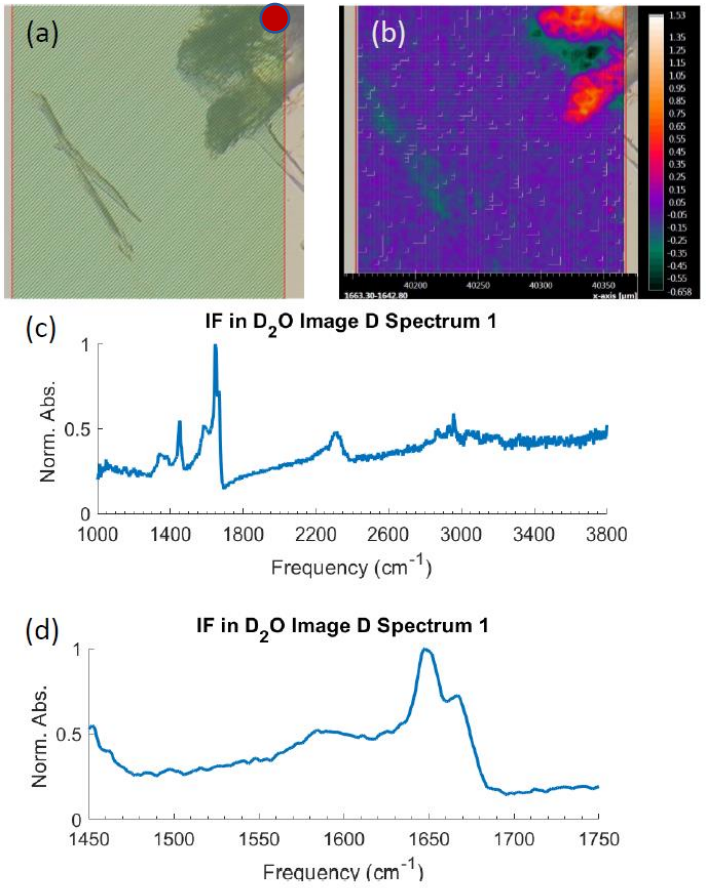

Figure 6 FTIR microscopy data of IF self-assembled structure in D_2O. Bright field image is shown in (a), the red dot corresponds to the FTIR shown in (c) and (d). Finally, the integration of the amide I peak is shown in (b).

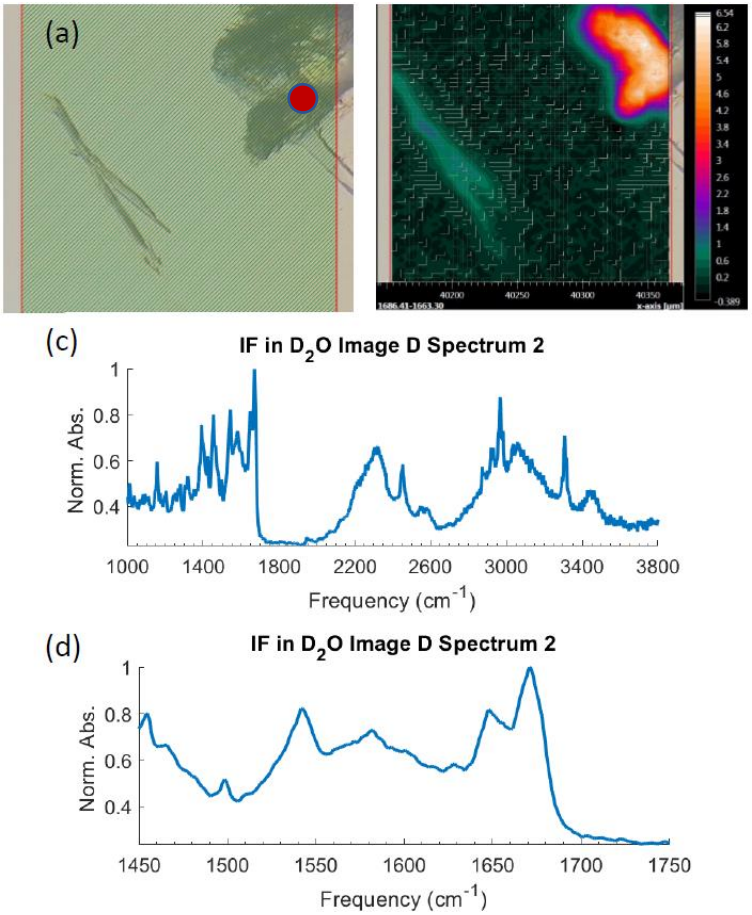

Figure 7 FTIR microscopy data of IF self-assembled structure in D_2O. Bright field image is shown in (a), the red dot corresponds to the FTIR shown in (c) and (d). Finally, the integration of the amide I peak is shown in (b).

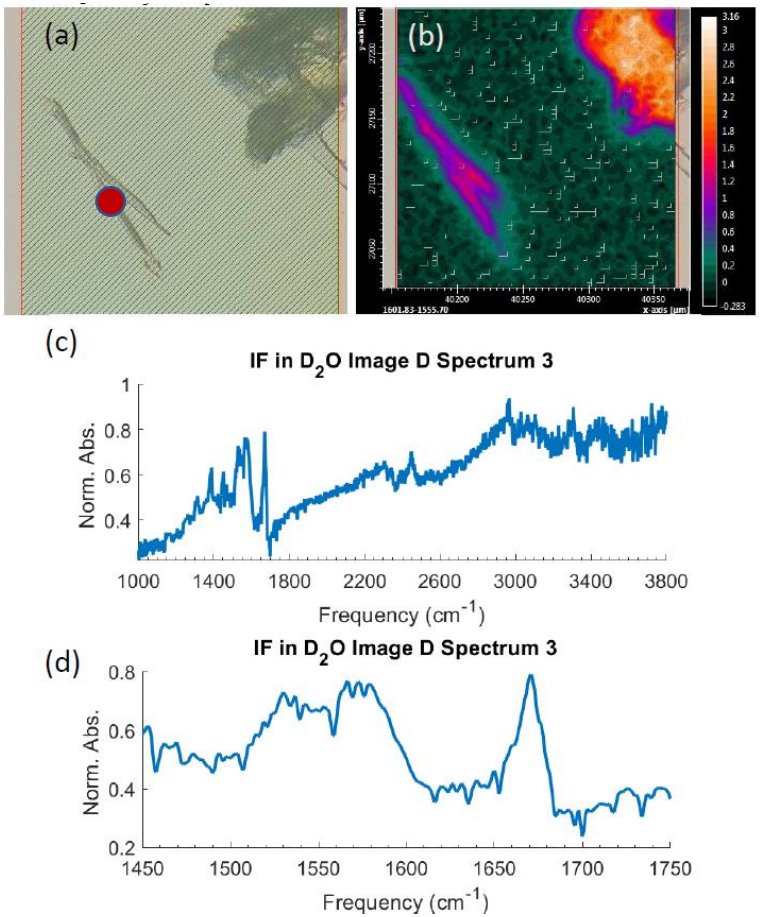

Figure 8 FTIR microscopy data of IF self-assembled structure in D_2O. Bright field image is shown in (a), the red dot corresponds to the FTIR shown in (c) and (d). Finally, the integration of the amide I peak is shown in (b).

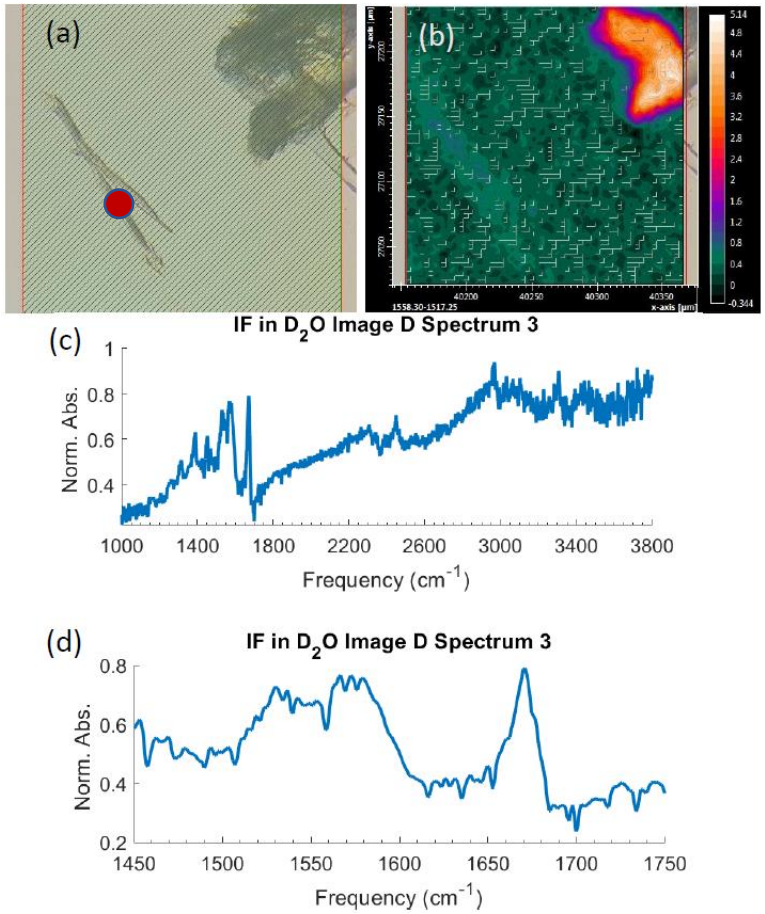

Figure 9 FTIR microscopy data of IF self-assembled structure in D_2O. Bright field image is shown in (a), the red dot corresponds to the FTIR shown in (c) and (d). Finally, the integration of the amide I peak is shown in (b).

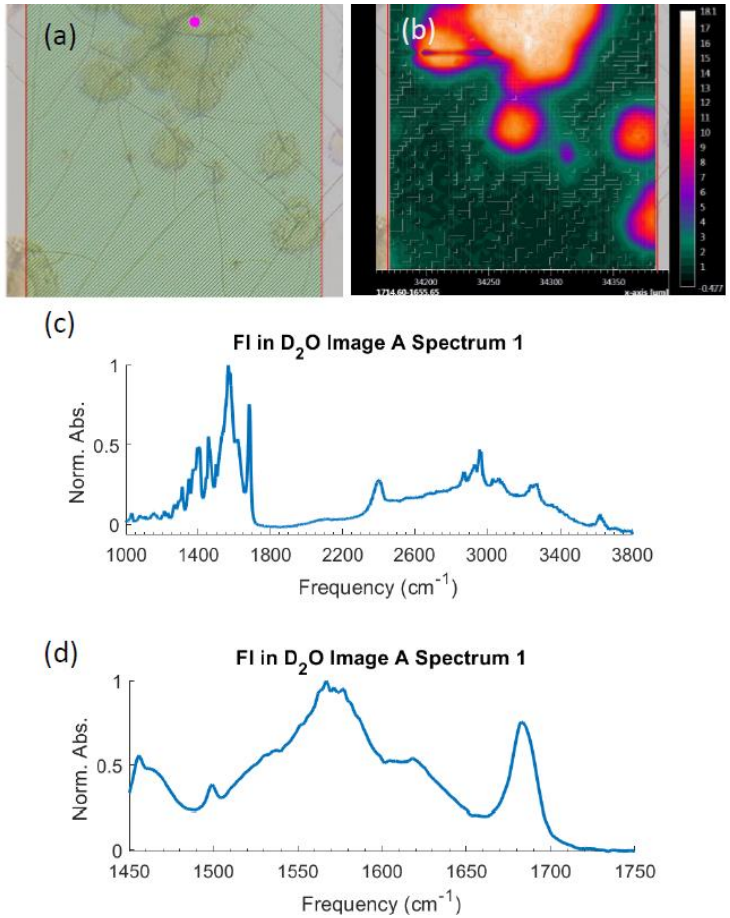

Figure 10 FTIR microscopy data of FI self-assembled structure in D_2O. Bright field image is shown in (a), the red dot corresponds to the FTIR shown in (c) and (d). Finally, the integration of the amide I peak is shown in (b).

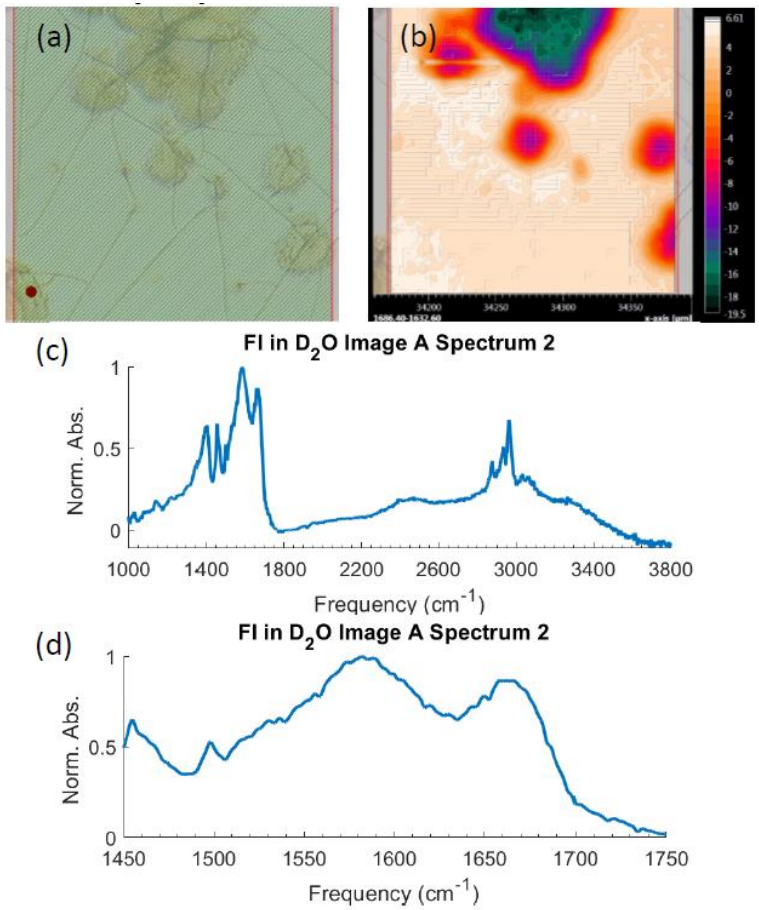

Figure 11 FTIR microscopy data of FI self-assembled structure in D_2O. Bright field image is shown in (a), the red dot corresponds to the FTIR shown in (c) and (d). Finally, the integration of the amide I peak is shown in (b).

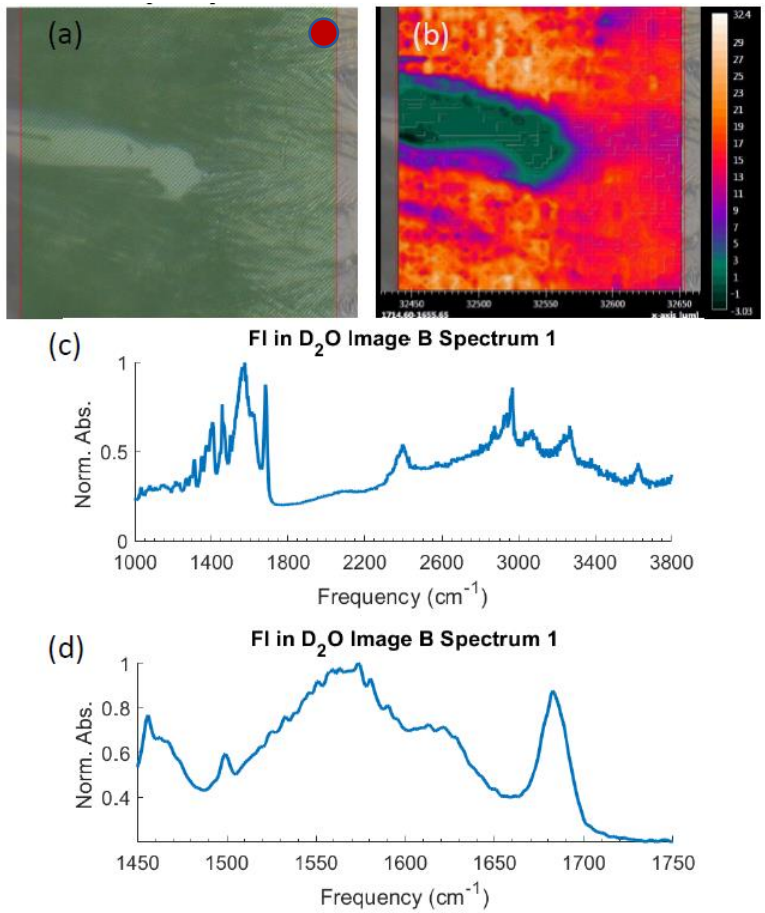

Figure 12 FTIR microscopy data of FI self-assembled structure in D_2O. Bright field image is shown in (a), the red dot corresponds to the FTIR shown in (c) and (d). Finally, the integration of the amide I peak is shown in (b).

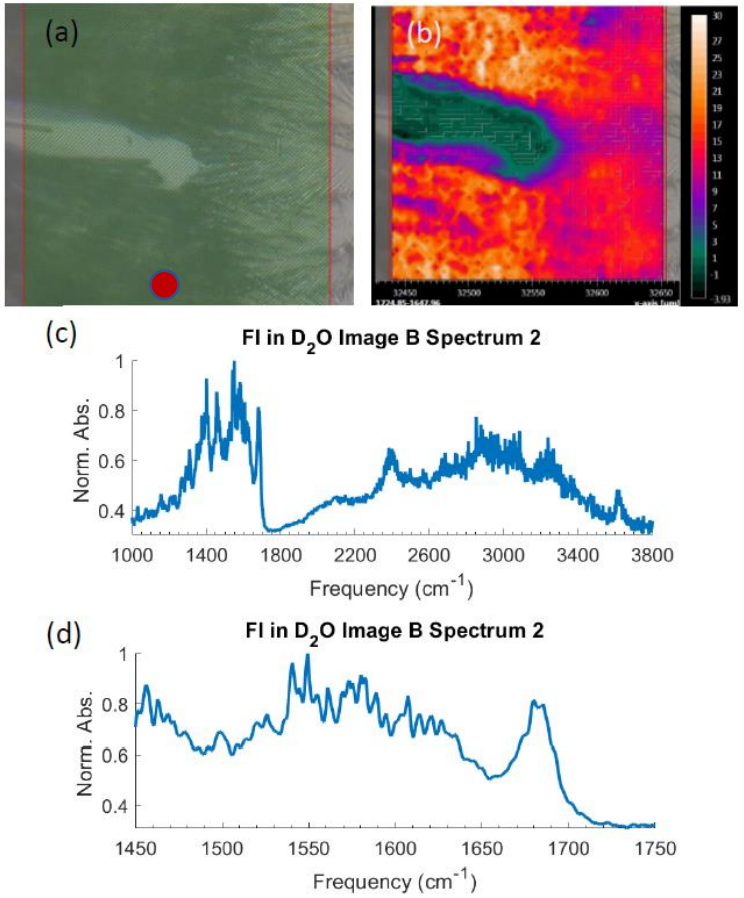

Figure 13 FTIR microscopy data of FI self-assembled structure in D_2O. Bright field image is shown in (a), the red dot corresponds to the FTIR shown in (c) and (d). Finally, the integration of the amide I peak is shown in (b).

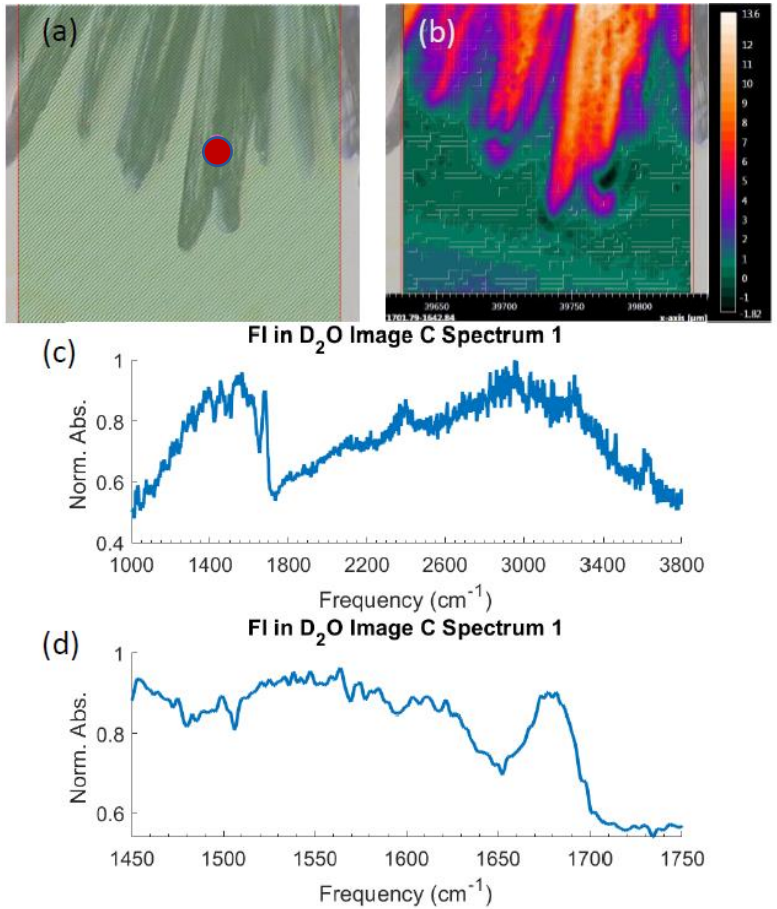

Figure 14 FTIR microscopy data of FI self-assembled structure in D_2O. Bright field image is shown in (a), the red dot corresponds to the FTIR shown in (c) and (d). Finally, the integration of the amide I peak is shown in (b).

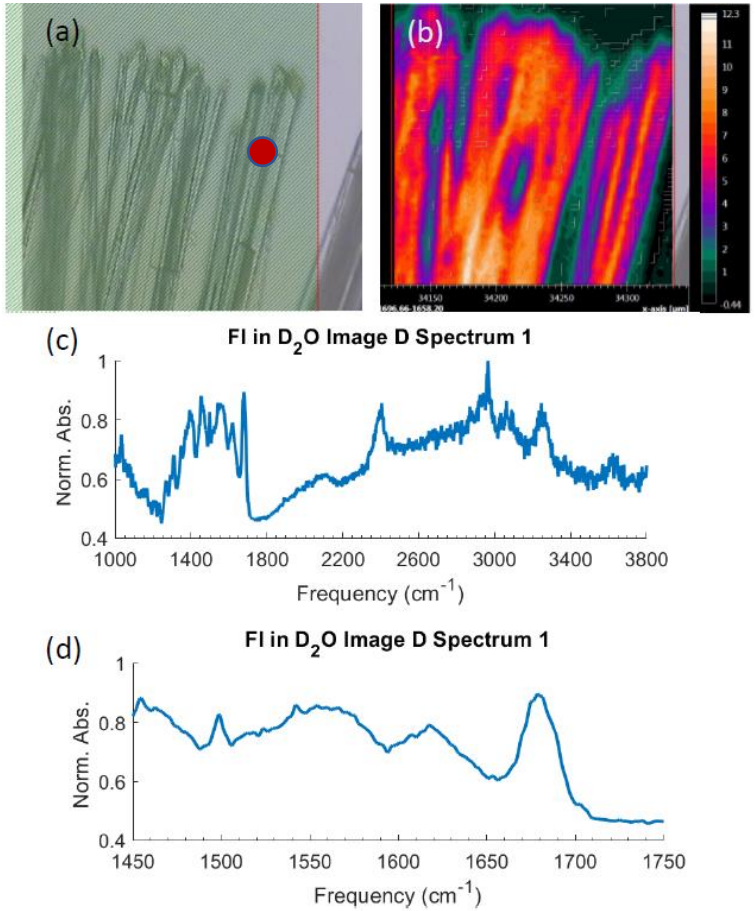

Figure 15 FTIR microscopy data of FI self-assembled structure in D_2O. Bright field image is shown in (a), the red dot corresponds to the FTIR shown in (c) and (d). Finally, the integration of the amide I peak is shown in (b).

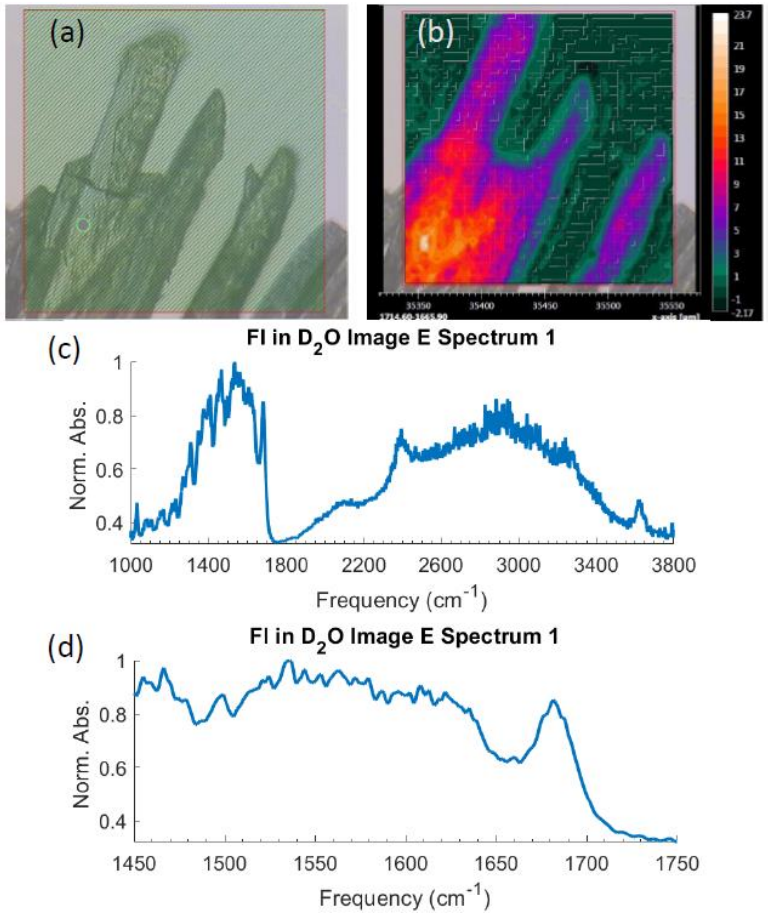

Figure 16 FTIR microscopy data of FI self-assembled structure in D_2O. Bright field image is shown in (a), the red dot corresponds to the FTIR shown in (c) and (d). Finally, the integration of the amide I peak is shown in (b).

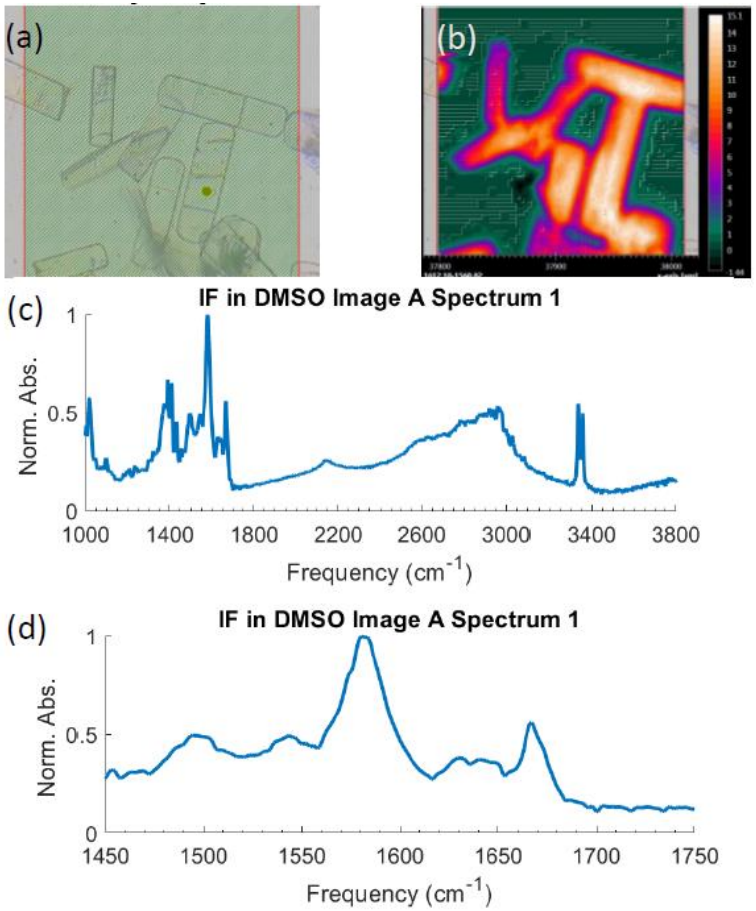

Figure 17 FTIR microscopy data of IF self-assembled structure in DMSO. Bright field image is shown in (a), the red dot corresponds to the FTIR shown in (c) and (d). Finally, the integration of the amide I peak is shown in (b).

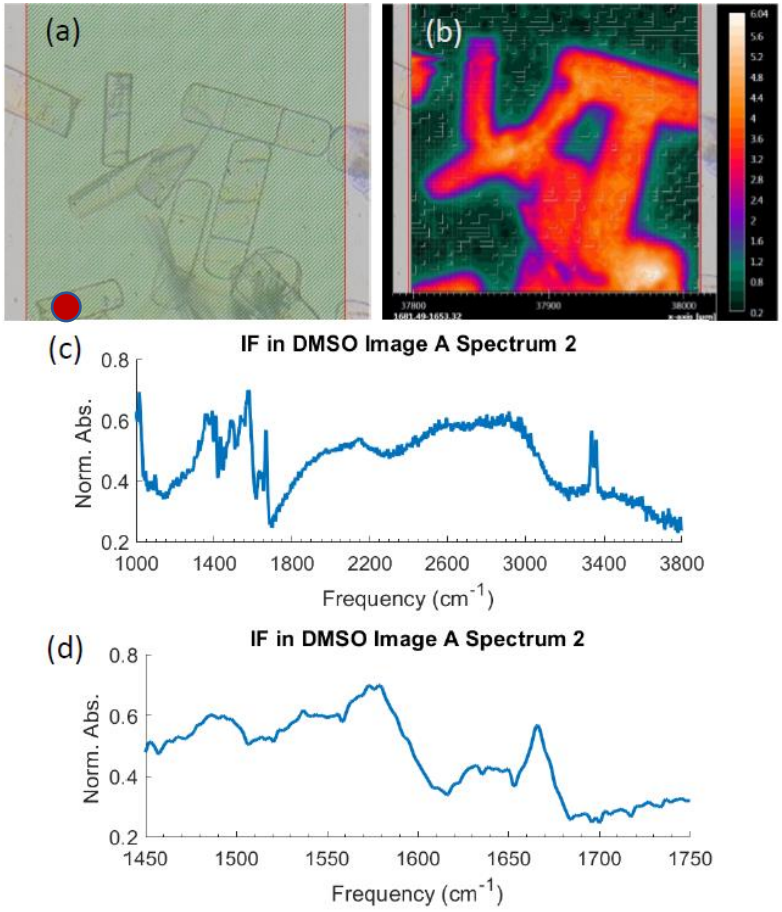

Figure 18 FTIR microscopy data of IF self-assembled structure in DMSO. Bright field image is shown in (a), the red dot corresponds to the FTIR shown in (c) and (d). Finally, the integration of the amide I peak is shown in (b).

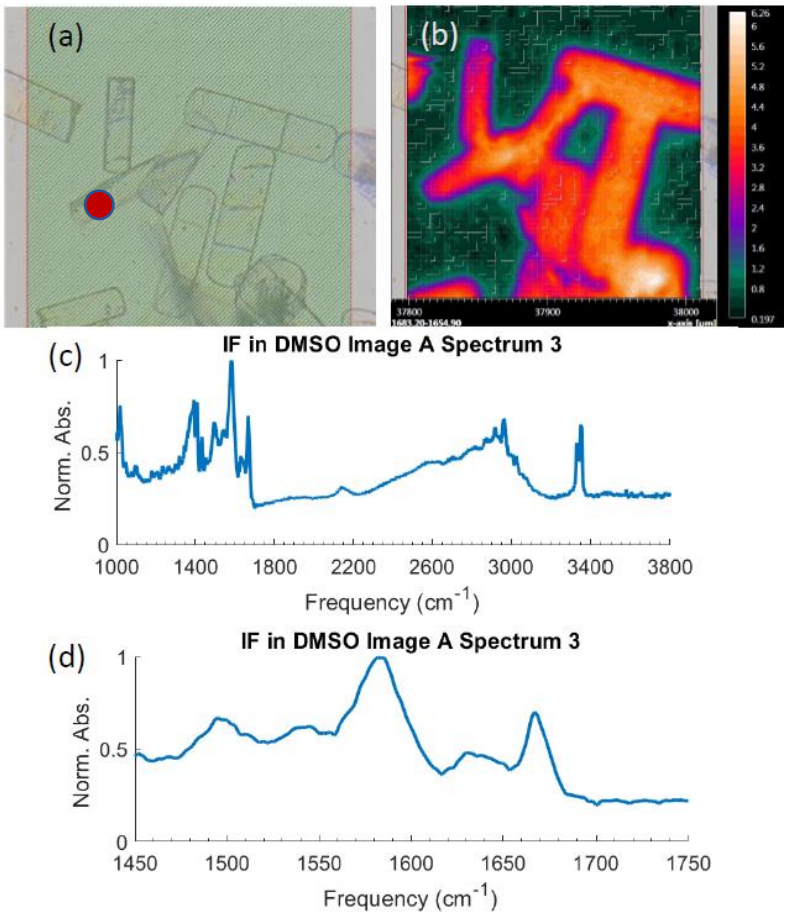

Figure 19 FTIR microscopy data of IF self-assembled structure in DMSO. Bright field image is shown in (a), the red dot corresponds to the FTIR shown in (c) and (d). Finally, the integration of the amide I peak is shown in (b).

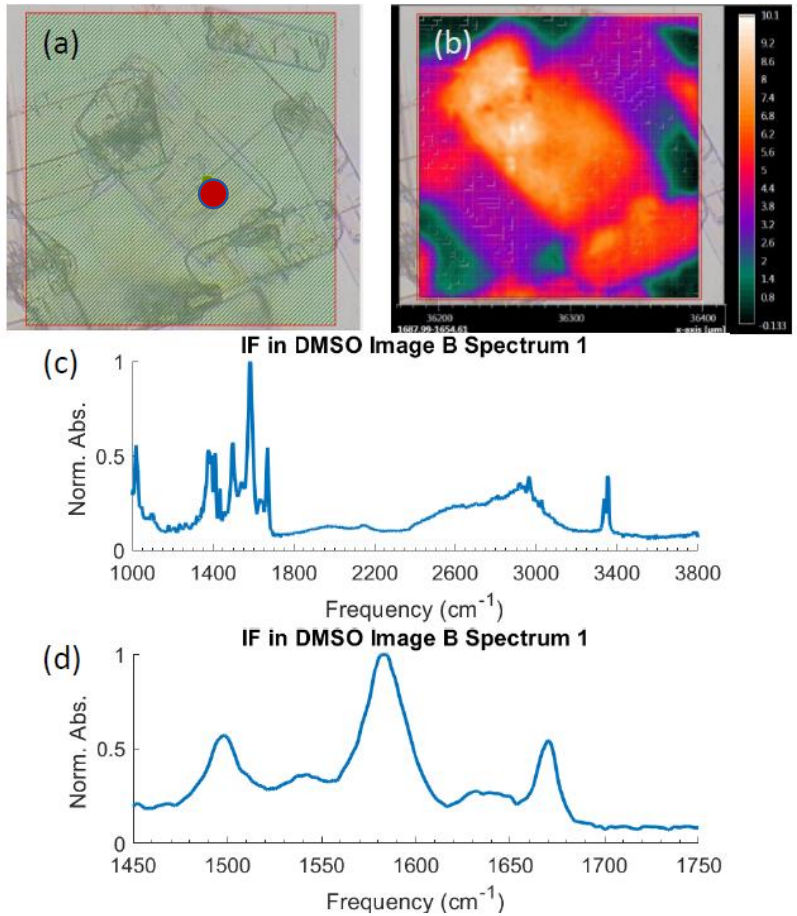

Figure 20 FTIR microscopy data of IF self-assembled structure in DMSO. Bright field image is shown in (a), the red dot corresponds to the FTIR shown in (c) and (d). Finally, the integration of the amide I peak is shown in (b).

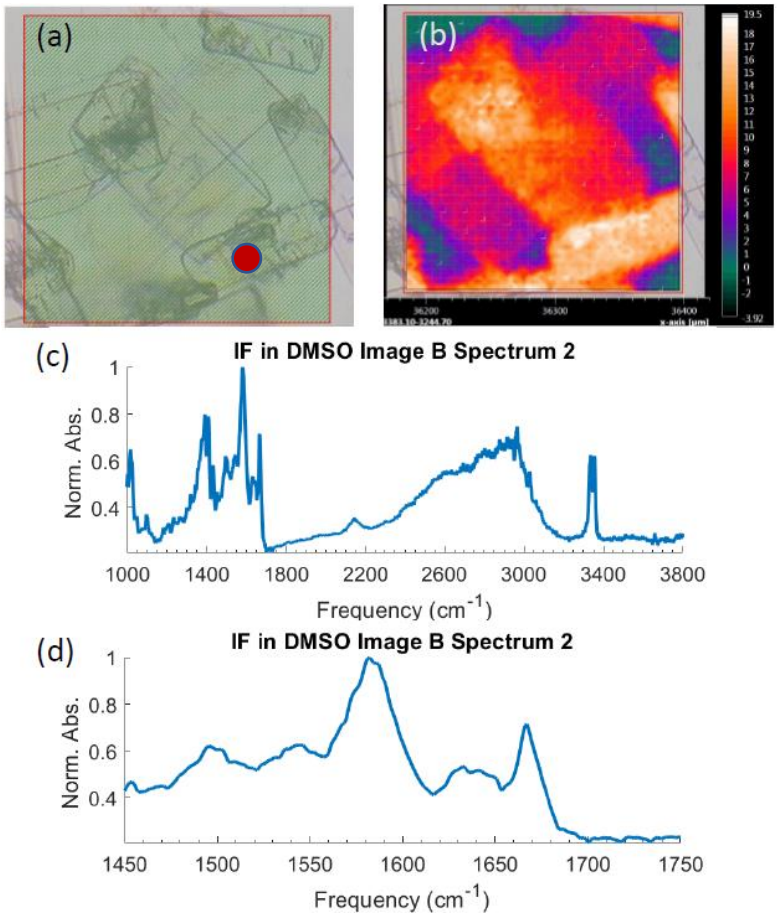

Figure 21 FTIR microscopy data of IF self-assembled structure in DMSO. Bright field image is shown in (a), the red dot corresponds to the FTIR shown in (c) and (d). Finally, the integration of the amide I peak is shown in (b).

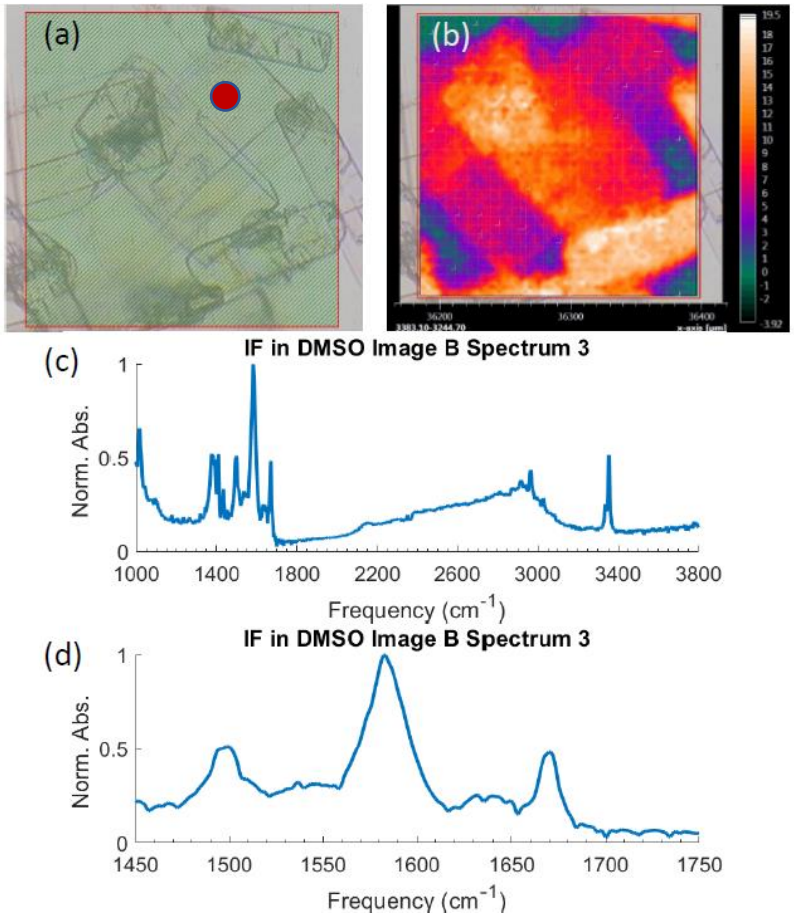

Figure 22 FTIR microscopy data of IF self-assembled structure in DMSO. Bright field image is shown in (a), the red dot corresponds to the FTIR shown in (c) and (d). Finally, the integration of the amide I peak is shown in (b).

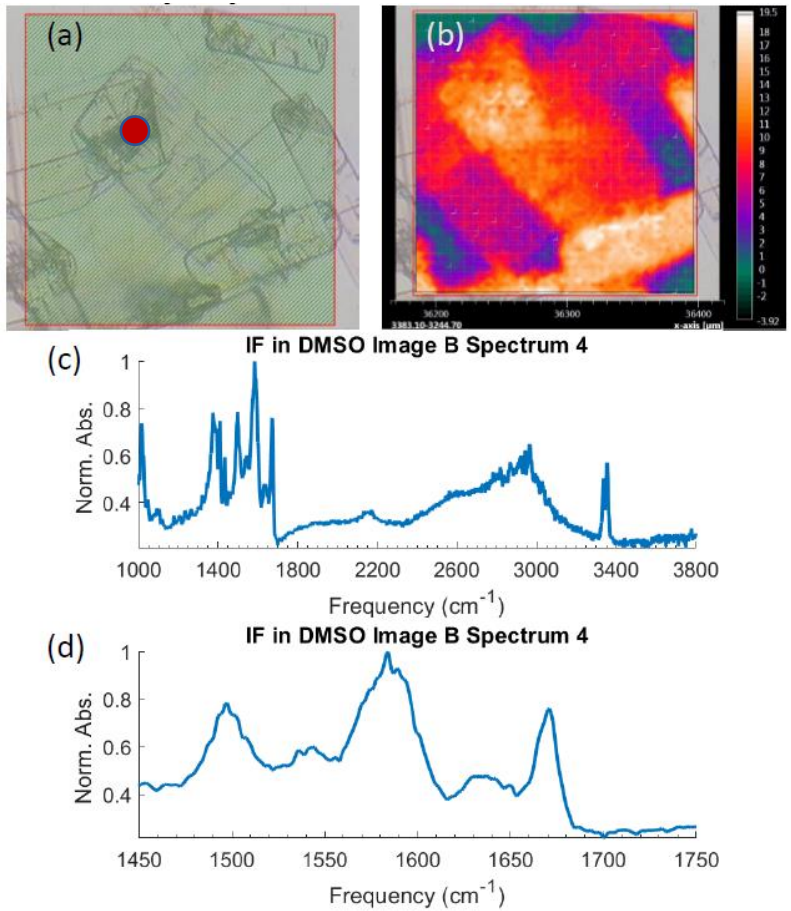

Figure 23 FTIR microscopy data of IF self-assembled structure in DMSO. Bright field image is shown in (a), the red dot corresponds to the FTIR shown in (c) and (d). Finally, the integration of the amide I peak is shown in (b).

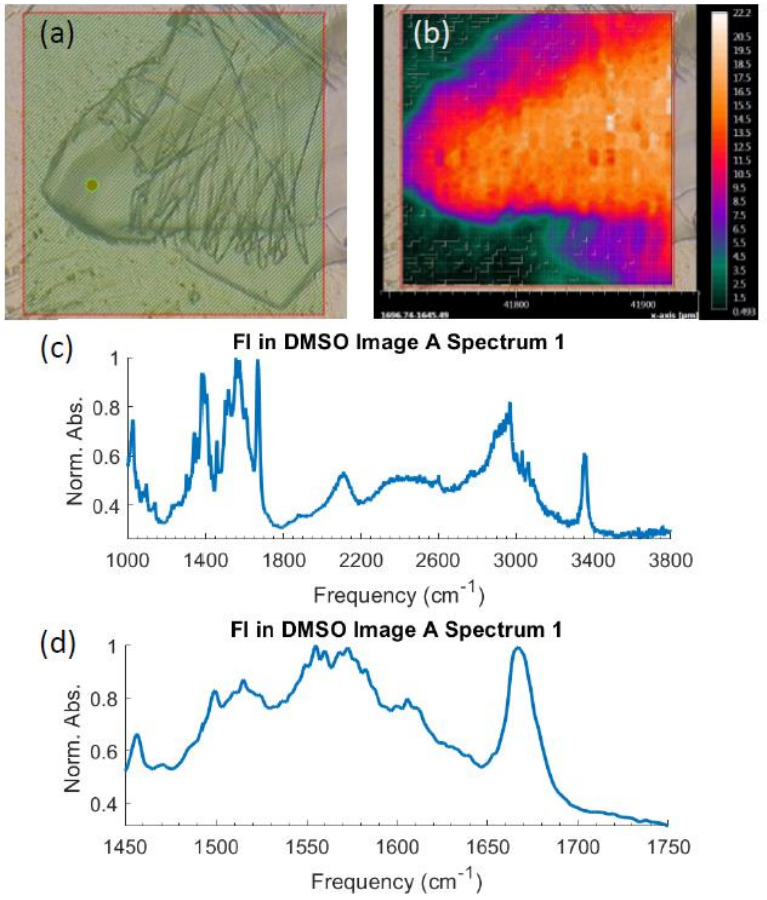

Figure 24 FTIR microscopy data of FI self-assembled structure in DMSO. Bright field image is shown in (a), the red dot corresponds to the FTIR shown in (c) and (d). Finally, the integration of the amide I peak is shown in (b).

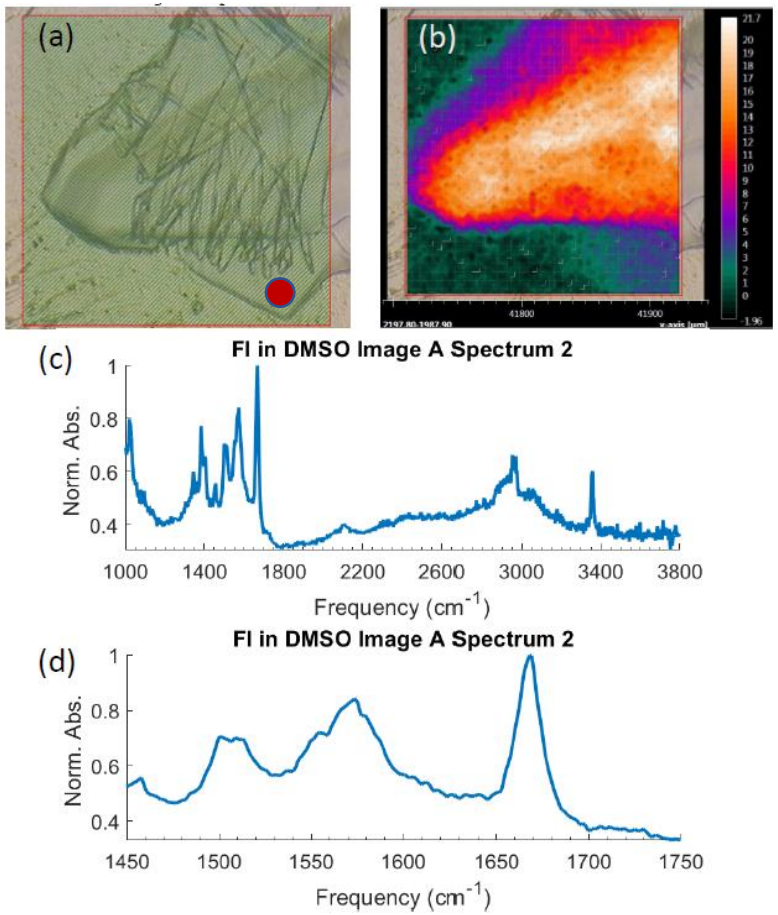

Figure 25 FTIR microscopy data of FI self-assembled structure in DMSO. Bright field image is shown in (a), the red dot corresponds to the FTIR shown in (c) and (d). Finally, the integration of the amide I peak is shown in (b).

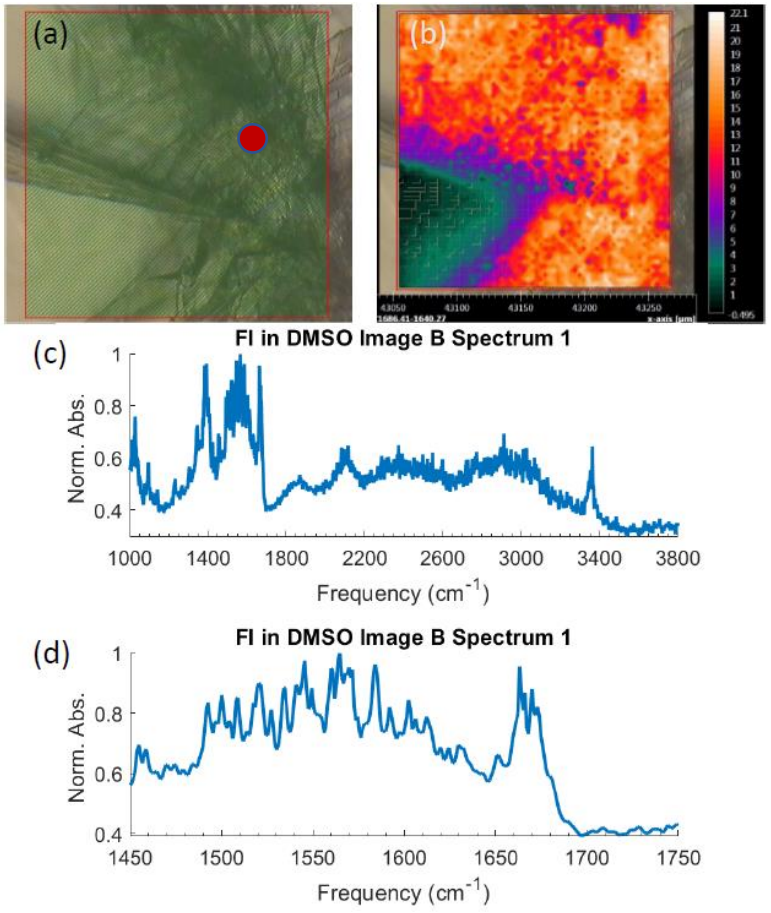

Figure 26 FTIR microscopy data of FI self-assembled structure in DMSO. Bright field image is shown in (a), the red dot corresponds to the FTIR shown in (c) and (d). Finally, the integration of the amide I peak is shown in (b) .

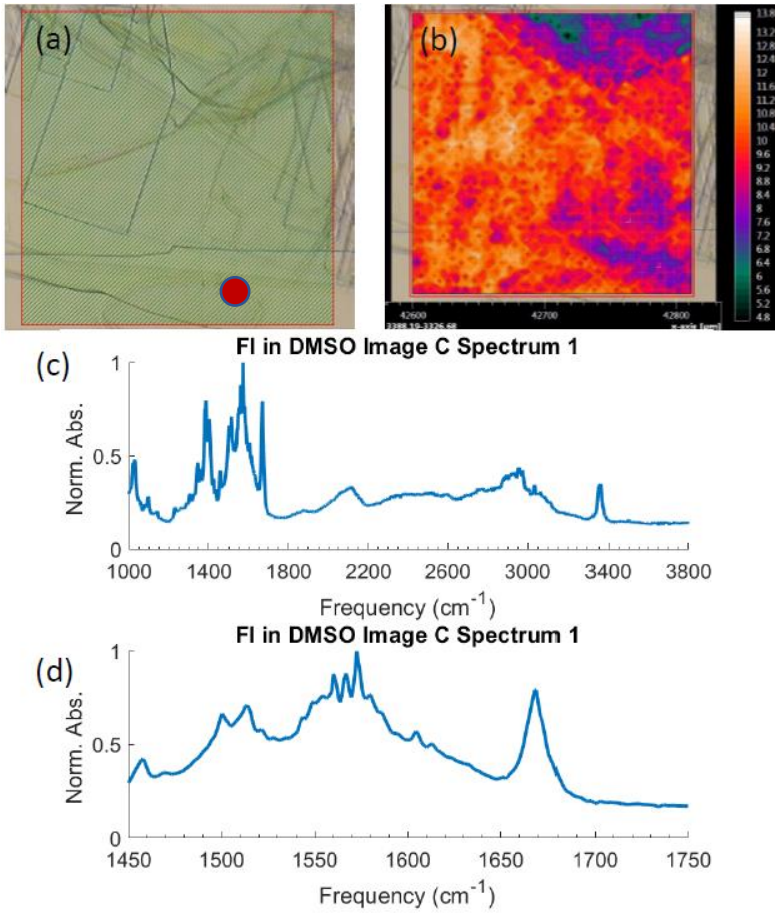

Figure 27 FTIR microscopy data of FI self-assembled structure in DMSO. Bright field image is shown in (a), the red dot corresponds to the FTIR shown in (c) and (d). Finally, the integration of the amide I peak is shown in (b).

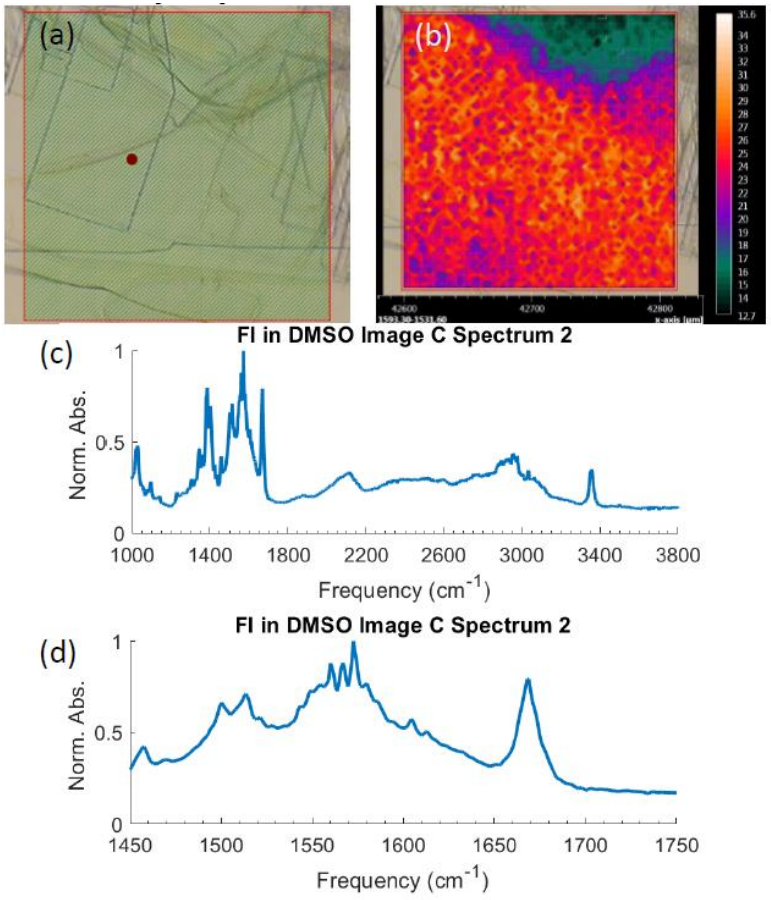

Figure 28 FTIR microscopy data of FI self-assembled structure in DMSO. Bright field image is shown in (a), the red dot corresponds to the FTIR shown in (c) and (d). Finally, the integration of the amide I peak is shown in (b).

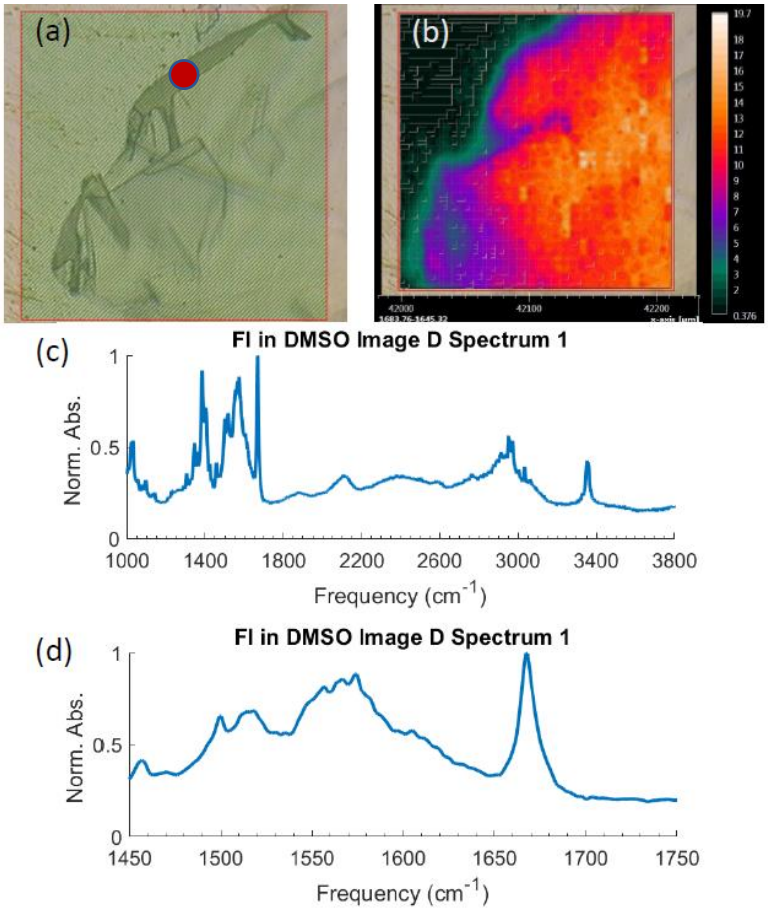

Figure 29 FTIR microscopy data of FI self-assembled structure in DMSO. Bright field image is shown in (a), the red dot corresponds to the FTIR shown in (c) and (d). Finally, the integration of the amide I peak is shown in (b).